INSTITUTE OF NATURAL AND APPLIED SCIENCES
UNIVERSITY OF CUKUROVA

PhD THESIS

İlham NASIROĞLU

FAST TIMING PHOTO–POLARIMETRY WITH OPTIMA

DEPARTMENT OF PHYSICS

ADANA, 2012

ÇUKUROVA ÜNİVERSİTESİ
FEN BİLİMLERİ ENSTİTÜSÜ

OPTIMA İLE HIZLI FOTOMETRİ VE POLARİMETRİ

İlham NASIROĞLU

DOKTORA TEZİ

FİZİK ANABİLİM DALI

Bu Tez 02 / 07 / 2010 Tarihinde Aşağıdaki Jüri Üyeleri Tarafından Oybirliği/Oyçokluğu ile Kabul Edilmiştir.

.....	.....	.....
Prof. Dr. Aysun AKYÜZ	Dr. Gottfried KANBACH	Prof. Dr. M. Emin ÖZEL
DANIŞMAN	ÜYE	ÜYE
.....	.....	
Prof. Dr. Yüksel UFUKTEPE	Doç. Dr. Mustafa KANDIRMAZ	
ÜYE	ÜYE	

Bu Tez Enstitümüz Fizik Anabilim Dalında hazırlanmıştır.
Kod No:

Prof. Dr. M. Rifat ULUSOY
Enstitü Müdürü

Bu Çalışma Ç.Ü. Araştırma Projeleri Birimi Tarafından Desteklenmiştir.
Proje No: FEF2010D17

Sevgili Aileme,

*

* * * * *

ABSTRACT

PhD THESIS

FAST TIMING PHOTO−POLARIMETRY WITH OPTIMA

İlham NASIROĞLU

ÇUKUROVA UNIVERSITY
INSTITUTE OF NATURAL AND APPLIED SCIENCES
DEPARTMENT OF PHYSICS

Supervisor: Prof. Dr. Aysun AKYÜZ

Year: 2012, Pages: 160

Jury : Prof. Dr. Aysun AKYÜZ
: Dr. Gottfried KANBACH
: Prof. Dr. M. Emin ÖZEL
: Prof. Dr. Yüksel UFUKTEPE
: Assoc. Prof. Dr. Mustafa KANDIRMAZ

Cataclysmic variables are interacting close binaries which constitute a general class of binary star systems. These systems radiate in the radio through gamma-ray bandpasses, hence several hundreds of those close to our Sun have been studied extensively with ground-based and space-based telescopes. The cataclysmic variable systems contain an accreting white dwarf and a normal star companion. The entire binary system usually has the size of the Sun with an orbital period in the range of 1-10 hour. In this work, general properties of cataclysmic variables were reviewed, and fast-photometric and X-ray observations of two magnetic cataclysmic variables, HU Aqr (polar) and V2069 Cyg (intermediate polar), were presented. Additionaly, in order to calibrate the polarimeter mode of OPTIMA (OPtical TIming Analyzer) some polarization measurements and polarimetric observations of some standart stars were obtained. The fast photometric and polarimetric observations were performed with OPTIMA instrument at the 1.3 m telescope at Skinakas Observatory (Crete). The X-ray observations were performed with the XMM-Newton and Swift/XRT telescopes. The timing analyse of the optical/X-ray light curves of V2069 Cyg showed double-peaked emission profile at the white dwarf spin period. Here, we discussed the probable mechanism which causes double-peaked profile. Furthermore, we presented the X-ray spectra obtained from the XMM-Newton EPIC instruments. Additionally, we investigated the long term orbital period change of the eclipsing binary system HU Aqr. We created O−C (observed minus calculated) light curves of the system including recent observations together with the existing data in the literature. We discussed probable mechanisms which cause the orbital period change of binary systems.

Keywords: Magnetic Cataclysmic Variables, V2069 Cygni, HU Aquarii, OPTIMA, Photo-polarimetry.

ÖZ

DOKTORA TEZİ

OPTIMA İLE HIZLI FOTOMETRİ VE POLARİMETRİ

İlham NASIROĞLU

ÇUKUROVA ÜNİVERSİTESİ
FEN BİLİMLERİ ENSTİTÜSÜ
FİZİK ANABİLİM DALI

Danışman: Prof. Dr. Aysun AKYÜZ
Yıl: 2012, Sayfa: 160
Jüri : Prof. Dr. Aysun AKYÜZ
: Dr. Gottfried KANBACH
: Prof. Dr. M. Emin ÖZEL
: Prof. Dr. Yüksel UFUKTEPE
: Doç. Dr. Mustafa KANDIRMAZ

Kataklismik değişen yıldızlar çift yıldız sistemlerinin genel bir sınıfını oluştururlar. Bu sistemler, radyo ışınımından gama ışınımına kadar tüm dalga boylarında ışıma yaparlar, bu yüzden Güneş sistemine yakın olan yüzlercesi uzay ve yer tabanlı teleskoplar ile yaygın olarak çalışılmaktadır. Bu sistemler bir beyaz cüce ve ona kütle aktaran normal bir eş yıldızdan oluşur. Genellikle 1 ila 10 saatlik yörüngesel periyodlara sahip olup sisteminin tamamı yaklaşık bir Güneş boyutundadır. Bu çalışmada kataklismik değişen yıldızların genel özellikleri derlendi ve iki manyetik kataklismik değişen yıldızın (polar HU Aqr ve orta kutup V2069 Cyg) X-ışın ve hızlı-fotometrik gözlemleriden elde edilen sonuçlar sunuldu. Ayrıca OPTIMA (Optical Timing Analyzer) gözlemlerinde kullanılan polarimetre modunu kalibre etmek için polarizasyon ölçümleri ve bazı standart yıldızların polarimetrik gözlemleri yapıldı. Hızlı fotometrik ve polarimetrik gözlem verileri Skinakas gözlemevi (Girit)'de bulunan 1.3 m teleskop üzerine takılı OPTIMA ile elde edildi. X-ışın gözlemleri ise XMM-Newton ve SWIFT/XRT uyduları kullanılarak elde edildi. Işık eğrilerinin zamansal analizden V2069 Cyg sistemindeki baş yıldızın (beyaz cüce) dönüş frekansı hesaplandı ve her iki dalga boyunda (optik ve X-ışın) çift tepeli bir yayınım profiline sahip olduğu gözlendi. Burada sistemin çift tepeli bir yayınım profiline neden olan olası mekanizma tartışıldı. Ayrıca sistemin X-ışın tayf analizi yapıldı. Bununla birlikte, tutulma gösteren yakın çift yıldız sistem olan HU Aqr'nin yörüngesel periyodunun uzun dönemli değişimleri incelendi. Bu kaynak için literatürde bulunan tüm tutulma zamanları ile bu çalışmada elde edilen yeni tutulma zamanları birleştirilerek sistemin O-C (gözlenen eksi hesaplanan) eğrileri oluşturuldu ve dönem değişimleri analiz edildi. Ayrıca bu değişime neden olabilecek olası mekanizmalar tartışıldı.

Anahtar Kelimeler: Manyetik Kataklismik Değişenler, V2069 Cygni, HU Aquarii, OPTIMA, Foto-polarimetri.

ACKNOWLEDGEMENTS

First of all I would like to express my thanks and sincere appreciation to my supervisor Prof. Dr. Aysun AKYÜZ (University of Çukurova), Dr. Gottfried KANBACH (MPE, Max-Planck-Institut für extraterrestrische Physik, Garching, Germany, MPE) and Dr. Agnieszka SLOWIKOWSKA (University of Zielona Gora, Poland) for their scientific guidance, encouragement and support throughout my PhD, and their kind assistance in the preparation of this thesis.

It is also a pleasure to express my deepest gratitude to Dr. Gottfried KANBACH, Prof. Dr M. Emin ÖZEL and Prof. Dr. Aysun AKYÜZ for their careful reading portions of an earlier draft of this thesis and helpful feedback.

Many thanks to Dr. Frank HABERL who make time for me and taught me a lot about X-ray data (XMM-Newton) analysis and interpretation, and to my office-mate Abdullah YOLDAŞ whenever I need for his advice and help in software problems and for his friendship during my stay at MPE.

During my visit to MPE, University of Zielona Gora and Skinakas Observatory I have also met collaborations and support staff who help me a lot, therefore I would like to thank especially Fritz SCHREY, Alexander STEFANESCU, Martin MÜHLEGGER, Arne RAU, Hüseyin CİBOOĞLU, Andrzej SZARY, and special thanks to Agnieszka SLOWIKOWSKA, Krzysztof KRZESZOWSKI (Chriss) and all my Polish friends for their help, friendship and spending great time during my stay at Zielona Gora.

Thanks also to all the funding projects, most notably ASTRONS (EU FP6 Transfer of Knowledge Project 'Astrophysics of Neutron Stars', MKTD-CT-2006-042722) and its team, ERASMUS (European Union project), The Foundation for Polish Science grant FNP HOM/2009/11B, and OPTIMA (MPE) that have paid my trip and stay during my visit to MPE, University of Zielona Gora and Skinakas Observatory.

I would like extend special thanks to all my friends, especially Kamuran KARA, Volkan TAYLAN, Semiha İLHAN, Eda SONBAŞ, Ania SKRZYPCZAK, Durmuş TAKTUK and Emin KAYNARPINAR for their help, moral support, understanding and friendship during my studies, and director of UZAYMER (Space Science and Solar Energy Research and Application Center) Assistant Prof Dr. Nuri EMRAHOĞLU and the staff Utkan TEMİZ and Selami ÖZBAY for their help during my works in UZAYMER.

Finally, I will forever be grateful to my parents, sisters and brothers for their love, understanding and supporting me all the time. Therefore, I dedicate this thesis to my family.

The works of this dissertation is based on the papers in part or in full '**Nasiroglu** et al., 2010, in High Time Resolution Astrophysics (HTRA) IV-48. The orbital ephemeris of HU Aquarii observed with OPTIMA. Are there two giant planets in orbit?; **Nasiroglu** et al., 2012. Very fast photometric and X-ray observations of the intermediate polar V2069 Cygni (RX J2123.7+4217). Monthly Notices of the Royal Astronomical Society, 420, 3350-3359; Gozdziewski and **Nasiroglu** et al., 2012. On the HU Aquarii planetary system hypothesis. Monthly Notices of the Royal Astronomical Society. 2012arXiv1205.4164G'.

TABLE OF CONTENTS **PAGE**

LIST OF TABLES **PAGE**

LIST OF FIGURES **PAGE**

ACRONYMS

APD	:	Avalanche Photo-Diode
AROLIS	:	ARtificial OPTIMA LIght Source
AU	:	Astronomical Unit
BAT	:	Swift/Burst Alert Telescope
bbody	:	Black Body
BJD	:	Barycentric Julian Date
CCD	:	Charge-Coupled Device
CN	:	Classical Nova
CNO	:	Carbon-Nitrogen-Oxygen
CO	:	Carbon-Oxygen
CV	:	Cataclysmic Variable
d	:	Day (Unit of Time)
DAQ	:	Data Acquisition
DN	:	Dwarf Nova
EPIC	:	European Photon Imaging Camera
ESA	:	European Space Agency
EUV	:	Extreme Ultraviolet
EW	:	Equivalent Width
FFT	:	Fast Fourier Transform
GCN	:	GRB Coordinate Network
GPS	:	Global Positioning System
GRB	:	Gamma Ray Burst
HST	:	Hubble Space Telescope
INTEGRAL	:	International Gamma-Ray Astrophysics Laboratory
IP	:	Intermediate Polar
IR	:	Infra-Red
IUE	:	International Ultraviolet Explorer

LED	:	Light Emitting Diode
LTT	:	Light Travel Time
mCV	:	Magnetic Cataclysmic Variable
min	:	Minute (Unit of Time)
MONET	:	MOnitoring NEtwork of Telescopes
MPE	:	Max-Planck-Institut für extraterrestrische Physik
$M_\odot$	:	Solar Mass
NL	:	Nova Like System
O−C	:	Observed minus Calculated
OM	:	Optical Monitor
ONe	:	Oxygen-Neon
ONeMg	:	Oxygen-Neon-Magnesium
OPTIMA	:	OPtical TIMing Analyzer
PMT	:	Photo-multiplier Tube
QE	:	Quantum Efficiency
RN	:	Recurrent Nova
ROSAT	:	ROntgen SATellite
RXTE	:	Rossi X-ray Timing Explorer
$R_\odot$	:	Solar Radius
s	:	Second (Unit of Time)
SN	:	Supernova
TNR	:	Thermonuclear Runaway
UT	:	Universal Time
UTC	:	Coordinated Universal Time
UV-OT	:	Ultraviolet/Optical Telescope
WD	:	White Dwarf
yr	:	Year (Unit of Time)
XRT	:	Swift/X-Ray Telescope
XMM-Newton	:	Multi Mirror Satellite

1. INTRODUCTION

The changing nature of the sky has attracted the attention of people for centuries and it has always been a subject of interest and curiosity for them. When we look at the night sky with naked-eye, we may see some of the brightest stars and a few of the planets in our Solar System. But, if we look with telescopes we can see many of these stars. The observations made with the optical telescopes for centuries have shown that about half of all stars are binary stars and most of these binaries are interact with each other. However, during these observations some periodic variations in brightness have been observed in many of these stars. In general, due to the variations in their light, these stars are called 'Variable Stars'. Over the years, astronomers have obtained the 'light curves' of the stars by investigating the changes in their brightness. A light curve of a star contains a lot of information about its nature, type, physical properties, internal structure, and also contain information about its evolution in time. For this purpose, the light of the variables stars are measured from many part of the world by the astronomers using space- and ground-based telescopes and instruments, and, the obtained data is carried out by applying several different analysis methods.

Variables stars are divided into two general categories based on the variability in their brightness with time, as 'extrinsic' and 'intrinsic' variables. Extrinsic variables are stars in which the variability is caused by geometrical changes like the eclipse of one star by another (eclipsing binaries) or the effect of stellar rotation (rotating binaries). Intrinsic variables are stars in which the variability is caused by physical changes occurring inside the star or stellar system. The Intrinsic variables are divided into two subgroups: pulsating and eruptive-explosive variables. The pulsating variables show periodic or irregular expansion and contraction in their outer layers which result in variations in their brightness, temperature, spectrum and radius. However, the eruptive and explosive (or cataclysmic) variables are flare-up or sometimes explode suddenly and violently. This cause an extreme increases in star's luminosity and an ejection of material into space. These subgroups can further be divided into specific

classes of variable stars.

Cataclysmic Variable (CV) stars which undergo a cataclysmic change is a subgroup of intrinsic variables generated based upon the presence of change in their internal characteristics (like temperature, density, pressure and etc.). CVs have been a popular subject among both amateur and professional observers for many years. The word *'Cataclysmic'* is derived from the ancient Greek word *'Kataklysmos'* which means flood, storm or disaster. The CVs were interpreted as disaster due to their violent explosions and sudden release of energy into surrounding space.

In spite of the first discovery of a dwarf nova (U Geminorum) which was in 1855, the main descriptions which have provided understanding the nature and structure of CVs had started in 1960s. Since then CVs were confirmed to occur in binary star systems. Compared to the violence of explosions of Supernovae which is a catastrophic events towards the end of the star's life, the CVs have too weak explosions and sometimes can reoccurs one or more times.

Cataclysmic variables are interacting close binary systems in which relatively normal star is transferring mass to its compact companion. The companion star is often referred to as the 'donor' or the 'secondary' star, and the white dwarf (WD) as the 'primary' star. The secondary star generally is a cool late-type star near or on the main sequence. In rare cases, the system contains a giant star or another degenerate WD as a secondary. The transferred material, which is usually rich in hydrogen, forms in most cases an accretion disk around the WD. Some of them have occasionally a violent outburst caused by the nuclear fusion reaction as a result of the high density and temperature at the bottom of the accumulated hydrogen layer. The entire binary system is typically small and has the size of the Earth-Moon system with an orbital period in the range $1-10$ h.

Cataclysmic variables radiate in all parts of the electromagnetic spectrum from gamma-rays to radio waves, hence they have been studied extensively with ground-based (Keck, VLT, NOT, Mt.Skinakas, ESO, Calar Alto, SAAO, etc.) and space-based telescopes (like ROSAT, Rossi-XTE, Chandra, XMM-Newton, Swift, IUE, HST, etc.) so far. The gamma-rays are emitted by decays of some radioactive nuclei during nova

outbursts. The X-ray and ultraviolet observations give information from hot part of the inner region of the accretion disk. The infrared light comes from the secondary star and from optically thin plasma of the accretion disk. The optical radiation comes from the outer region of the accretion disk and from the secondary star. Finally, the radio emission arises as a result of thermal bremsstrahlung emission from electrons in the magnetosphere of WD and from the ionized gas in the ejected shell during the explosions.

Cataclysmic variables can be divided into several smaller classes based on their light curves, period, temperature, brightness and observed outburst behavior. These subclasses are classical novae, dwarf novae (with two subclasses named Z Cam and U Gem or SS Cyg), recurrent novae, symbiotic stars, nova-like systems and supernovae. The classical novae have an outburst which is caused by thermonuclear fusion with brightness of about $6-9$ magnitude and recurrence period of 10^4-10^5 yr, therefore they can be observed only one time for one binary system. The recurrent novae can have more than one recorded classical nova like outbursts repeating every 10 to 100 yr (with brightness of about $4-9$ magnitudes). The dwarf novae show normal- and super-outbursts with a recurrence times of $20-300$ d, due to the release of gravitational potential energy caused by the mass transfer through the disk. The nova-like variables are non-eruptive subclass of CVs. They are named as nova-like variables due to typical features of their light curves and spectra which are similar to those classical novae and dwarf novae.

Additionally, there is a type of CVs which contains a WD with a strong magnetic field, and they are known as Magnetic Cataclysmic Variables (mCVs). These short period binaries are divided further into two subclasses based on the strength of their magnetic fields: polars (or AM Her) and intermediate polars (IPs; or DQ Her). In polars, the WD is highly magnetized which either rotates synchronously with the orbital motion and prevents the formation of an accretion disk around the WD. In IPs, the WD has weaker magnetic field, and therefore rotates asynchronously with the orbital motion. The mass accretion in these systems occurs through a disk, which is disrupted in the inner region by the magnetic field.

This thesis present the results of investigation in optical and X-ray bands of two mCVs observed with ground (Mt. Skinakas Observator, Crete, Grecee) and space-based (XMM Newton and Swift/XRT) telescopes. This first chapter begins with a brief introduction to Binary Stars. Following the 'Introduction' Chapter 2. contains a review of previous work summarizing several different subtypes of CVs with their properties. Chapter 3. describes the OPTIMA instrument with its data acquisition software, calibration and polarization measurement obtained during observation campaigns at the Skinakas Observatory. Chapter 4. refer the X-ray and optical (OPTIMA) observations, data analysis and results of the two mCVs (Intermediate Polar V2069 Cyg and Polar HU Aqr). Finally, Chapter 5. contains discussion of the results and an overall conclusion of the thesis.

2. PREVIOUS WORK AND ASTROPHYSICAL TARGETS

This part contains a comprehensive review of previous work, summarizing magnetic CVs and other different subtypes of CVs with their properties.

2.1. Cataclysmic Variables

Cataclysmic variables constitute a wide class of binary star systems. In some cases, their brightness increase by a large factor, then drop back down to a low state. There are probably more than a million of these CVs in the galaxy, but only several hundreds of those close to our Sun have been studied in different wavelengths from gamma rays to radio waves. In these interacting close binary systems, the material is transferred from a Roche-lobe filling low-mass companion and is accreted by a white dwarf. The companion star is often called as the 'donor' or the 'secondary' star, while the WD is the 'primary'. The secondary is generally a cool late-type star near or on the main sequence, with a spectral type of K, M or G. In rare cases, these semi-detached binary systems may contain a giant star or another degenerate WD as a secondary. The accreted material, which is usually rich in hydrogen, forms in most cases, an accretion disk around the WD. During the accretion process, strong UV and X-ray emissions are often observed. Some of them have occasionally a violent outburst caused by the nuclear fusion reaction as a result of the high density and temperature at the bottom of the accumulated hydrogen layer on the primary. In these thermonuclear processes, the hydrogen layer is converted rapidly into helium. In general, each CV has an outburst form with a different characteristic. If a WD accumulates enough material until its mass reaches to the Chandrasekhar limit, the increasing interior density of accumulated material can ignite a runaway carbon fusion and may trigger a type-Ia Supernova (SN Ia) outburst, which is the brightest of all supernovae types (these are also the types used in cosmological searches, due to their well defined intensities). The entire binary system is typically small and has the size of the Earth-Moon system with an orbital period in the range $1-10$ h. CVs lead us to understand the evolutionary processes of

the accretion disk and mass transfer processes that exist in the universe. These low-mass system of objects also include well known subclasses such as Classical Novae (CNe), Dwarf Novae (DNe), Recurrent novae(RNe), Symbiotic Stars, Nova-Like Systems (NLs) and Supernovae (SNe). Additionally, there is a subclass of CVs containing a WD with a strong magnetic field (see Section 2.3); these are known as Magnetic Cataclysmic Variable Stars, mCVs (Warner 1995; Hellier 2001). We will now summarize each subclass mentioned.

Classical Novae;

The Classical Novae are mostly referred to only as the 'nova'. Novae are short-period binary systems containing a WD and a cool-low-mass main sequence star. In CN systems, the secondary star expands and fills its Roche lobe during its evolution. When the Roche lobe overflows, the secondary will lose material from its outer atmosphere, and then hydrogen-rich material will be accreted ($\sim 10^{-9}$ $M_\odot$ yr^{-1}) by the WD through the inner Lagrangian point, L1. Meanwhile, according to the principle of conservation of angular momentum, the flowing material will not fall directly on WD, but will form a disk around it. Then, during this process the intense gravity of the WD will compactify the material on the WD surface and heat it to very high temperatures. The accretion of the material, which is accumulated around WD, will continue pressing until pressure and temperature rise high enough ($10^7 - 10^8$ °K) to trigger the hydrogen fusion reactions. At these temperatures, hydrogen burning reactions occur via the well known CNO (Carbon-Nitrogen-Oxygen) cyle. Through this thermonuclear processes the hydrogen layer is converted rapidly into helium and the atmosphere of the degenerate WD will continue to expand, then a violent nova outburst occurs on the WD surface. Briefly, the nova outburst is a thermonuclear runaway (TNR) explosion of hydrogen-rich material on the WD surface. In summary, a TNR begins with the conversion of the hydrogen into helium under a critical pressure ($\sim 10^{20}$ dyne cm^{-2}) at the bottom of the accreted layers on the WD. A sudden release of nuclear energy throws the accreted material layers out of the WD surface. As a result, about $10^{-5} - 10^{-4}$ $M_\odot$ of material is ejected quickly with velocities from 100 to few 1000 km s^{-1}. The apparent (visual) brightness of the outburst can be in a range of 6 to 19 magnitude. Close their

maximum brightness, these systems have a spectrum similar to an A or F type giant star. Depending on the binary system parameters (accretion rate, composition of the envelope and the white dwarf mass), the outbursts can show different characteristics in their light curves, the duration times and expansion speeds of material and recurrence periods. The recurrence period of an outburst of CNe could be as long as $10^4 - 10^5$ yr; therefore they can only be observed once for one binary system (Shara 1989; Warner 1995; Gehrz et al. 1998; Starrfield et al. 1998; Kato 2002; Townsley & Bildsten 2005).

Recurrent Novae;

Recurrent Novae are a small subclass of CVs which can have more than one recorded classical nova-like outbursts. When a CN shows a second outburst, it is classified as a RN. The recurrence period of the outbursts varies in irregular intervals ranging from 10 to 100 yr (with brightness of about 4 to 9 magnitudes). Their outbursts show usually a very rapid evolution and may last from 10 d to several months (with a rate of decline of ~ 0.3 mag d^{-1}). A part of them contain a giant secondary with a large mass transfer rate ($\geq 10^{-8}$ $M_\odot$ yr^{-1}) and their WD mass is close to Chandrasekhar limit ($\sim$1.38 $M_\odot$). In RNe systems, the material collected on the accretion disk could be $\sim$10 times less than the classical novae. Because of the difference in the nature of the binary system and their outburst mechanism, this class is considered to be a heterogeneous group. The outburst mechanisms have been proposed to occur from TNR in the accretion layers on massive WDs or perhaps due to the instabilities of mass transfer from a giant companion. Theoretical assumptions and observations of the RNe have shown that only some part of the accreted material is ejected (with $V_{exp} \geq 300$ km s^{-1}) during the explosions. However in some RN systems, the WD may continue to accrete material until its mass reaches the Chandrasekhar limit. In such systems, this event might evolve to become a type Ia Supernova outburst.

RNe systems are subdivided into two classes: **long** period systems with a few 100 d (T CrB, RS Oph, V 3890 Sgr ve V745 Sco) and **short** period systems less than 2 d periods (i.e., U Sco, V394 CrA, LMC 1990♯2, T Pyx, Cl Aql ve IM Nor). The long period systems consist of a red giant secondary similar to Symbiotic Novae and the short period systems contain an evolved main sequence secondary similar to CNe

systems. The outbursts of short period systems are powered by TNR, while the long period systems are accretion powered events (Starrfield et al. 1985; Webbink et al. 1987; Starrfield et al. 1988; Anupama & Mikolajewska 1999; Anupama 2002; Kato 2002; Anupama 2008).

Dwarf Novae;

Another subclass of CVs called Dwarf Novae, consists of a WD primary and a low-mass main sequence secondary with an orbital period in a range from 80 min to 180 d. In these systems an accretion disk is created around the WD due to the angular momentum of the transferred material from the companion star. During the quiescence, the accretion rates range from 10^{-12} to 10^{-10} $M_{\odot}$ yr^{-1}. These systems show normal- and super-outbursts with a recurrence times of $20-300$ d, due to the release of gravitational potential energy caused by the mass transfer through the disk. Throughout the outbursts their brightnesses increase suddenly, with increase in the range of $2-7$ magnitudes, and last in a time interval from 2 to 20 d. The super-outbursts is thought to be triggered by a combination of thermal and tidal instabilities within the accretion disk, or by an enhanced rate of the mass transfer through to disk from the secondary. On the other hand, the normal outbursts originate at a constant mass transfer rate in the accretion disk. The super-outbursts show, in their light curves, a super-hump caused by the precession of the accretion disk at a period longer than the orbital period, and they have larger amplitude and longer durations than normal outbursts.

According the morphology of their light curves, DNe are divided into three subtype. These are SS Cygni (or U Geminorum) stars exhibiting normal outbursts, Z Camelopardalis stars exhibiting normal outbursts and following standstills, and SU Ursae Majoris stars exhibiting super-outbursts and normal outbursts (Cannizzo 1993; Warner 1995; Lasota et al. 1995; Osaki 1996; Urban & Sion 2006).

Nova$-$Like Variables;

There is a non-eruptive subclass of CV with higher mass transfer rates ($\sim 10^{-9}$ ile 10^{-8} $M_{\odot}$ yr^{-1}) than that in quiescent DNe. Such CVs are frequently named Nova-Like Variables due to typical features of their light curves and spectra which are similar to those CNe and DNe. In contrast with DNe systems, they have a constant

mass transfer rate through the disk, which, most of the time, causes their disk to be hot and fully ionized. NLs are $\sim$3$-$4 magnitudes brighter than DNe of the same orbital period and they vary in brightness with only a very small amplitude. It is thought that because of exceeding the upper stability limit (typically, $\dot{M} \sim 6 \times 10^{-9}$ $M_{\odot}$ yr^{-1}), they show constant brightness. Some of these systems show stunted outbursts due to DN-type disk instabilities.

NLs can be divided into a number of subclasses like AM CVn (AM Canum Venaticorum) stars, DQ Her (DQ Hercules) stars, AM Her (AM Hercules) stars and UX Uma (UX Ursae Majoris) stars. AM CVn stars are binary systems consisting of a degenerate C-O (Carbon-Oxygen) WD and a low-mass semi-degenerate WD secondary. In general, their chemical composition does not contain hydrogen. In these systems dynamical effects such as orbital motion and mass accretion cause the light curve to change. DQ Her stars contain a WD and a cool secondary star near the main sequence. AM Her stars, usually host a WD and sub-giant secondary star near the main sequence. UX UMa stars have bright accretion disk due to high mass transfer rate. Some of them are similar to the novae in case of minimum brightness and an eclipse effect is seen in their light curves (Horne 1993; Smak 1994; Warner 1995; Ringwald & Naylor 1998; Honeycutt et al. 1998; Honeycutt 2001; Froning et al. 2003; Nagel et al. 2004; Dobrotka et al. 2011).

Symbiotic Stars;

Symbiotic Stars (Z Andromedae Variables) are long-period binary systems, which show irregular photometric changes. They consist of a cool red giant (usually M spectral type) and a hot main sequence star (or usually a WD with accretion disk, subdwarf or neutron star). Their orbital periods are typically between 200 and 1000 d (and some of them significantly larger). The mass transfer from the red giant to hot compact companion occur via accretion from the stellar wind or in some cases could be from Roche-lobe overflow. During this process, the system become a very hot ($\sim 10^5$ $^{\circ}$K) and luminous ($\sim 10^2 - 10^4$ $L_{\odot}$); radiation source is powered by quasi-steady nuclear shell burning on the WD surface. These systems can be characterized by two main phases based on their energy generation (quiescent and active) phases. During the

'quiescent phase', the hot component releases its energy at an approximately constant rate and spectral distribution, as well as the 'active phase' is characterized by a significant change in the hot component radiation with a few magnitudes brightening in the optical and a high-velocity mass ejection. There are two distinct types of Symbiotic stars; S-type (Stellar), which contain normal M-type red-giants with an orbital period of about $1-15$ yr and accretion rate of $\sim 10^{-8}-10^{-7}$ $M_{\odot}$ yr^{-1}, and D-type (Dusty), which contain Mira variables surrounded by warm dust with an orbital periods usually longer than 10 yr and accretion of $\sim 10^{-6}-10^{-5}$ $M_{\odot}$ yr^{-1}. They have outbursts (with amplitudes of $1-3$ magnitude and variation timescales from minutes to decades) arise from steady nuclear burning of accreted material on the surface of WD triggered by instabilities in the accretion disk or TNR. It is suggested that some symbiotic systems with a WD close to the Chandrasekhar limit might evolve to become SN Ia (Kenyon 1988; Muerset et al. 1991; Warner 1995; Mikolajewska 2003; Skopal et al. 2004; Tang et al. 2011; Mikolajewska 2011).

Supernovae;

Supernovae are systems showing a sudden explosion and a large increase in their brightness (with a range from 16 to 20 magnitudes). In principle, they are similar to Novae with much larger explosions, and they can be classified as a member of CVs due to their sudden explosions. SNe provide important information in determining the fundamental cosmological parameters and distances beyond our own Galaxy. In addition, they contribute heavy elements to the richness of the interstellar medium, and by this way they may trigger the formation of new stars with the ejected material. SNe can be divided into two classes (Type I and Type II) based on shape of the light curves and spectrum of their explosions. The light curves of Type I supernovae (SN I) are very similar to each other and their optical spectra do not contain hydrogen Balmer lines. They are seen to occur among middle-aged and older populations of stars placed in elliptical and spiral galaxies. SNe Type I can also be subdivided in to three classes: Type Ia , Type Ib and Type Ic. Type Ia occur on a WD close to Chandrasekhar limit as a result of TNR in a close binary system and they contain strong silicon lines in their spectrum. For a few weeks the explosions can look nearly as bright as its own

galaxy. Type Ib and Type Ic appear as a result of core collapse of massive stars, and they contain strong and weak helium lines in their spectrum, respectively. Type II supernovae occur only in spiral galaxies as a result of core collapse of massive young stars. Hydrogen lines are seen in their spectrum. SNe Type II also subdivided into two classes based on their light curves: Type II-P and Type II-L. In light curves of Type II-L are seen a **linear** decline for few weeks just after the initial maximum light, while in Type II-P are seen a constant **plateau** for about 3 months shortly after the decline from initial maximum light. The best example for Type II-P are Kepler's SN 1604 and SN 1987A observed in Large Magellanic Cloud (Barbon et al. 1979; Doggett & Branch 1985; Wheeler & Harkness 1990; Riess et al. 1998; Perlmutter et al. 1999; Percy 2007).

2.2. The Historical Background of CVs

It has become possible to identify typical features of nova explosions from the observations performed in the middle of 20^{th} century. For example, the presence of an explosion and ejection of a large portion of material at high speed have been found from the spectroscopic observations (Payne-Gaposchink 1957; McLaughlin 1960; Gallagher & Starrfield 1978). The physical conditions and chemical abundances of the ejected material of the novae explosions have been studied in different wavelengths (Gehrz et al. 1998). In all novae events it has been found a helium richness in the ejected material resulting from the hydrogen fusion which is strengthening the explosion (Starrfield 1989). In addition, the results of ratio of isotopic abundances from the analysis of the Murchison meteorite (Australia, 1969) showed the presence of presolar particles from earlier novae event (Amari et al. 2001).

The first observations, which have provided an understanding of the nature of the CVs, have started by discovering the short-period spectral binaries SS Cyg, AE Aqr and RU Peg (and other U Geminorum type of variable stars). The observations have shown that the general spectroscopic features of AE Aqr resemble those of SS Cyg and RU Peg. At minimum light they show a continuous spectrum with few or no

absorption features and wide emission lines of hydrogen, helium and ionized calcium. And, at maximum light the spectrum of many of stars was continuous, while others showed faint and very wide, diffuse absorption lines of hydrogen (Elvey & Babcock 1943; Joy 1954).

From the photometric observations, it has been found that DQ Her (1934) is a short-period (4.65 h) eclipsing binary with a periodic oscillations of 71 s and an amplitude of about 0.05 magnitude in its light curve. The presence of the oscillation has shown that there is a compact object (a WD) in the system. The origin of the 71 s oscillation has been suggested to results from pulsations of the WD (Walker 1954, 1956; Kraft 1959). Twenty years later, it has been proposed that the 71 s periodicity in DQ Her is provided by rapid rotation of an accreting WD. As a result of investigations, it has been estimated that all CVs are close binary systems in which a cool component fills its Roche lobe and transfers material through the inner Lagrangian point into an accretion disk (or ring) around the compact star. In binaries like DQ Her, the material accreted onto WD with a strong magnetic field from the surrounding disk. Then, the material channeled along the field lines and impacts WD atmosphere at each magnetic pole. Nevertheless the accretion onto the WD could produce a 'hot spot' at each pole which gives rise to soft X-ray and UV radiation (Crawford & Kraft 1956; Bath et al. 1974; Herbst et al. 1974; Patterson 1994).

Kraft (1964) has discussed some of the spectroscopic and photometric properties of 10 old novae. He found that these systems have membership in a certain type of close-binary systems which have the necessary condition for a star to become a nova consisting of a blue sub-dwarf and a red star. He, however, thought that the nova outbursts do not occur due to the thermal runaway in accretion layer on WDs. This idea was established on the high degeneracy of the material at the bottom of the accreted envelope on the WD. Kraft (1964) and Schatzman (1965) argued that, due to the degeneracy the high electron conductivity, the locally produced energy would fastly distribute throughout the interior (core) and therefore there would be no reactions to ignite the outburst. Schatzman (1965) has proposed that the burst may occur as a result of non-radial oscillation of the compact blue star. On the other hand, Starrfield

(1971) has suggested that there are convection and non-degenerate region in the envelope, and therefore a significant amount of energy would not transport into the interior. Thereupon, considering these conditions, the theoretical calculations have shown that, a TNR can occur in the envelope of a WD and can produce the energy observed during the nova outburst (Giannone and Weigert 1967; Starrfield 1971).

The theoretical assumptions and hydrostatic studies have shown that the characteristics of the outburst strongly depend on the mass of the WD. It has been argued that, in less massive WDs, only some part of the accreted material is ejected in the earlier stages of the explosion, and the remaining part in the envelope continues to nuclear burning and mass ejection for years. Therefore, the lower-mass WDs (< 1 $M_{\odot}$) could be responsible for the slow nova-like DQ Her and HR Del. In order to produce high mass ejection in a nova outburst on lower-mass WDs, the envelope should have a very high degree of the CNO enhancement and hydrogen-rich mass (Starrfield et al. 1972, 1974a,b). The subsequent investigations on the novae ejecta have confirmed the requirement of the enriched CNO nuclei for a fast nova and shown that the ejected material is rich in carbon, nitrogen and oxygen (Williams et al. 1978; Williams & Gallagher 1979; Gallagher et al. 1980). Afterward, it has been reported that a massive WD is necessary to produce a very fast nova or recurrent nova outburst (Starrfield et al. 1978, 1985, 1988).

Nevertheless, in the late 1970s, one-dimensional (1-D) hydrodynamic calculations have been used to study the TNR on WDs, the accretion mechanism, the chemical diffusion in the accretion material, the evolution of the WD through the burst, and the chemical composition of the ejecta (Prialnik et al. 1979; Shara et al. 1980; Prialnik & Kovetz 1984; Prialnik 1986). The main features of the accretion phase and the burst mechanism have been obtained for different initial conditions, and the nucleosynthesis in the ejecta has been studied in detail for carbon-oxygen (CO) and oxygen-neon (ONe) novae. The short-lived β^+ unstable nuclei (such as ^{13}N (τ=862 s), ^{14}O (τ=102 s), ^{15}O (τ=176 s), ^{17}F (τ=93 s) and ^{18}F (τ=158 min)) produced during hydrogen burning, and the medium- and long-lived radioactive nuclei (such as ^{7}Be (τ=77 d), ^{22}Na (τ=3.75 yr), and ^{26}Al ($\tau = 1.04 \times 10^6$ yr)) synthesized during nova explosions

have been discussed in some details. It has been suggested that the unstable proton-rich nuclei are transported by convection to the outer envelope where they decay and trigger the explosion; however, the medium- and short-lived radioactive nuclei are responsible for producing emissions of γ-rays when they decay (Hernanz & Jose 1998; Jose & Hernanz 1998; Gomez-Gomar et al. 1998; and reference therein).

In order to understand nature of the CVs and their outbursts, many studies have been done at all wavelengths from radio to gamma-rays. The optical observations of novae have been started in the 15^{th} century by naked eye, and since then a large number of observations have been performed and many new novae were discovered by astronomers. The Supernova 1572 and 1604 had been observed in details by Tycho Brache and Johannes Kepler, respectively. The first to reach naked-eye visibility Nova Ophiuchus was discovered by J.R. Hind (1848) and defined as a bright red star, and that the cause of this was thought to be due to intensely bright H_α emission. The first dwarf nova U Geminorum, which was observed for several d at the same brightness, was also discovered by J.R Hind in 1855. SS Cygni, the best studied one of variable stars since 1899. It was observed with photographic plates at Harvard College Observatory by Miss L. D. Well in 1896 (Warner 1995; Harland 2003).

The development of photoelectric photometry has been started with the introduction of the photomultiplier tubes in the mid of 1940s. The pioneering observation was made by A.P. Linnell (1949) with the 1.5 m reflector of the Oak Ridge Station of Harvard Observatory. The NL eclipsing binary UX UMa was observed at that time with an orbital period of 4.717 h. In these observations, this system showed the presence of intrinsic variations with amplitudes of $0.01-0.2$ magnitude which is a characteristic of CVs. Similar flickering had been also observed visually in the recurrent nova T CrB by E. Petit (1946), nova like variables AE Aqr by K. Henize (1947) and VV Pup by Thackeray et al. (1949). The light curve of eclipsing variable UX UMa obtained from both spectroscopic and photometric observations by Walker and Herbig (1954) was characteristic of most CV light curves over the period $1950-1968$. Their result was important for understanding nature of the CVs (Warner 1995; and reference therein).

The first spectroscopic survey on CVs has been started with the observation of recurrent nova T CrB using a visual spectroscope by W. Huggins in 1866. After that, a great number of spectroscopic observations have been so far performed to study the variations of the spectrum of CVs. By this way, several classification schemes have been developed for better interpretation of the evolution of the spectra of sources. The spectral observations of CV have provided a determination of their physical properties, a better understanding of exact nature of them and a classification based on their spectral characteristics (for review see Mumford (1967); Warner (1995); Augusteijn et al. (2010); Southworth et al. (2010); Szkody et al. (2011)).

The Hubble Space Telescope (HST) which is capable to observe in the visible, infrared (IR) and ultraviolet (UV) wavelengths was launched in 1990. The high time-resolution observations both spectroscopically (down to 30 ms integration time) and photometrically (10 ms integration time) have been made using the HST's instruments to study the physical condition and morphology of the ejected material around the novae, the CVs during quiescence, and the pre-Cataclysmic Variables. The HST has advanced the study of CVs because of its sensitivity in UV that provided by its size and the efficiency of its instruments. On the other hand, the temperature and pulsation properties of the WDs, and the linear polarization measurements (with a time resolution of 1 ms) of CVs have been also made using HST's instruments (Wood 1992; Sion et al. 2001; Krautter et al. 2002; Froning et al. 2003; Szkody et al. 2010).

In order to obtain the ultraviolet properties of CVs, a large number of observations have been performed with the International Ultraviolet Explorer (IUE). The high quality, fluxed, IUE spectra of CVs provided important information about the evolution of the nebular emission lines with time. As a result of these UV investigations, a second class of novae was identified. This class was ONe (ONeMg) novae that occurred on an oxygen-neon-magnesium WD. The first one of these classes was CO novae that occurred on a WD with a core composition of carbon and oxygen (Williams et al. 1985; Starrfield et al. 1986). From the UV studies (on the basis of IUE data archive), 51 CV systems have been showed that the spectral flux distribution of CVs does not depend on system type, orbital period, or average length of interval between outburst maxima (for

dwarf novae) and inclination, but strongly depends on the WD mass (Verbunt 1987). However, two new theoretical models have been developed for a better understanding of UV spectra of novae. The first one was the spherically symmetric, non-LTE, expanding stellar atmosphere code. It has been shown that the unidentified lines in the UV spectra were, in actuality, due to regions of transparency between overlapping absorption lines from the iron group elements. The second one, which was used to study novae ejecta in which the spatially unresolved shell, was an optimization technique in combination with the large-scale spectral synthesis code CLOUDY (Hauschildt et al. 1992, 1997; Starrfield 2002; and reference therein).

The first comprehensive ground-based infrared observations of CV have been made for Nova Serpentis 1970 (FH Ser) during its outburst (Geisel et al. 1970). IR photometry of FH Ser was obtained over the period from 19 to 111 d after its discovery, and it was one of the brightest infrared stars in the sky. The IR observations of this source and subsequent novae has shown that the thermal re-radiation by dust grains in the nearby region of the system is a common and normal feature of the nova event (Bode & Evans 1980). It has been suggested that near-IR light curves can be used for distinguishing the ONeMg novae with coronal activity from those CO novae that produce plenty of circumstellar dust. IR observations of novae have shown that they create optically thick circumstellar dust shell composed largely of carbon grains, and their IR spectral energy distributions are dominated by strong thermal emission from dust. These thick dust shell formation events also appear in CO novae (Gehrz 1988; Gehrz et al. 1995, 1998). Infrared broad-band observations of CVs over several years were useful to understand the origin of their infrared light and to predict some of their physical parameters like system distance, mass and spectral type of the secondary, and disk temperature (Tanzi et al. 1981; Jameson et al. 1982; Mateo et al. 1991; Rodrigues et al. 2006). A subsequent work of IR observations of 28 CVs (DN and NLs in quiescence) has shown that the infrared light comes from the secondary star that supplies material to the WD companion, and from opaque material and optically thin plasma of the accretion disk that gives rise to the visual and UV emission lines (Berriman et al. 1985; and reference therein).

X-ray observations have provided important information about CVs and their outbursts. Long before the ROSAT (ROntgen SATellite) all-sky survey, it has been reported that most of CVs would be expected to be observable as X-ray sources. EX Hya was the first known CV which has been detected as X-ray sources (Warner 1972). Soft X-ray emission has been also detected from the dwarf nova RX And, SS Cyg and U Gem, and from Magnetic CVs such as AM Her and AN Uma (Rappaport et al. 1974; Henry et al. 1975; Mason et al. 1978; Bunner 1978; Hearn & Marshall 1979). The number of detections of CVs in the X-rays has started to increase consistently since the more sensitive satellites (Einstein, EXOSAT, ROSAT, BeppoSAX, Chandra, XMM-Newton, Swift and RXTE) started being used (O'Dell et al. 2010). An X-ray survey of 32 CVs have been made by using Imaging Proportional Counter (IPC) on the Einstein Observatory. These observations have made it possible to investigate in more detail the X-ray properties of CV and the mechanism which is responsible for their X-radiation. It has been suggested that the reason of the X-ray emission in CV sytems is the release of gravitational energy from the accretion onto the surface of the WD (Lamb & Masters 1979; Cordova et al. 1981; Becker & Marshall 1981; Becker 1981). Patterson & Raymond (1985) have discussed the hard and soft X-ray emission from CVs with the accretion disk, and they interpreted their results in a simple model of the disk boundary layer, where accretion gas settles onto the WD. According to their model, at low accretion rates ($< \sim 10^{-9}$ $M_\odot$ yr^{-1}) the hard X-rays are emitted by hot gas (at high temperatures near 10^8 K) in the optically thin portion of the boundary layer, and at higher accretion rates ($> \sim 10^{-9}$ $M_\odot$ yr^{-1}) the disk boundary layer becomes optically thick, and should emit most of its energy (about 10^{35} erg s^{-1}) in the UV/soft X-rays, with temperatures near 10^5 K.

In the 1990s, the X-ray satellite ROSAT performed the first imaging all-sky survey in the soft X-ray band. During the ROSAT mission several new CVs were discovered from the optical identification of X-ray sources (Van Teeseling & Verbunt 1994; Motch et al. 1996; Verbunt et al. 1997; Burwitz 1998; and reference therein). Many of these new systems were magnetic CVs (Polar and Intermediate Polars) which constitute a group representing about 25% of all CVs. The intermediate polars are

known to exhibit both soft and hard X-ray radiation, and are thought to be the brightest and hardest X-ray sources among CVs (Gaensicke et al. 2005; Barlow et al. 2006; Muno et al. 2006; Bonnet-Bidaud et al. 2007; Anzolin et al. 2008; de Martino et al. 2008; and reference therein). Observational studies of these interacting binaries have provided important information about their X-rays characteristics and outbursts. As a result of these studies, it has been proposed that there are different mechanism for producing X-ray radiation during the quiescence and outburst of CVs. The hard X-ray radiation could produced: 1) during the radioactive decay of ^{22}Na and ^{26}Al from Compton degradation of gamma-rays, 2) during the outburst by shocks which produce a thermal bremsstrahlung spectrum in the ejected wind or between the ejecta and the circumstellar medium, 3) shortly after or before the outburst, by the residual hydrogen burning occurs in a shell on WD, 4) during quiescence by shocks heating of accretion phenomena through a disk or magnetic field of the WD (Livio et al. 1992; Orio et al. 2001a,b; Orio 2004; Hellier et al. 2004; Balman 2005; and reference therein).

After the first radio detection of a nova outburst, the radio light curves of several CVs have been obtained and fitted using relatively simple spherically symmetric and isothermal models. The radio light curves typically show an initial rise due to optically thick ejecta followed by an optically thin decline. In general, CVs are weak emitters of radio emissions (Bode & Lloyd 1996). The first radio emission from CVs have been detected at wavelengths of 11.1, 3.7 and 1.95 cm from Nova Delphini 1967 (HR Del) and Nova Serpentis 1970 (FH Ser) by Hjellming & Wade (1970). Chanmugam & Dulk (1982) have reported the first discovery of radio emission from a magnetic CV system AM Her at 4.9 GHz using VLA (Very Large Array). They have suggested that the radio emission arises as a result of thermal bremsstrahlung emission and coherent or incoherent non-thermal gyro-synchrotron radiation generated by accelerated relativistic electrons (while the term synchrotron radiation used to describe emission from ultra-relativistic electrons) in the magnetosphere of WD. Following this discovery, many CVs have been observed in radio, and their radio emission mechanism have been discussed during their quiescent and outburst (Cordova et al. 1983; Dulk et al. 1983; Hjellming et al. 1986; Chanmugam 1987). Subsequent high-sensitivity radio

observations of magnetic (AM Her- and DQ Her-type) and non-magnetic CVs have revealed new information about the radio emission mechanism. It has been reported that GK Per has a non-thermal radio emitting shell which is not a common characteristic of classical novae. This radio emission has been interpreted as synchrotron emission from shocked circumstellar gas swept up by the nova ejecta similar to young supernova remnants. It has been suggested that the interaction between the disk wind (during the outburst) and the magnetosphere of the secondary star in CVs generates radio emission. These radio observations were important in term of identification of synchrotron-emission and for understanding the evolution of CVs and morphology of their outburst (Bode et al. 1987; Pavelin et al. 1994; Bode & Lloyd 1996; Bond et al. 2002; Warner 2006; Mason & Gray 2007; and reference therein).

Many years ago, it has been pointed out that the gamma-rays are emitted by decays of some radioactive nuclei (such as short-lived ^{13}N and ^{18}F and medium-and long-lived ^{7}Be, ^{22}Na and ^{26}Al) during nova outbursts (Clayton & Hoyle 1974; Clayton 1981; Leising & Clayton 1987). The emission of gamma rays from these radioactive nuclei occur since they emit positrons that annihilate with the surrounding electrons (e^+ - e^-), when the envelope is already becoming transparent to gamma rays. Complete evolution of various nova models have been computed with a continuously updated hydrodynamical code, including a complete network of nuclear reactions from the accretion phase up to the ejection (Hernanz & Jose 1998; Jose & Hernanz 1998; Gomez-Gomar et al. 1998; Hernanz et al. 1999, 2002; Jenkins et al. 2004; and reference therein). Gamma-ray observations of AE Aqr and AM Her (Magnetic CVs) have stimulated investigation of different scenarios for the gamma-ray production in CVs. In the case of IP V1223 Sgr, during the accretion process it has been suggested that accelerated hadrons are convected onto the WD surface and interact with dense material. As a result of these hadronic interactions, high energy gamma-rays are produced from decay of neutral pions (Warner 2006; Bednarek & Pabich 2011; and reference therein). Several observational studies have been performed last three decades to detect gamma-ray emission from novae, using OSSE, BATSE and COMPTEL instruments on-board CGRO; TGRS instrument on-board WIND; SPI and IBIS instruments on-board INTE-

GRAL; and BAT instrument on-board SWIFT; and GBM instrument on-board Fermi (Iyudin et al. 1995, 1999; Harris et al. 1999; Hernanz et al. 2000; Hernanz & Jose 2004, 2005; Senziani et al. 2008; Suzuki & Shigeyama 2010; and reference therein).

2.3. Magnetic Cataclysmic Variables (mCVs)

2.3.1. Polars and Intermediate Polars

mCVs are interacting close binary systems in which material flows through the inner Lagrangian point (L1) from a Roche-lobe filling low mass companion and falls towards a magnetized white dwarf primary (typically $0.7-1.2$ $M_{\odot}$), forming an accretion stream. These systems are known to be lie in the solar neighbours within a few hundred parsecs of the Sun and therefore they could be considered within the galactic disk. mCVs are ideal plasma physics laboratories to study the accretion and radiation processes for material under extreme astrophysical conditions including relativistic environments and magnetic field strengths. And, they provide a unique insight for a better understanding of magnetically funneled accretion flows in other astrophysical environments. These short period binaries usually included among the NLs with two subgroups based on the strength of magnetic fields of the WD: polars (or AM Her) and intermediate polars (IPs; or DQ Her). For detailed description see Cropper (1990); Patterson (1994); Warner (1995); Hellier (2001); Lasota (2004).

Polars (AM Her Stars);

In polars, the WD has a sufficiently strong magnetic field (B $\sim 10^7 - 10^8$ G) which locks the system into synchronous rotation (P_{spin}=P_{orb}). The strong field also leads to formation of an extended magnetosphere around the WD and a small separation between the WD and the secondary. Because of the magnetosphere extends beyond the L1 radius, the accretion material ($\sim 10^{-12} - 10^{-14}$ $M_{\odot}$ yr^{-1}) cannot orbit freely, and thus does not form an accretion disk around the WD, unlike in other non-magnetic CVs. In polars, the accretion process is widely thought to occur directly via an accretion stream from the secondary into the magnetosphere of the WD. When the

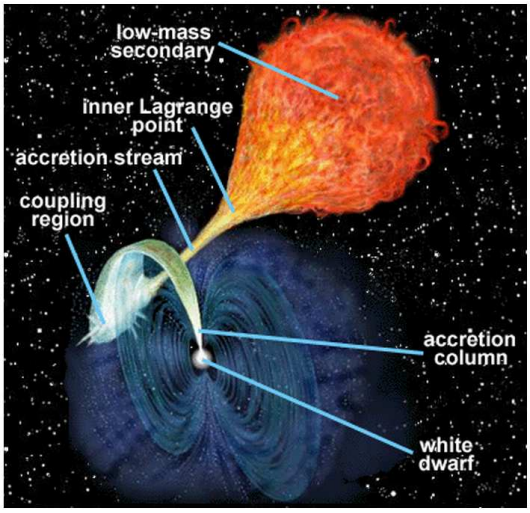

Figure 2.1. A schematic representation of the geometry and components of a polar. The material flows through inner Lagrangian point from the secondary, and falls along an accretion stream on a magnetized WD. When the accretion stream encounters the magnetosphere of the WD, it follows the magnetic field lines (blue) of the WD and plunges into the magnetic pole(s) [Adapted from Russell Kighttly Media (rkm.com.au)]

accretion stream encounters the magnetosphere, the strong magnetic field captures the material and force it to move directly along the magnetic field lines, towards one or both magnetic poles of the WD, forming a hot '*accretion spot*', (Figure 2.1.). The gas in the accretion stream is ionized by collisions and photo-ionized by UV and X-ray photons from the accretion region on the WD (Cropper 1990; Patterson 1994; Warner 1995; Hellier 2001; Lasota 2004).

There are presently more than 100 known polars which are cataloged by Ritter & Kolb (2003) in catalog version-2011. The confirmed members of them have an orbital/spin periods ranging from $\sim$77 min to 14 h, with V band magnitude in the range of 12 to 21. More than half of polars have a period below of the period gap (so called $2-3$ h). The secondary star in polars is in general a low mass red dwarf or a main-sequence star with possible range of 0.2 to 0.6 $M_{\odot}$. The magnetic fields in polars have been determined by different methods like cyclotron lines, Zeeman effect, optical polarimetry. Most of polars often show large-amplitude variations in their luminosity on a time scale of months to year. These variations usually referred to as 'high',

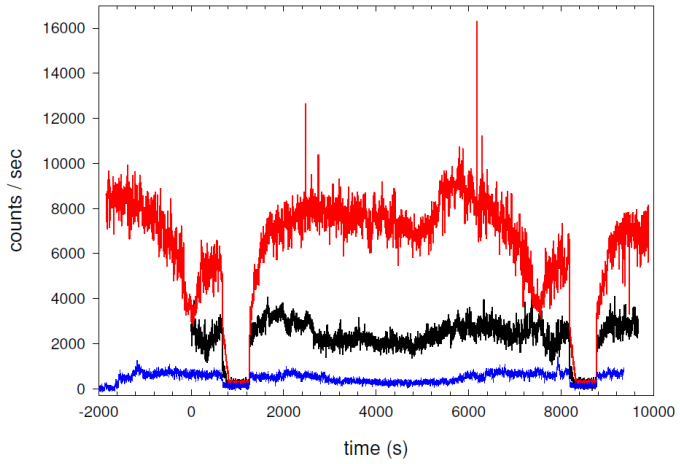

Figure 2.2. An example of light curves of various mass accretion rates in Polars. The light curves with 1 s resolution of the eclipsing polar HU Aqr at three epochs: July 5, 2000 (upper curve, red) in a high state of mass accretion from the secondary, Sep 21, 2001 (middle curve, black), in a intermediate state of mass accretion, and July 18, 2004 (lowest curve, blue) in a low state of mass accretion. The observations data obtained with OPTIMA at Skinakas observatory, Crete, Greece. [Taken from Kanbach et al. (2008)]

'intermediate' and 'low' states of accretion, which are due to episodic changes of the mass accretion rates from the secondary (Figure 2.2.). Currently it has been known 7 of asynchronous polar systems in which the WD spin period slightly different from the system orbital period by $\sim 1-3$ percent, like V1432 Aql, V1500 Cyg, By Cam and CD Ind (Warner 1995; Wickramasinghe & Ferrario 2000; Gaensicke et al. 2004; Mouchet et al. 2012).

Intermediate Polars (IPs, DQ Her Stars);

In intermediate polars, the magnetic field of the WD is one or two order of magnitude weaker (B $\sim 10^6 - 10^7$ G) than polars with larger orbital separation, therefore insufficient to force the WD to spin with the same period as the binary system orbit ($P_{spin} < P_{orb}$). Due to their weak magnetic field, these systems have smaller magnetosphere than the polars, and therefore the mass accretion ($\sim 10^{-10} - 10^{-8}$ $M_\odot$ yr^{-1}) occurs through a disk (or an accretion stream) which is disrupted in the inner region by the magnetic field up to the magnetosphere edge where the pressure of the accretion gas stronger than the pressure of the magnetic field. From this point the

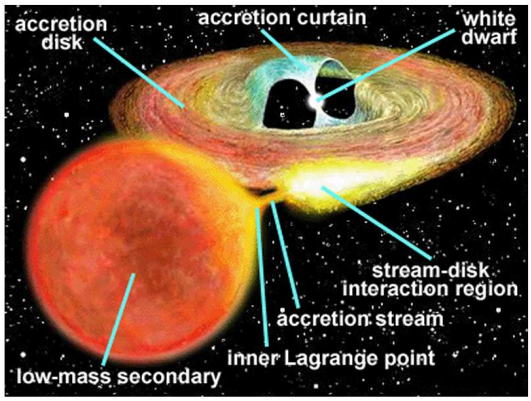

Figure 2.3. A schematic representation of the geometry and components of an intermediate polar. The material flows through inner Lagrangian point from the secondary, and falls along an accretion stream on the WD. The infalling material forms an accretion disk around the white dwarf, truncated at its inner edge by the magnetic field of WD. When the material in the accretion disk reaches the WD, the accretion flow becomes channeled towards the magnetic poles of the WD by the magnetic field, forming an accretion curtain. [Adapted from Russell Kighttly Media (rkm.com.au)]

accretion flow becomes channeled towards the magnetic poles of the WD by the magnetic field, forming'*accretion curtains*' (Cropper 1990; Patterson 1994; Warner 1995; Hellier 2001; Lasota 2004), see Figure 2.3.

Since starting to use more sensitive X-ray satellite, the number of detections of CVs has increased steadily. In recent years, a growing number of magnetic CVs have been detected by hard X-ray telescopes such as *INTEGRAL*/IBIS and *Swift*/BAT, and many of them were identified as IP (Landi et al. 2009; Brunschweiger et al. 2009; Bernardini et al. 2012). There are 36 confirmed, 20 probable, 26 possible IPs cataloged in Mukai (2011) catalog (version Jan. 2011)[1] . This number of IPs has updated in Section 5.1.2 (see Figure 5.6. and Table 5.2.) as 39 confirmed IPs with known spin and orbital periods. These systems contain a low mass secondary near the main sequence with a mass range of 0.1 to 0.5 $M_{\odot}$. The orbital period of these systems range from 1.38 to 48 h with typical values between 3 and 6 h, and the spin period of the WDs range from 33 to 4021 seconds with spin-to-orbital period ratios (P_{spin}/P_{orb}) ranging from 9×10^{-4} to 0.68. There are 5 systems with orbital period below the gap and only

[1] http://asd.gsfc.nasa.gov/Koji.Mukai/iphome/iphome.html

one system lies in the period gap. Only eight IPs have been found to emit circularly polarized light. Those IPs are: BG Cmi, PQ Gem, V2400 Oph, V405 Aur, V2306 Cyg, 1RXS J173021.5-055933, RX J2133.7+5107, and NY Lup (Katajainen et al. 2010; Potter et al. 2012; and reference therein).

2.3.2. Fundamental Properties of mCVs

In mCVs, a fraction of the gravitational potential energy of accreted material can be converted into radiation, give rise to an accretion luminosity which could be very larger than the energy produced through nuclear fusion in the core of normal stars. In these systems, the magnetically channeled material towards WD magnetic poles, accelerating as it falls (with supersonic velocities, about few 1000 km s^{-1}) and undergoes a strong shock at some distance from WD surface, and heated to temperatures about 10^8 K, then cools, producing hard X-ray/soft gamma-ray emission from the thermal bremsstrahlung cooling processes by free electrons in the hot post-shock region ($kT_{brm} \sim 10-60$ keV), and cyclotron emission ($kT_{cyc} \sim 2-30$) keV in the optical and infrared (Figure 2.4.). Additionally, the illuminated photosphere of the WD, either by thermal emission or reprocessed hard X-ray emission from the accretion column, emit a quasi blackbody radiation which is prominent at EUV (extreme ultraviolet) and soft X-ray ($\sim kT_{bb}$ 25-100 eV) wavelengths (Burwitz 1997; Warner 1995; Lasota 2004; Evans & Hellier 2007; Bernardini et al. 2012; and reference therein).

IPs have higher mass transfer rates, higher intrinsic absorption and larger accretion area than polars. They are known to exhibit both soft and hard X-ray emission. They are thought to be the most luminous and the hardest X-ray sources among accreting WDs, due to their typically higher mass transfer rates. In hard X-rays, these objects seem to be more luminous up to the factor of 10 than polars which are strong emitters of soft X-rays. Additionally, some of IPs emit weak circularly polarized optical-IR light arising from accretion shocks, while all polars emit both strong linear and circular polarization of the optical and near-IR radiation, which is believed to arise as a result of cyclotron emission processes in the accretion columns. In polars, the cy-

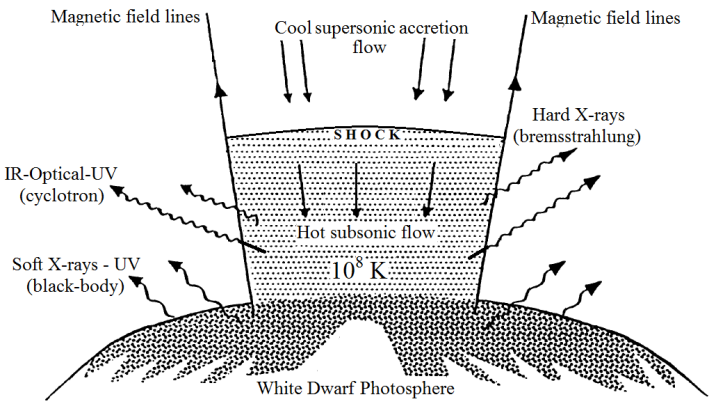

Figure 2.4. Schematic figure of a standard accretion column geometry for a magnetized WD and a part of its surface. The ionized gas infalling along the magnetic field lines with supersonic speeds encounters a shock above the surface of WD, and emit its energy in the X-rays, Optical, IR and UV. [Adapted from Patterson (1994)]

clotron radiation is an important cooling mechanism, which suppresses the high temperature bremsstrahlung emission of a substantial fraction of the electrons in the shock region due to the strong magnetic field. This could explain why the majority of the CVs observed in the hard X-ray band are IPs, in which cyclotron emission is negligible (Chanmugam et al. 1991; Burwitz 1997; Koenig et al. 2006; de Martino et al. 2006b; and reference therein). However, IPs are found to be dominant X-ray source population detected near the Galactic center by *Chandra* observatory. These systems also significantly contribute to the Galactic ridge X-ray emission. Moreover, most of the known CVs detected by *INTEGRAL* and *Swift* satellites are IPs (Revnivtsev et al. 2006; Ruiter et al. 2006; Bird et al. 2007; Suleimanov et al. 2008).

In general, CVs evolve through the period gap to minimum in P_{orb}, due to angular momentum loses by magnetic braking and gravitational radiation, on a time scale of $10^8 - 10^9$ yr. It has been suggested that as mCVs evolve towards shorter period, the magnetic field of the WD may be able to resurface and the magnetosphere fills more and more of the binary. Once the orbital period separation has shrunk enough to be comparable to the magneto-spheric radius, the interlocking fields of two stars could overcome the accretion torques, and this could allow the system to synchronize. If the magnetic field of the IPs high enough, they will synchronize in their evolution-

path towards short orbital periods, and hence they might become polars (Hellier 2001; Norton et al. 2004c, 2008; Scaringi et al. 2010).

It has long been suggested that IPs could be the evolutionary progenitors of polars (Chanmugam & Ray 1984). Some of IPs possess soft X-ray emission component and also show circularly polarized optical light similar to the observed in polars (like PQGem, UU Col and V405 Aur). Their similarity to low field polars led to the suggestion that some of these IPs (also called 'soft IPs') could be their true progenitors (Haberl & Motch 1995; Burwitz et al. 1996; Staude et al. 2003; Norton et al. 2004c; Evans & Hellier 2007). This idea has not been widely accepted, mainly because there are a lack of polarized emission and magnetic field strengths from IPs compared (in magnitude and size) to the polars (Katajainen et al. 2010; Potter et al. 2012).

In mCVs, the accretion flow can be characterized with four different scenarios. These are: '**propellers**' in which the rapidly rotating WD magnetosphere expels most of the transferred material away from the system (IP AE Aqr), '**disk**' in which the accreted material forms a disk around the white dwarf, truncated at its inner edge by the magnetic field of WD (IPs), '**streams**' in which accreted material is forced to follow the field lines on to the WD surface (polar, IPs), and '**rings**' in which the accreted material forms a ring around the WD (IPs) at the outer edge of its Roche lobe (Hellier 2007; Norton et al. 2008).

3. BRIEF OVERVIEW AND METHOD

3.1. OPTIMA (OPtical TIMing Analyzer) Instrument

This part describes the OPTIMA instrument with its data acquisition software. Firstly, an overview of the system will be given, and then its components will be described in detail.

3.1.1. High Speed Photo-Polarimeter OPTIMA

Pulsars, accreting stellar and galactic black-holes, neutron star or white dwarf binaries, and gamma ray bursts (GRB) are defined as cosmic high-energy sources. They typically show excessively fast temporal variation in their emissions throughout the spectrum. Optical radiation from these basically high-energy photon sources is frequently related to the non-thermal particle populations that produce the X- and γ-rays. In most cases, optical photons carry unique spectral, timing and polarization information about their source and can be measured with different ground based as well as on-board telescopes (Kanbach et al. 2003).

The high-speed photo-polarimeter OPTIMA, an active experimental instrument has been in design and development since 1996 by the gamma-ray astronomy group of the Max-Planck-Institut für extraterrestrische Physik (MPE), Munich Germany. This sensitive, portable detector is used to observe pulsars and other highly variable astrophysical sources with a specially sensitive timing accuracy in the optical band. The system presently contains 12 fiber-fed single photon counters using, so called, the avalanche photo-diodes (APDs) for photometry and polarimetry together with a global positioning system (GPS) for the precision timing control and an integrating charge-coupled device (CCD) camera for target acquisition, guiding, and atmospheric monitoring. The system is controlled and run by a data acquisition (DAQ) PC, for fast changes in observation modes, between photometry and polarimetry. A new configuration called 'OPTIMA-Burst' is now added and it features a control software that

allows a semi-robotic response to GRB triggers. Triggers move the telescope automatically to the source when it receive a burst signal from Swift BAT (the Burst Alert Telescope). The fiber array is configured as a hexagonal bundle for photometry and a tetragonal one for polarimetry. A separate fiber is located $\sim 1'$ away as a night sky background monitor. Single photons are recorded in all channels with absolute timing accuracy of ~ 4 μs. A new DAQ system (not yet installed for the measurements described in this thesis) will allow $\sim$10 ns resolution. The quantum efficiency (QE) of APDs has a maximum of 60% at 750 nm and above 20% in the range $450-950$ nm. Compared to similar photometers based on photomultiplier tubes (PMTs), OPTIMA has a $\sim$6 times higher sensitivity due to its large bandwidth and high QE. A rotating polarization filter or a newly developed 4-channel double Wollaston system for polarimetry, and a 4-color prism spectrograph for coarse spectroscopy have been used as optional equipment in the system.

OPTIMA has been tested and used on different telescopes since January 1999 to measure detailed light curve and polarization of the Crab Pulsar, search for the optical emission from the Gemini pulsar, and also for timing of cataclysmic variables stars and X-ray transients (Kanbach et al. 2003, 2008).

3.1.2. Instrument Overview

The main science goal of OPTIMA was to detect and measure the optical light curves of extremely faint (V $\sim 25^m$) young high-energy pulsars known to emit X- and γ-ray photons. To measure the light from compact binary systems with rapid brightness variations was the secondary goal. From such objects are expected to observe quasi-periodic as well as irregular and random density fluctuations. These features call for the detection and timing of single photons in order to obtain light curves with any convenient binning after the observations. Furthermore, the correlation of OPTIMA data with measurements from other ground or space observatories requires the recording of absolute arrival time of individual photons (Kanbach et al. 2003).

The OPTIMA photometer was in development since 1998 (Straubmeier et al.

2001) and was used progressively with more complete versions on the 1.3 m (Mt. Skinakas, Crete, Greece), 3.5 m (Calar Alto, Spain) and 2.1 m (Guillermo Haro, Cananea, Mexico) telescopes, and in the southern hemisphere on the 1.88 m (Mt. Stromlo, Australia), 2.2 m (ESO/La Silla, Chile) and 1.9 m (SAAO/Sutherland, South Africa) telescopes.

The description of the OPTIMA-Burst instrument in the following is based on the presentation by Kanbach et al. (2003) with some modifications and updates.

3.1.3. General Layout

As specified above, the initial science goals of OPTIMA were to obtain the optical light curves of selected pulsars and highly variable binary systems and also, to determine timing relations of them in other wavelength ranges (basically radio and X-rays). For this aim, accurate quantitative photometry is not of prime importance and fixed apertures of an appropriate size are usually sufficient. The apertures are given by optical fibers which are placed in the focal plane of a telescope and fed the light of target stars and sky background to APD detectors. To ameliorate the negative aspects of fixed aperture photometry, a small 'integral field unit' of apertures is installed in the form of a hexagonal close-packed bundle of fibers and a fast read-out for the field viewing acquisition CCD camera. The schematics of the new configuration of the OPTIMA detector (called 'OPTIMA-Burst' since 2006) and a photograph of the system are shown in Figure 3.1. and Figure 3.2. This configuration uses basically the components of the previous mode of experiment, but now, it has a separate box for the APD detectors (for the old version of OPTIMA see Kanbach et al. (2003)). The focal plane fiber pick-ups of the earlier version are kept in OPTIMA-Burst, however, there is an additional aperture that inputs light into a new double-Wollaston polarimeter. All fibers ($\sim$2 m length) are fed through a semi-rigid tube to the APD box.

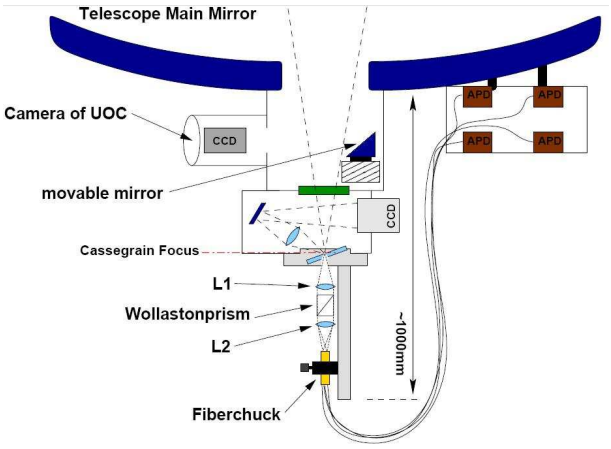

Figure 3.1. Schematic layout of OPTIMA-Burst configuration since 2006. The light from the telescope falls on a slant mirror with an embedded bundle of optical fibers in the focal plane and the light continues through the fibers to the APDs. The field around the fibers, visible in the mirror, is imaged with a CCD camera. [Adapted from Muhlegger (2006)]

3.1.3.1. Fibre Pick-Up and Detectors

OPTIMA intercepts the image formed in the focal plane of a large telescope with a slanted mirror. The reflected light is re-imaged on a commercial CCD camera. Currently, a fast-readout Apogee AP6 camera featuring a Kodak chip (KAF1000E, 1024x1024 pixels of 24.4 μm size, backside illuminated) is used in OPTIMA. A full frame is downloaded in $\sim$1 s. Embedded in the slanted mirror and coincident with the focal plane are the 'photon-counting' apertures (numbers from 1 to 4 in Figure 3.3.) and 2 small LED (Light Emitting Diode) light sources (labeled A and B in the same figure). These LEDs can be switched on, via a computer command and serve to control the overall alignment of the field-viewing optics and the camera. Aperture no. 1 (size $\sim$345 μm) in Figure 3.3. is the diaphragm for the double-Wollaston polarimeter which includes four fibers. Opening no. 2, with 1.7 mm diameter, contains the hexagonal fiber bundle (input: single fiber diameter $\sim$320 μm; output diameter: $\sim$100 μm; length: 2 m; illuminated from output side) mounted in a fine steel tube. The apertures no. 3 and 4 contain a fiber input to a $4-$channel prism spectrograph and a fiber to record the night sky background) near to the target, respectively. The field-

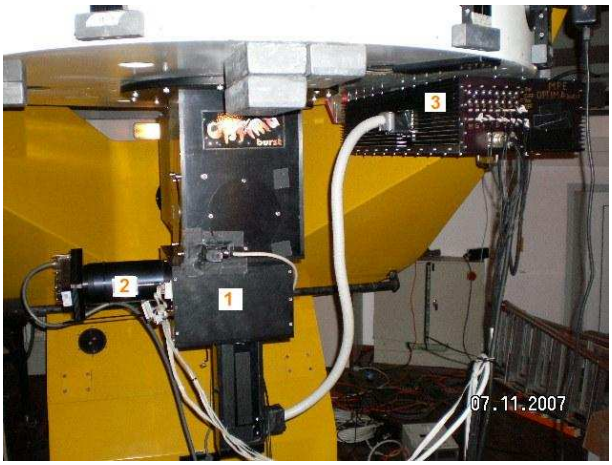

Figure 3.2. A photograph of OPTIMA-Burst mounted on the 1.3 m Cassegrain focus telescope of the Skinakas Observatory. The target acquisition optics (filters, target imaging and fiber pick-up) is located in box no. 1 and the CCD camera is mounted externally box no. 2. APD photon counters are located in box no. 3 connected to the telescope

viewing optics shows a region of approximately $12' \times 12'$ at the 1.3 m telescope (with f-ratio=7.64), at Skinakas Observatory. The telescope mirror has with some vignetting near the edges. The main task of this system is to acquire the target star and to derive the telescope control commands to move the target into any chosen aperture. During the photon counting measurements, when the telescope guiding is controlled by an external auto-guider, the secondary task of the OPTIMA CCD is to take serial images of the field with short integration times (typically 10 s). These images is evaluated for the atmospheric seeing and transparency conditions during the measurement.

3.1.3.2. Timing, Data Acquisition, and Software

The signals provided by the system GPS supply a global absolute time base. This system uses a receiver which can process the clock pulses of up to six satellites simultaneously and reach an absolute time accuracy of better than 2 μs on the 'pulse per second' GPS signal. This signal disciplines a local high frequency oscillator (250 kHz, i.e. leading to a time resolution window of 4.2 μs) with the same precision providing a continuous Coordinated Universal Time (UTC) signal to the system bus

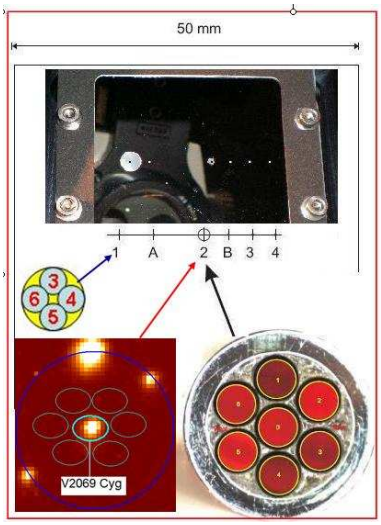

Figure 3.3. Schematic layout of the fiber input apertures in the field-viewing mirror (no.1: polarimeter diaphragm with a size of $\sim$ 345 μm, no.2: photometry hexagonal fibers array with a size $\sim$1.7 mm, no.3: the spectrometer diaphragm, no.4: sky background monitor fiber) and photograph of the hexagonal fiber bundle (central fiber for the target, ring fibers for the close-by sky or nebular environment). [Adapted from Kanbach et al. (2008)]

of the PC used for DAQ. The task of the DAQ unit is thus to correlate the electronic signals of the APD detector modules with the high resolution time base and assign UTC arrival times to each detected photon. The timing of the conversion cycles of the DAQ card is controlled by the GPS based oscillator, so that the transfer of the APD detector signals is running at a fixed rate. The absolute starting time of each software triggered acquisition sequence is precisely known. The controlling software counts the number of conversion cycles since the start of the sequence and stores this sequential number together with an identifier of the respective detector channel for each detected photon. Conversion cycles without detected photons are skipped. Based on the cycle number, the acquisition frequency and the absolute time of the start of the sequence the UTC arrival time of every recorded photon can be restored during data analysis. During the long-term measurements the consistency and continuity of the time base are continuously controlled.

The presently used DAQ system is limited to rates below about $\sim 10^5$ counts/sec because of pile-up in the time-resolution window. Future versions of the DAQ should

be able to control higher rates, which are achievable with the photon counters (up to several MHz). Typical count rates from the night sky in dark conditions are $\sim 1-2$ kHz per fiber resulting in several GBytes of data for a night of observing. Data are first staged to RAM and periodically (about every 10 min) stored on hard disk drive (HDD). During the data analysis the topocentric photon arrival times can be converted to the solar system barycenter.

3.1.3.3. The Photometer

For the observation of faint sources, it is very important to convert the highest possible fraction of incoming photons into countable signals, i.e. to have detectors with high QE over a wide spectral band. Most previous systems for recording single optical photons with time resolutions of a few μs used PMTs or detectors based on a similar technology. Their photo cathodes usually had a peak QE of typically 20% and a narrow wavelength range of sensitivity. Much better QEs can be reached with the present-day solid state detectors. These silicon devices have peak QEs of up to 80% and a wide band of sensitivity ranging from 250 to 1100 nm. OPTIMA uses commercially available APD-based single-photon counting modules (type SPCM-AQR-15-FC by Perkin-Elmer). These highly integrated devices operate in a Geiger counter mode where a photon initiated avalanche pulse is quenched by the instantaneous reduction of the bias voltage. The diodes have a diameter of 200 μm and are electrically cooled with Peletier elements. The selected units offer low dark count rates of typically $\sim$100 counts/sec, and are insensitive to electromagnetic interference and very reliable. They can record photons up to rates of $\sim 2\times 10^6$ counts/sec before noticeable dead-time losses occur. The present DAQ however can not keep up with such rates. Typical DAQ event losses around 1% are encountered for rates of 4×10^4 counts/sec. The achieved QE of the APD detectors is shown in Figure 3.4. Although it falls short of the values mentioned above, it is still above 20% for a spectral range from 450 to 950 nm. Bandwidth and QE of APDs results in about a factor of 6 improvement in sensitivity, compared to PMT based systems.

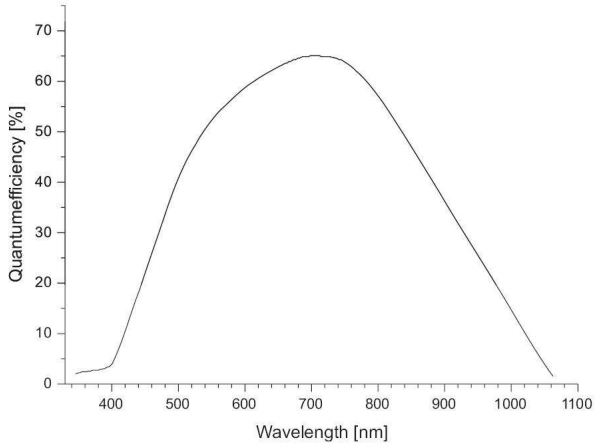

Figure 3.4. Typical quantum efficiency of the Perkin-Elmer APD single photon counting modules SPCM-AQR-15-FC; dark noise ranging from 100 to 250 counts/sec. [Taken from Kanbach et al. (2008)]

3.1.3.4. The Polarimeter (Double Wollaston System)

The Double Wollaston configuration (Figure 3.5.), which is available for OPTIMA, provides the irregular transient source to be measured with a system that offers parallel simultaneous polarimeters. The target star is positioned in a diaphragm (aperture of $\sim$345 μm in the field viewing mirror) and the emerging beam is collimated. Two quartz Wollaston prisms are positioned side by side in the collimated beam (separated by a thin opaque plate), so that about half of the beam falls on each prism. The polarized and symmetrically diverging output beams (divergence about 1°) are refocused onto a fiber pick-up where four regular tapered fibers are mounted in a chuck. For further detail refer to the work of Muhlegger (2006) and Duscha (2007). The system has been verified in the MPE laboratory with polarized and unpolarized light and used on the Skinakas observatory since November 2005 campaigns.

OPTIMA can be operated in two different modes using the fibers: the photometer mode and polarimeter mode. In the photometer mode the hexagonal fiber bundle is used together with the background fiber, therefore, only eight channels can recorded by the DAQ at the same time. In this mode the hexagonal configuration of the fiber bundle allows observation of the source and its surrounding background, simultaneously.

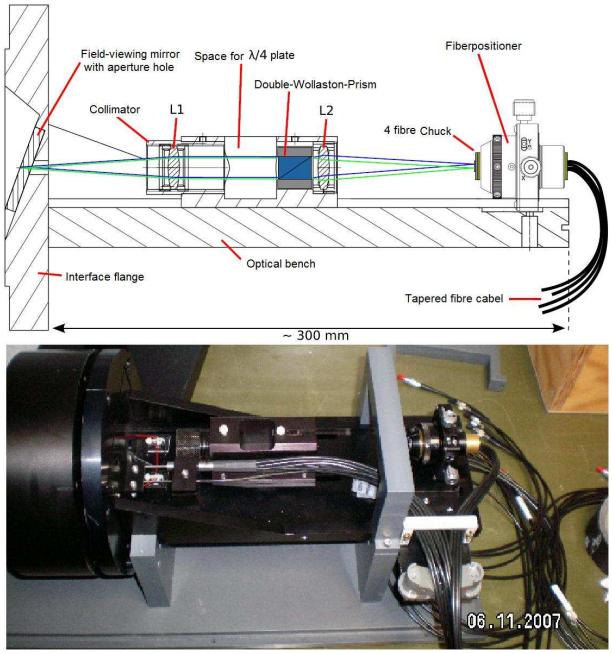

Figure 3.5. Cut through the Double Wollaston Polarimeter. In the central parallel beam two quartz Wollaston prisms, each covering about half the beam and separated by a thin opaque plate, split the incoming light into four images that are polarized at staggered angles and arranged approximately on the corners of a square. [Adopted from Muhlegger (2006)]

On the other hand, in the polarimeter mode, the channels 3, 4, 5 and 6 are dedicated to the Wollaston output, while the rest (three fiber of the bundle fibers and the background fiber) are connected to photometer. In this mode the polarimetric observation can be performed with the parallel Wollaston polarimeter through this four Wollaston channels, corresponding to polarization angles of 0°, 45°, 90° and 135° in case of OPTIMA's Wollaston prism, and the rest three fiber of the fiber bundle and the background fiber can be used to determine the background intensity during the observation, simultaneously.

3.2. Calibration and Reference Measurements of OPTIMA

This part describes calibration and polarization measurement of OPTIMA data obtained at the Skinakas Observatory (Jun−July 2008-2009-2010, Crete, Greece).

3.2.1. Pile Up Effect (Correction)

In OPTIMA observations of bright sources, the arrival of two or more photons to DAQ at the same time (before their read out) may give rise to a pile-up effect. The OPTIMA DAQ system records only one-photon event within one read-out time interval ($\tau \sim 4\ \mu$s), even if two or more photons arrive to a APD. At very high counts rates the pile-up effect is a real problem and it becomes non-ignorable. Therefore, the missed events counting should be improved statistically after data binning. An analytical formula for correcting the pile-up both in count-rate as well in the error of the count-rate has been derived by Stefanescu (2011). For OPTIMA data reduction, the pile-up correction formula can be briefly summarized as below, (for detailed derivation see Stefanescu (2011)).

$$R(r) = -\tfrac{1}{\tau} ln(1-\tau.r) \qquad \sigma_R = \sqrt{\tfrac{r}{\Delta t} \cdot \tfrac{1}{(1-\tau r)}} \tag{3.1}$$

Corrected rate R for measured rate r Uncertainty σ_R of corrected rate R

Here, τ is the DAQ read-out time interval, Δt is the binning time used during analysis.

3.2.2. AROLIS Measurements

Before each observation campaign, the AROLIS (**AR**tificial **O**PTIMA **LI**ght **S**ource) measurements were carried out to measure the relative sensitivity of each channel (fiber) and to calibrate them according to each other. This process consists of several steps. In so called AROLIS measurements, the detector unit of OPTIMA is illuminated with two LEDs mounted at the front of OPTIMA photo-polarimeter. One of these LEDs is an unpolarized bright (white) light source used to adjust the Polarimeter fiber chuck and the other is a faint (green) light source with a diffuser for testing the Photometer and hexagonal fiber bundle (Figure 3.3.). During the measurements, LEDs are driven by an adjustable power supply where the voltage is increasing step by step.

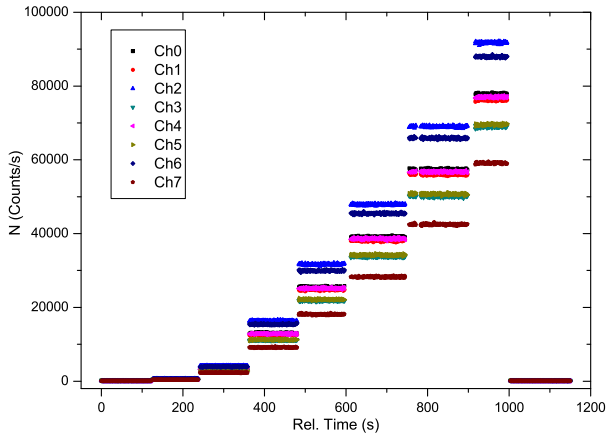

Figure 3.6. AROLIS photometer raw data (03 Jun 2009 Skinakas observatory)

During these measurements to determine the instrumental dark count rates of APDs, the OPTIMA shutter is kept closed in the first and last two or three minutes. The APD dark count rates correspond to the dark frames in the CCD data reduction sample. The resulting APD count rates in all channels are recorded by the OPTIMA-DAQ system.

3.2.2.1. AROLIS-Photometer Measurement

The most often used observation mode with OPTIMA is the photometer mode. In this mode, the light from telescope is incident on a slant mirror with embedded optical fibers in the focal plane and the photons of each fiber are registered by the APDs. The fiber bundle (with the background fiber) allows observation of the source and its surrounding background are recorded by the OPTIMA-DAQ system simultaneously. The counting output of each fiber channel must be calibrated since transmission efficiencies and APD detectors may have different responses. This is performed by measuring a diffuse light source and calibrating it against one of the fibers as a reference. Therefore, the main component of this work is to measure the relative sensitivity of each channel and to calibrate them according to each other. This measurement is done by using the AROLIS photometer raw data as given in Figure 3.6.

In the measurement, first step, the corresponding instrumental dark (APD-dark) rates are subtracted from each photometer channel. The dark rate of APDs can be

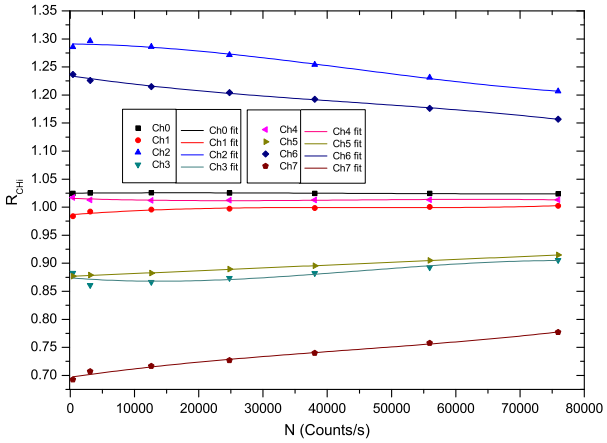

Figure 3.7. The dependence of the relative sensitivity versus total count rate fitted by a cubic polynomial of each channel for the AROLIS Photometer data, 03 Jun 2009, Skinakas Observatory

accepted as a constant, because they should have equal values before and after the measurements in the framework of the observatory or MPE laboratory. The dark rates are determined by averaging the first and final level of the background measurements for each channel, separately. The error between these two levels results from a Poisson distribution. The relative sensitivity of each channel R_i with respect to the average rate of all channels can then be calculated by using the following equation (Stefanescu 2004; Muhlegger 2006),

$$R_i = 8\frac{\overline{N}_i}{\sum_{j=0}^{7}\overline{N}_j} \tag{3.2}$$

Here, i and j are channels number (0,1,...7). The dependence of the R_i versus the total average count rate N_i can be fitted with cubic polynomial and extrapolated for higher count rates (Figure 3.7.) to obtain the calibration factors used in the calibration process:

$$r_i = A + B.\overline{N}_i + C.\overline{N}_i^2 + D.\overline{N}_i^3 \tag{3.3}$$

Finally, the r_i values of each channel can be obtained in the range of N=0 to N=8000

Table 3.1. Fit parameters obtained from the cubic polynomial fitting and extrapolation of the relative sensitivities of individual channels to the total intensity in the range N=0 to N=8000 s^{-1} by the AROLIS Photometer calculations on 03 Jun 2009 at Skinakas Observatory

Channel	A	B $(10^{-7}s)$	C $(10^{-11}s^2)$	D $(10^{-16}s^3)$
Ch0	1.025	0.805	-0.296	0.224
Ch1	0.987	8.909	-2.011	1.475
Ch2	1.291	-1.129	-3.042	2.280
Ch3	0.874	-9.422	4.046	-2.991
Ch4	1.016	-3.865	1.091	-0.8.29
Ch5	0.877	4.755	0.077	-0.062
Ch6	1.234	-16.76	2.044	-1.556
Ch7	0.697	16.71	-1.909	1.458

s^{-1}. These fit parameters obtained for the campaigns in Jun-July 2009 at Skinakas observatory are shown in Table 3.1.

On the other hand, instead of using AROLIS measurements, the fiber calibration process can be carried out according to each other by using sky dark measurements which obtained from all fibers for few minutes before and after the target observations under the supposition that the sky background is uniform, and free of sources in a deep CCD exposure over a region with radius of 0.5 arc-min which appears. To determine each fiber's calibration factor, the average of the sky dark measurement of each fiber is divided by the average of the sky dark measurement of all fibers separately as in Equation 3.2 After that the count rates in each channel are divided by these factors respectively. This calibration corresponds to flat fielding with a sky-flat in a CCD data reduction sample.

3.2.2.2. AROLIS-Polarimeter Measurement

In the new configuration, the polarimetric observations of the astronomical objects are obtained by using polarimeter mode of OPTIMA detector. In this mode, to get a cleanly reduced polarization data, we need also to calibrate the fibers, and get the background data (APD dark and sky background) and deduct this from each channel. Here, for the calibration process, we follow similar procedures for the photometer

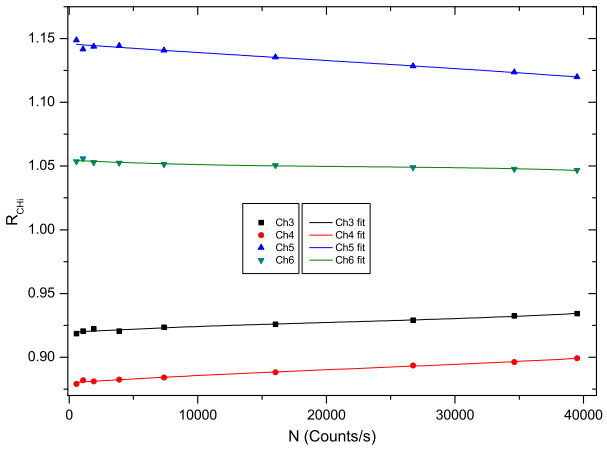

Figure 3.8. The dependence of the relative sensitivity versus total count rate fitted by a cubic polynomial of each channel for the AROLIS Polarimeter data, 03 Jun 2009 Skinakas Observatory

data. After subtracting the corresponding instrumental (APD) dark rates from each polarimeter channel, the relative sensitivity R_i of each channel can be calculated by using the following formula,

$$R_i = 4\frac{\overline{N}_i}{\sum_{j=3}^{6}\overline{N}_j} \tag{3.4}$$

Here, i and j are channel numbers (3,4, 5 and 6). A the third-degree polynomial fit is presented in Figure 3.8. to obtain the calibration factors r_i which are used in the calibration process:

$$r_i = A + B.\overline{N}_i + C.\overline{N}_i^2 + D.\overline{N}_i^3 \tag{3.5}$$

The corresponding fit parameters obtained for the campaigns in Jun-July 2009 at Skinakas observatory are summarized in Table 3.2. Finally, the count rates in each channel can be divided by these r_i factors to calibrate the fibers, respectively.

Table 3.2. Fit parameters obtained from the cubic polynomial fitting and extrapolation of the relative sensitivities of individual channels to the total intensity in the range N=0 to N=8000 s^{-1} (AROLIS Polarimeter, 03 Jun 2009, Skinakas Observatory)

Channel	A	B $(10^{-7}s)$	C $(10^{-11}s^2)$	D $(10^{-16}s^3)$
Ch3	0.91952	5.716	-1.357	2.181
Ch4	0.87993	6.619	-1.046	1.518
Ch5	1.14589	-7.252	0.544	-0.946
Ch6	1.05466	-5.084	1.859	-2.753

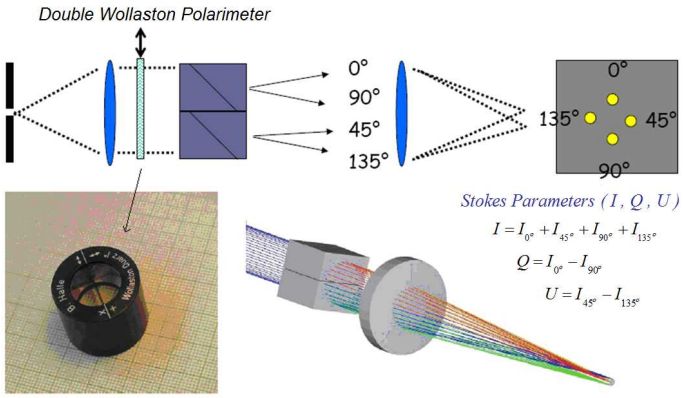

Figure 3.9. Schematic configuration with related figures for Wollaston polarimeter

3.2.3. Mathematical Process for Polarimetry

The polarization measurements are performed using a parallel Wollaston polarimeter (Figure 3.9.), based on birefringent crystals to allow measurement of the full set of linear Stokes parameters in each time bin. The incoming light beam encounters the two halves of the parallel Wollaston prism and passing through them. Then, the light exits from the parallel Wollaston prism in four different directions corresponding to the polarization angles (0°, 45°, 90° and 135°). In this case, the individual brightness measurements allow the mathematical reconstruction of the polarization angle and degree of polarization of the incident light beam (Muhlegger 2006).

Henceforth, we will present a step by step polarization data analysis by using the methodology described by Sparks & Axon (1999). The parallel Wollaston prism inside the OPTIMA instrument provides polarimetric data that include a series of 'im-

ages' of an object taken through 4 sets of linear polarizers as in Figure 3.9.

Measurement of at least three distinct polarization quantities are required in order to characterize entirely the linearly polarized light. The most common of them involves the total intensity of the light I, the degree of polarization p and the position angle θ. An 'intermediate' stage between the input data and the solution of polarization quantities are the Stokes parameters (I, Q, U) that are related through:

$$\begin{pmatrix} I \\ Q \\ U \end{pmatrix} = \begin{pmatrix} {I_0}^\circ + {I_{45}}^\circ + {I_{90}}^\circ + {I_{135}}^\circ \\ {I_0}^\circ - {I_{90}}^\circ \\ {I_{45}}^\circ - {I_{135}}^\circ \end{pmatrix} = \begin{pmatrix} I \\ Icos(2\theta)p \\ Isin(2\theta)p \end{pmatrix} \tag{3.6}$$

another way to express the physical quantities that are obtained from the Stokes parameters by transforming the above equation are:

$$\begin{aligned} p &= \frac{\sqrt{Q^2+U^2}}{I}, \\ \theta &= \frac{1}{2} arctan \frac{U}{Q} \end{aligned} \tag{3.7}$$

These quantities describe all the essential properties of linearly polarized radiation from a source. From an input data set of 4 polarized intensities I (measured in counts by the Wollaston Polarimeter) and their errors ($\sigma_I = \sqrt{I}$), assumed independent between observations, corresponding to a set of observations through these 4 polarizers, the Stokes parameters can be derived following the case of n polarizers after Sparks & Axon (1999) as described in APPENDIX.

3.2.4. Calibration of the Polarimeter in the Laboratory

In the polarimeter mode, the calibration of the exact position angle (ϕ_k) of the four Wollaston output channels (see Section 3.2.2.2) can be made by illumina-

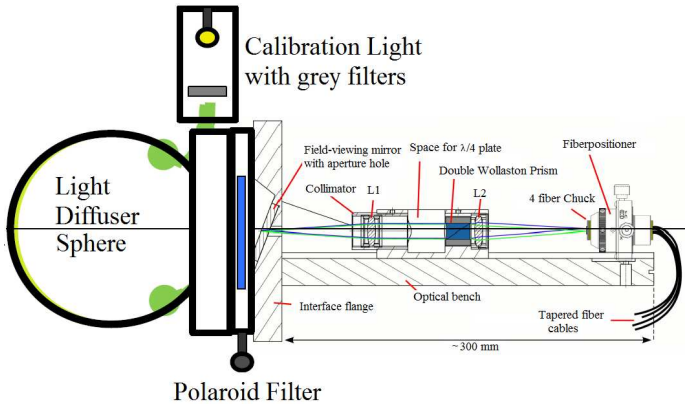

(a)

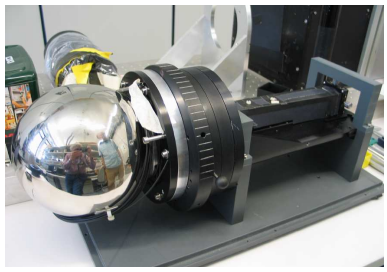

(b)

Figure 3.10. Schematic figure of the rotatable Polaroid filter and light diffuser sphere mounted on the Double Wollaston Polarimeter

tion through a rotatable Polaroid filter. The rotatable Polaroid filter (Figure 3.10.) is mounted between the light diffuser sphere and the polarimeter, which is connected to the aperture hole (field-viewing). The light diffuser sphere is illuminated by a lamp with a F1 grey filter and a broad-band filter transmitting 400-710 nm. The rotatable Polaroid filter has a manually adjustable angle, scaled from 0 to 180 degrees.

The polarimeter test measurements were performed in the laboratory at MPE (also can be done at the observatory, when OPTIMA is mounted on the telescope). Firstly, the Polaroid-angle scale was set to zero as the reference angle, and the resulting count rates in four channels were recorded for 5 minutes with the OPTIMA-DAQ. Then, the Polaroid-angle scale was set to different 36 angles from 0 to 180 (with an increase of 5 degrees) to record 5 minutes data. To determine the instrumental dark count rates of each APDs, before and after these measurements the light is kept closed

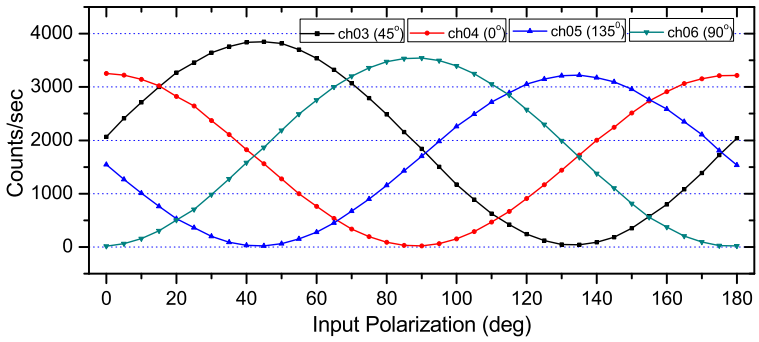

Figure 3.11. Count rate curves of the four polarimeter channels during Polaroid circulation. Here *Ch*3, *Ch*4, *Ch*5 and *Ch*6 represent position angle of 0°, 45°, 90° and 135° respectively

for two-three minutes during data recording. The data analysis of this measurements were done with a simple method as described in the following.

In the first step, the average count rate of each measurements (for 36 angles measurement) for each channel were determined by averaging each 5 minutes data set. After that the corresponding APD dark rates were subtracted from averaged 36 data sets of each channel. Figure 3.11. shows the curve of the averaged count rates of the 36 measurements for four channels. It is clearly seen that the averaged count rates of the individual channels are different. To determine the exact position angles of the four output channels of the polarizer, these four curves can be fitted with parametric sine function, separately.

$$y = a + b * sin(c * x + d) \tag{3.8}$$

where, b and $T = 2\pi/c$ are the amplitude and the period of the function, d/c represents the phase shift of the sine waves, which can be transformed in to an angle as follows,

$$\alpha = (d/c) * (360/2\pi) \tag{3.9}$$

The fit results with their uncertainties obtained from the parametric sine function fitting are listed in Table 3.3. The measured position angles of the four output

Table 3.3. Measured position angles of four output channels of the polarizer

Channel	Ideal Angle	Measured Angle, ϕ_k	Uncertainty, σ_k
Ch3	45°	43.08°	0.078
Ch4	0°	-1.05°	0.300
Ch5	135°	133.50°	0.035
Ch6	90°	88.40°	0.054

channel of the Wollaston polarimeter show significant deviations from the ideal values. This, may be caused by the wrong positioning of the fibers during the adjustment. A difference in the alignment of the two Wollaston prisms could be explained by possible defects during the manufacturing process of the double Wollaston prism.

After determining the throughput coefficients for each individual polarimeter channel by using unpolarized light (as explained in Section 3.2.2.2), and the exact position angle of the four Wollaston polarimeters (listed in Table 3.3.), the Stokes parameters can be calculated by as given in Section 3.2.3. Here we accept the efficiency of the polarizers as 1, assuming that the four polarizers as perfect polarizer ($\varepsilon_1 = \varepsilon_2 = \varepsilon_3 = \varepsilon_4 = 1$). The Stokes parameters can be transformed to physical quantities: polarization angles and degree of polarization by using Equation (3.7). The polarization angle offsets can be calculated by subtracting the measured polarization angles from the reference polarization angles (Figure 3.12.). The measured angles are in good agreement with expected, even if the systematic errors are considered. For example the manual adjustment of the filter might have resulted in some offsets from the nominal angles. The measured degree of polarization during the Polaroid circulation is represented in Figure 3.13. Response to $\sim$100% polarized light (illumination through a Polaroid filter) the variability of the degree of polarization obtained from the measurement can be explained by scattered light in the laboratory.

3.2.5. Calibration of the Polarimeter on Celestial Sources

In this part, the polarization of astronomical signals will be discussed. Most of a star's light is unpolarized. The low polarization in stars is due to their spherical sym-

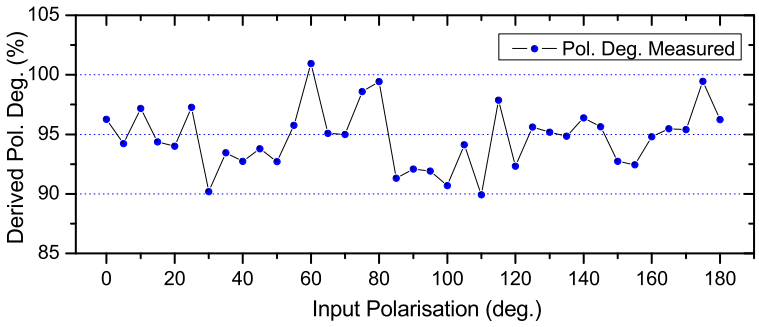

Figure 3.12. Response to ∼100% polarized light (illumination through a Polaroid filter). Stray room light could affect the degree of polarization reconstruction

metry and that they are at a great distance: if there is any linear polarization it might be averaged out over the star's visible disk. When the intrinsic linear polarization occurs at a stellar object (e.g. by scattering in a photosphere), the direction of polarization due to the spherical symmetry is positioned rotationally symmetric. Since a star (with the exception of the Sun) can not be simultaneously resolved spatially and spectrally by an observational instrument, its measured total polarization will be approximately close to zero. There are two conditions to follow an object appearing polarized at some level. First, there must be an intrinsic effect which produces polarized light, or polarizes the starlight. Second, there must be appreciable asymmetry in the astronomical situation, so that the polarization will not disappear due to spatial averaging out over the object (Tinbergen 1996). Polarized light can be either issued directly from a lamp (such as produced by synchrotron radiation), or by modification of unpolarized light (by scattering, reflection or transmission through a polarizing medium). To implement the measurement for the polarimeter the following steps were carried out.

In order to calibrate the angular orientation of the polarimeter we calculate the polarization angle by measuring the Rayleigh-scattered sunlight during twilight and compare it with expected one. This calculation is used to confirm the validity of the measured angle. We also chose some standard reference stars (for example, the unpolarized standard star BD+28° 4211 and the polarized standard star BD+64° 106) to test and calibrate the polarization unit of OPTIMA on the telescope.

In addition to the actual measurements, we need also the acquisition of the

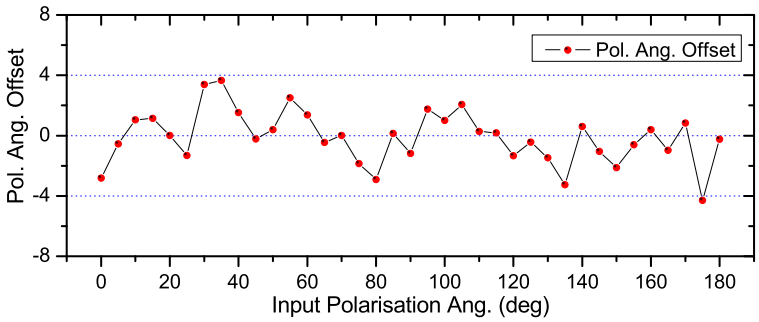

Figure 3.13. Response to ∼100% polarized light (illumination through a Polaroid filter). The manual adjustment of the filter might have resulted in some offsets from the nominal angles

background. Each of the avalanche photo-diodes has a dark count rate dependent on temperature. Although the APDs are controlled thermostatically, it could also indicate count rate changes. Therefore the APD dark rates should be recorded before and after each measurement. To deduct this expected effect, a constant value can be obtained by averaging APD dark counts from each channel. Even the sky background of the vicinity of the concerned object should be taken before and after each measurement. With a similar method, a constant value from sky background data can be determined by averaging sky background data from each channel after deducting APD dark values.

3.2.5.1. Calibration of the Angular Orientation of the Polarimeter

The calibration measurements were performed in the OPTIMA-Burst-campaign at the Skinakas Observatory (2008-2009). The polarimeter measures initially the angles only relative to the instrument's coordinate system not in any celestial reference system. Although the individual transmission directions of the polarizers of double-Wollaston-Polarimeter (which is mounted on the telescope) are oriented, the exact location of its zero-point-angle relative to the sky is not exactly known. For relative angle measurements, this zero-point is not meaningful. But if we want to measure absolute polarization angle (to compare measurements with the measurements from other instruments), the polarimeter must be calibrated. This can be done by measuring

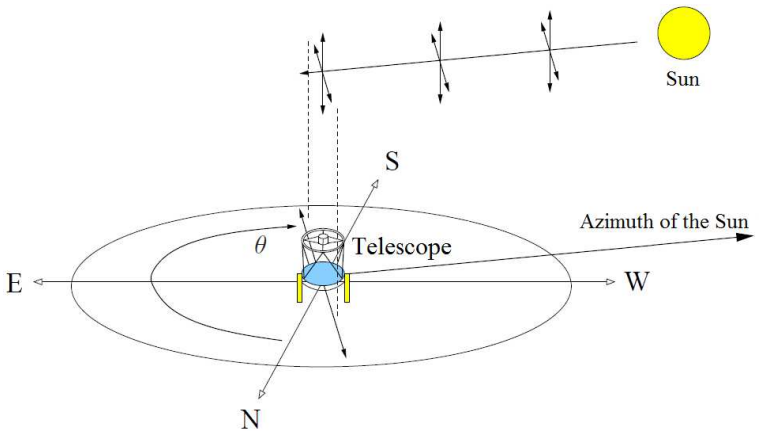

Figure 3.14. Calibration of the zero angle on the sky before sunrise (or after sunset). In this sketch, the Sun during measurement has to be below the horizon. Here θ is polarization angle measured by the observer (adapted from Muhlegger (2006))

the Rayleigh scattered sunlight during twilight (Muhlegger 2006). The direction of the polarization for the Rayleigh scattering case can be visualized in the following way.

When the sunlight passes through the Earth's atmosphere, it gets scattered by the electrons of the air molecules and it causes the electrons to vibrate perpendicular with respect to the direction of propagation of sunlight. The vibrating electrons, in turn, re-emit light with the vibration directions in the same plane. Since the light is a transverse wave, only the horizontally vibrating component propagates in the direction of the telescope. Therefore the measured light is polarized perpendicular to the azimuth of the sun (the direction of the incoming light). Because of multiple scattering by air molecules, the initially unpolarized light could be highly polarized with a quite large values of degree of polarization (nearly 80-100 percent) and at a scattering angle of 90 degree from the light source (Cronin et al. 2005; Kokhanovsky 2008).

The telescope was operated for this measurement at sunrise (or sunset) towards the zenith and tracked at a distance of 90° to the Sun. Figure 3.14. illustrates how polarized light is produced during twilight. Here θ is the polarization angle of the scattered light measured by the observer. The expected polarization angle θ' is described by the sum of the zenith angle (90°) and the azimuth angle of the Sun at the time of measurement (θ' = Azimuth + 90°). The Azimuth angle is defined as the zero

Table 3.4. Polarization measurement for the Rayleigh scattering (07.09.2008)

The azimuth of the Sun	θ' = Azimuth + 90°	Measured angle θ	Offset = θ-θ'
75.865	165.86°	174.68°	8.8°

angle of the polarization at the north direction and this angle increases from the north to the east (Muhlegger 2006).

The evaluation of this calculation was done with the data analysis described in the following simple method. The polarimeter count rates (sunlight data during twilight) were first normalized after subtracting the corresponding instrumental (APD) dark counts. And then, in order to calibrate the fibers, the count rates in each channel divided by the r_{Chi} factors (Equation (3.5)). After that, the Stokes Parameters and polarization angle θ (measured angle during twilight) are calculated using Equation (1.13) (see APPENDIX) and Equation (3.7), respectively, (see Section 3.2.3). The azimuth angle of the Sun at the time of the measurement can be determined using astronomy software *Skycal* or *XEphem3* tools. Table 3.4. shows the results of measurement for the Rayleigh scattering.

As it is shown in Table 3.4. the offset between the two angles is 8.8°. This value is determined by subtracting the average of the measured data from the average of expected data. Figure 3.15. shows the variation of the measured and the expected polarization angle for the observation which is done in the date of 07.09.2008. The fits are straight and approximate parallel for the measured and expected polarization angles. This results confirm the validity of the measured angle, and then can be used to confirm and calibrate the polarimeter.

3.2.5.2. Polarization of Standard Stars

The Unpolarized Star BD+28° 4211;

Instrumental polarization is the measured polarization of an instrument when an unpolarized source is observed. Unpolarized stars (taken from the catalog of calibration objects of Hubble Space Telescope, as given by Turnshek (1990)) can be used

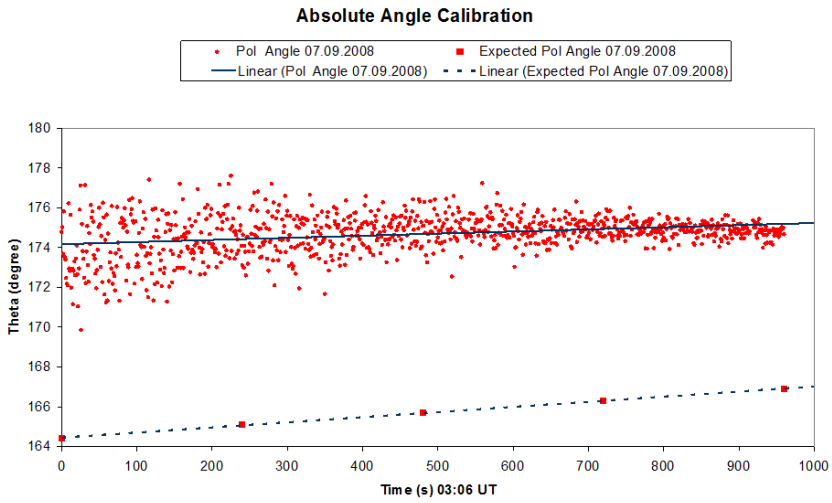

Figure 3.15. Measured and expected polarization angle at the sunrise in Skinakas observatory

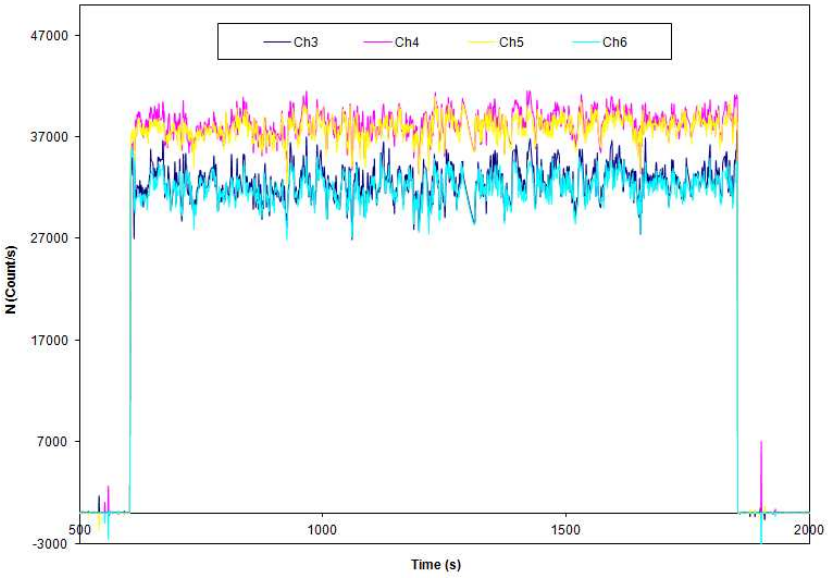

Figure 3.16. Exemplary light curve of the polarimetric standard star BD+28° 4211 after implementation of the complete calibration and standardization (10.09.2008)

to calibrate the polarization unit of OPTIMA instrument on the telescope. The degree of polarization of these stars are normally zero. A calculated non-zero polarization is caused by several effects: reflection losses at the surface of the lenses and the prism, absorption in the double Wollaston prism and lens, transmission coefficient of the fibers and efficiencies of the photon counters (Muhlegger 2006). These effects are smaller, when the aperture ratio f/D is larger (because, the light rays fall almost perpendicular on the mirror surface). The unpolarized white dwarf BD+28° 4211 was observed to perform this calibration to measure the magnitude of this instrumental effect.

Under the telescope mirror, the configuration of two halves of the double Wollaston polarimeter are different from each other. Because the halves are not identical, it leads to differences on the entering of total counts into the associated channels (fibers). Therefore, after deduction of the respective APD dark rate and sky background (partially polarized), and calibration of the channels with the relative sensitivities which are listed in Table 3.2. the requirement to balance the two halves of the Wollaston system can be done using the equation, $I_{Ch3} + I_{Ch4} = I_{Ch5} + I_{Ch6}$ for each time step of the standardized measurement. The polarization of the sky background must be assumed to be constant, since there is no available comparative polarimeter. Here, further verification is necessary to obtain the relative sensitivities of the channels on the telescope which can be different each day due to environmental influences. Figure 3.16. displays the light curves of each channels of measurement data on 10.09.2008.

Then, the Stokes Parameters are calculated (using Equation (1.13) in APPENDIX). In Figure 3.17. is shown the $Q/I - U/I$ diagram of the reference star BD+28° 4211 after full calibration. The Stokes parameters are transformed into physical quantities; the polarization angles and degree of polarization by using Equation (3.7). In line with the measurements shown in Figure 3.17. OPTIMA does not detect much polarization from this star. The polarization data of this unpolarized star from the catalog and OPTIMA measurement are listed in Table 3.5.

The Polarized Star BD+64° 106;

A star light can be polarized by the following effect: The interstellar medium contains dust particles with non-spherically symmetric structure. Therefore the effi-

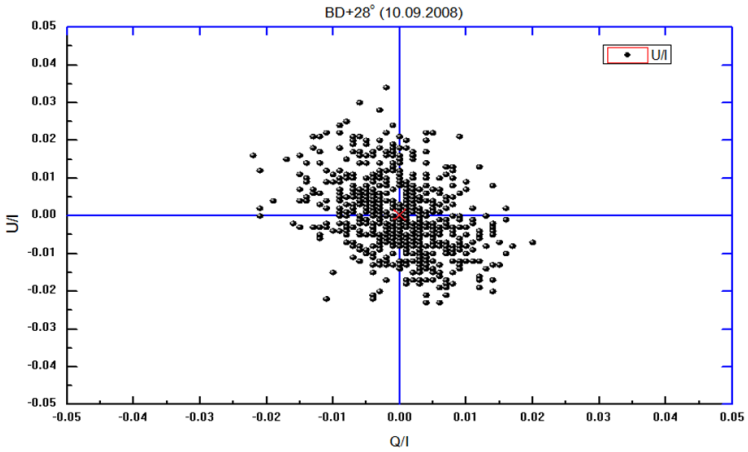

Figure 3.17. Stokes vector diagrams of polarimetric standard star BD+28° 4211 (I, Q and U are Stokes Parameters)

Table 3.5. Polarization measurement for polarimetric standard star BD+28° 4211

From Catalog (Turnshek 1990)	Degree of polarization	p = ∼0.063 ±0.027%
From OPTIMA	Degree of polarization	p = ∼0.49 ±0.28%
Magnitude	V∼10.5 mag	

ciency of the cross section of these structures for a scattering photon is dependent on its polarization direction. The dust particles will be oriented with the interstellar magnetic field along the field lines. Hence, photons with specific polarization directions will be scattered or absorbed more than others. In this way, unpolarized star light can be replaced by a net polarization similar to the effect of a Polaroid filter. The polarized standard star BD+64° 106 can be used to test and calibrate the polarimeter. The calibration data for this object was determined directly from the previous measurements.

To analyses the polarized star data, some basic calculations were performed analogous to the analysis of unpolarized star data. In order to have a better statistic, the standard star should be measured two or more times in a frame of an observation campaign. Each measurement of the unpolarized star should be done in the same night with the polarized star for a better calibration of OPTIMA. Figure 3.18. displayed the light curves of each channels of BD+64° 106 data that was measured on 06.09.2008. The Stokes Parameters (Q, U and I) can be calculated (using Equation (1.13). After

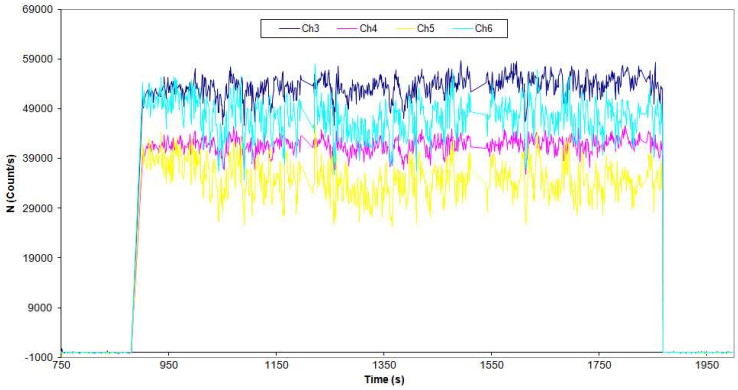

Figure 3.18. Exemplary light curve of the polarimetric standard star BD+64° 106 after implementation of the complete calibration and standardization (05.09.2008)

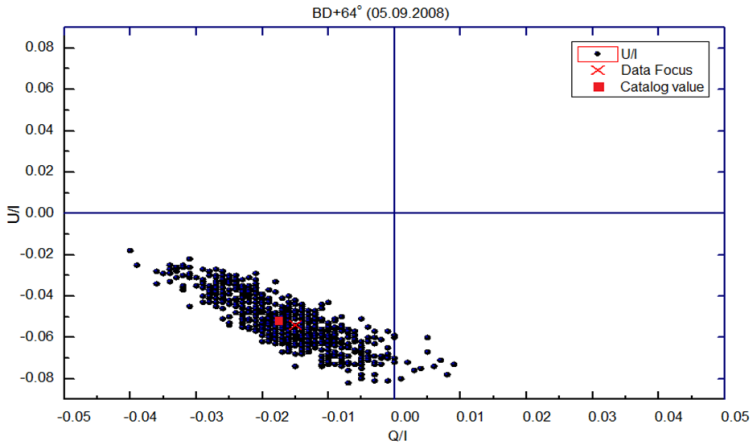

Figure 3.19. Stokes vector diagrams of polarimetric polarized standard star BD+64° 106 (I, Q and U are Stokes Parameters)

that the degree of polarization and polarization angle can be computed from Stokes Parameters using Equation (3.7). In Figure 3.19. is shown Q/I-U/I diagram of the reference star BD+64° 106 after full calibration. The polarization values from the catalog of HST and OPTIMA measurement are listed in Table 3.6.

The derived polarization degrees and errors are listed in Table 3.5. and Table 3.6. all agreeing with the catalogue values. The calculated polarization angle is a bit higher than the catalog value; however, both angles are compatible within the errors. These values are used to verify the functional capability of the polarization mode of OPTIMA. The small amount of the deviation between the calculated and catalog val-

Table 3.6. Polarization measurement for polarimetric unpolarized standard star BD+64° 106

From Catalog (Turnshek 1990)	Degree of polarization	p = ∼5.65 ±0.053%
	Polarization angle	θ = ∼96.8°
From OPTIMA	Degree of polarization	p = ∼5.73 ±0.8%
	Polarization angle	θ = ∼98.4 ±5°
Magnitude	V∼10.34 mag	

ues could result from the systematic factors such as clouds, seeing, moon position, etc. Here the errors were estimated simply, because all systematic factors have been neglected. Moreover, the long time between the observations of the unpolarized and the polarized stars, could also partially effect the calibration factors; because they could change with time. Another problem could come from the very high count rates, due to high brightness of the references stars. After these calibrations, photometric and polarimetric analysis of an astronomical object can be confidently conducted by using the procedures described above.

4. OBSERVATIONS, RESULTS, AND INTERPRETATION

In this part, we present fast timing photometric and X-ray observations, data analysis and results of the two mCVs, the polar HU Aquarii and intermediate polar V2069 Cygni (RX J2123.7+4217). The optical observations are performed using OPTIMA at the 1.3 m telescope of Skinakas Observatory (and previously at many different observatories for HU Aqr observations) and X-ray data are obtained by *XMM–Newton* and *Swift*/XRT space observatories.

4.1. Observatories

4.1.1. Skinakas Observatory

The Skinakas Observatory is a scientific research collaboration operated jointly by the University of Crete, the Foundation for Research and Technology-Hellas (FORTH), and MPE (Garching, Germany). It is located (Longitude: $24^o\ 53'\ 57''$, Latitude: $35^o\ 12'\ 43''$N, Altitude: 1750 m) at the top of Skinakas mountain of Mount Ida (also known as Mt. Psiloritis), at an and a distance of 60 km from Heraklion, in the island of Crete offering good conditions for high quality astronomical observations in the Mediterranean area (Charmandaris 2006).[2]

The observatory currently houses three fully functional telescopes. A 1.3 m modified Ritchey-Chretien telescope (focal ratio f/7.6), which became operational in 1995. The optical system (Figure 4.1.) was manufactured by Carl Zeiss, and the mechanical parts by DFM Engineering. Another two telescopes at the observatory are the 0.6 m remotely controlled telescope and a 0.3 m Schmidt-Cassegrain telescope. The instrumentation of the 1.3 m Telescope includes a focal reducer, a number of optical CCD cameras, and a low resolution long slit spectrograph together with a 1024x1024 near-IR camera and an echelle spectrograph.

[2] http://www.physics.uoc.gr/en/menu/skinakas.php, http://skinakas.physics.uoc.gr/en/

Figure 4.1. A photograph of 1.3 m cassegrain focus telescope of the Skinakas Observatory, Crete, Greece

4.1.2. *XMM–Newton* and *Swift* Space Observatories

XMM–Newton;

Since Earth's atmosphere blocks out all X-rays, only a telescope in space can detect and study celestial X-ray sources. The European Space Agency (ESA)'s X-ray Multi-Mirror satellite (*XMM-Newton*) is the most powerful X-ray telescope ever placed in orbit and the first flown on a X-ray observatory. It was launched on December 10 th, 1999 and carries three very advanced X-ray telescopes, with different X-ray detectors and an unprecedented effective area (each contain a mirror module with delicately nested 58 high-precision concentric mirrors, Figure 4.2.), and a 30 cm optical/UV telescope (Optical Monitor) with a micro-channel-plate pre-amplified CCD detector in its focal plane. Thus, *XMM-Newton* offers simultaneous access to two windows of the electromagnetic spectrum: X-ray and optical/UV. The mission is helping to solve a number of cosmic mysteries, ranging from enigmatic black holes, the formation of galaxies to the origins of the Universe itself (see 'XMM-Newton Users Handbook', Issue 2.9, 2011, ESA: XMM-Newton SOC).[3]

XMM-Newton provides the following three types of science instrument:

[3] http://heasarc.gsfc.nasa.gov/docs/xmm/uhb, http://xmm.esac.esa.int

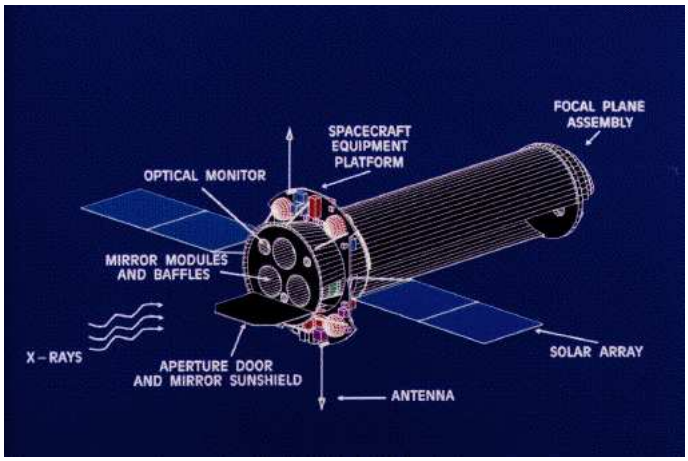

Figure 4.2. Schematic view of the *XMM-Newton* spacecraft. The focal plane assembly includes two RGS readout cameras, an EPIC PN and two EPIC MOS detectors, and the data handling and power distribution units for the cameras. [http://heasarc.gsfc.nasa.gov]

1. European Photon Imaging Camera (EPIC): 3 CCD cameras (two MOS and one pn) for X-ray imaging, spectroscopy, and X-ray photometry.

2. Reflection Grating Spectrometer (RGS): 2 essentially identical spectrometers for high-resolution X-ray spectroscopy and spectral-photometry.

3. Optical Monitor (OM): for optical/UV imaging and grism spectroscopy.

Swift Gamma-ray Burst Telescope

Swift is a first-of-its-kind multi-wavelength (gamma ray, X-ray, ultraviolet, and optical waveband) space-based observatory (Figure 4.3.) dedicated to the study of GRB science, launched on November 20, 2004. It is a sensitive, flexible, autonomous X-ray CCD imaging spectrometer designed to measure the position, spectrum, and brightness of GRBs and afterglows over a wide dynamic range covering more than 7 orders of magnitude in flux. Its three instruments [Burst Alert Telescope (BAT), X-ray Telescope (XRT) and Ultraviolet/Optical Telescope (UVOT)] work together to observe the GRBs before they end or any source in multi-wavelengths (Hill et al. 2004).[4]

When a GRB (or an energy flash) occurs, within about 10 seconds, the BAT will be the first of *Swift*'s instruments to detect and localize the burst direction which

[4] http://www.swift.psu.edu, http://swift.gsfc.nasa.gov/docs/swift

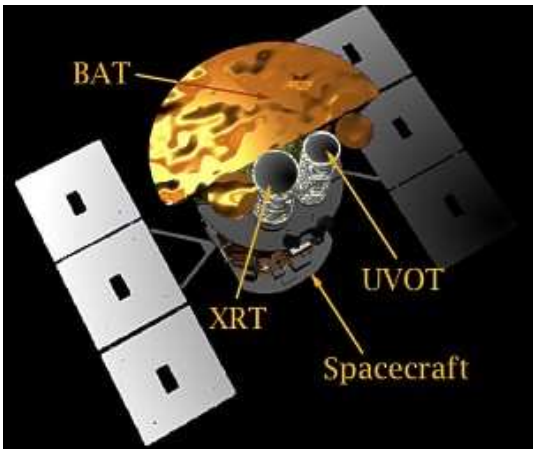

Figure 4.3. Schematic view of the *Swift* spacecraft. The *Swift* GRB Explorer carries three instruments, which work together to enable the most detailed observations of GRBs. These instruments are BAT, XRT and UVOT. [Taken from http://www.swift.psu.edu/]

is transmitted to ground observers, with an accuracy of 1 to 4 arc-minutes. After that the *Swift* spacecraft will slew to bring the GRB into the XRT and UVOT's fields of view. Within a minute after a burst, the XRT takes images and refines the BAT position, with a typical error circle of approximately $2-5$ arc-seconds radius. The XRT is also used to perform long term monitoring of GRB afterglow light curves for days to weeks after the event, depending on the brightness of the afterglow. After about 200 seconds, the UVOT produces an even more accurate localization with a sub-arc-second resolution and provides optical and ultraviolet photometry through lenticular filters and low resolution spectra ($170-650$ nm) through the use of its optical and UV grisms. The UVOT is also used to provide long term follow ups of GRB afterglow light-curves.

The XRT Mirror Assembly consists of the X-Ray Mirror Module (X-ray telescope with 12 nested mirrors, focused onto a single MOS CCD similar to those used by the XMM-Newton EPIC MOS cameras), a thermal baffle, a mirror collar and an electron deflector. The telescope has an energy range of $0.2-10$ keV.

4.2. Polar HU Aquarii

HU Aquarii (HU Aqr) is an eclipsing system belonging to the polar or AM Her type of CVs hosting a magnetic WD (with a mass of 0.88 $M_{\odot}$) accompanied by a red dwarf (with a spectral type of M4V and a mass of 0.2 $M_{\odot}$). The magnetic field of WD is strong enough to synchronize the spin period of the WD to the orbital period of the binary, which is 125 min. This system is one of the brightest polars in optical domain (with visual magnitudes from 14.6 to 18), as well as in the X-ray energy range. The system was discovered in 1993 in the ROSAT survey and has since been extensively studied in various wavelength bands (Warner 1995; Hellier 2001; Schwope et al. 1993; Schwope et al. 2001; Schwarz et al. 2009).

In HU Aqr the accreted material leaving from the red dwarf is initially not affected by the magnetic field of the WD, because it is far from WD. The material will continue to flow as thought there is no field. Close to the WD magnetosphere which typically extends beyond the L1 radius, the field (B $\sim 10^7 - 10^8$ G) begins to dominate the material. Then, the material will not orbit freely, instead flows in the form of a narrow stream, and thus, does not form an accretion disk, unlike in other non-magnetic CVs. Once the material reaches the magneto-spheric boundary, immediately after the L1 point, it is controlled magnetically, being forced to move along the field lines and forms an accretion spot (hot-spot) at the poles of the WD (Figure 2.1.)

In many systems, the WD field is tilted in a such way that one magnetic pole is oriented toward the direction of flowing material. Eclipses observed in highly inclined polar systems provide information about the stream geometry (Hellier 2001). Figure 4.4. shows two eclipses in photo-polarimetric light curves of HU Aqr. HU Aqr has a special geometry with an orbital inclination of $\sim 87^{\circ} \pm 0.8$ (Schwope et al. 2011), which make it important to investigate the planetary hypothesis. Assuming that a planetary companion has formed in the circumbinary disk, the inclination constraint removes the mass indeterminacy inherent to the eclipse timing method. Therefore its orbital ephemeris (which is a sequence of points that predicts the future positions of a celestial object moving across the sky) has been followed with precision since 1993.

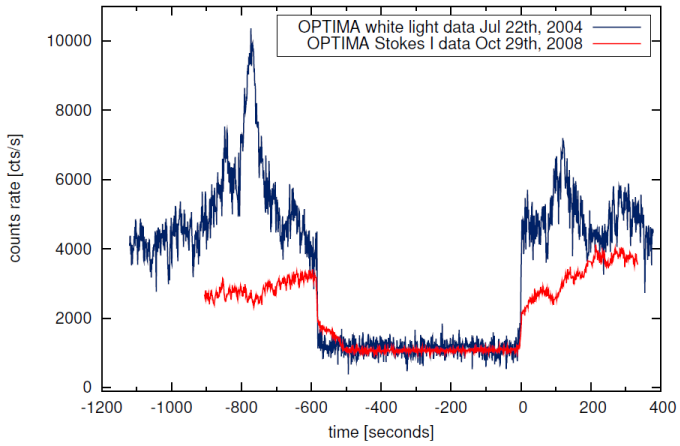

Figure 4.4. Photometric (upper) and polarimetric (lower) light curves of HU Aqr taken with OPTIMA. Before the eclipse there is a dip of the intensity (between -750th and -650th sec) caused by the eclipse of the hot-spot on the WD by the accretion stream. At around -610th s the hot-spot start to eclipse, and the light drops dramatically. Then the bright accretion stream enters in eclipse at -500th sec. The complete eclipse occurs between -500th and 00th s and during this period the observed constant brightness come from the secondary. At the end of the eclipse the hot-spot suddenly rise from behind the secondary and followed by the accretion stream at 0.05 sec. [Taken from Gozdziewski & Nasiroglu et al. (2012)]

4.2.1. Observation and Data

To follow the secular changes of the orbital period, the eclipse times of HU Aqr have been observed in optical, UV and X-rays over the last 19 yr, including regular OPTIMA observations since 1999. These collected data extend the work of Schwope et al. (2001) and Schwarz et al. (2009). Among these measurements, 68 eclipse times were obtained with OPTIMA instrument that operated mostly at the Skinakas Observatory. During the HU Aqr observations, OPTIMA was pointed at RA(J2000) = $21^h\ 07^m\ 58.^s19$, Dec(J2000) = $-05^o\ 17'\ 40.''5$, corresponding to the central aperture of the fibers bundle (Figure 4.5.). For sky background monitoring, we usually choose one out of the six hexagonally located fibers. We look for the fiber that is not by chance pointed to any source, therefore records sky background, and its response is the most similar to the central fiber response when the instrument is targeted at the dark sky. An example of sky background subtracted light curves are shown in Figure 4.4.

Table 4.1. 126 mid-egress times of HU Aqr observed in optical, UV and X-rays, obtained in the time period 1993−2007. BJD is the barycentrically corrected ephemeris OPT-ESO22 − OPTIMA photometer installed at ESO (Chile), OPT-SKO − OPTIMA operated at the Skinakas Observatory (Crete), OPT-NOT − OPTIMA operated at Nordic Optical Telescope, (Canary Islands) OPT-SAO − OPTIMA operated at South Africa Telescopes, (Sutherland). Adopted from Schwope et al. (2001); Schwarz et al. (2009)

Cycle Number	Egress Time (BJD) 2400000+	ΔBJD (d)	Telescope Instrument	Cycle Number	Egress Time (BJD) 2400000+	ΔBJD (d)	Telescope Instrument
0	49102.92000260	0.00000290	ROSAT	30276	2451731.49506483	0.00000171	OPT-SKO
1319	49217.43611200	0.00001150	MCCP	30277	2451731.58189712	0.00000189	OPT-SKO
1320	49217.52292200	0.00001150	MCCP	30287	2451732.45009015	0.00000225	OPT-SKO
1321	49217.60974900	0.00001150	MCCP	30299	2451733.49193572	0.00000333	OPT-SKO
1322	49217.69660100	0.00002310	ESO1m	30300	2451733.57875542	0.00000543	OPT-SKO
1333	49218.65161000	0.00002310	ESO1m	30310	2451734.44697401	0.00000309	OPT-SKO
1334	49218.73843900	0.00002310	ESO1m	30311	2451734.53378557	0.00000178	OPT-SKO
1367	49221.60350100	0.00002310	ESO1m	31312	2451821.44102100	0.00001150	STJ
1368	49221.69031900	0.00002310	ESO1m	31313	2451821.52784100	0.00001150	STJ
1369	49221.77714800	0.00002310	ESO1m	35043	2452145.36792500	0.00004630	AIP
2212	49294.96679440	0.00000130	ROSAT	35376	2452174.27909653	0.00000176	OPT-SKO
2213	49295.05361190	0.00000310	ROSAT	35377	2452174.36591008	0.00000216	OPT-SKO
2216	49295.31407800	0.00000240	ROSAT	35469	2452182.35338515	0.00000297	OPT-SKO
2222	49295.83499660	0.00000240	ROSAT	38098	2452410.60416255	0.00000836	OPT-SKO
2225	49296.09545910	0.00000120	ROSAT	38105	2452411.21187100	0.00005780	OM-UVM2
2226	49296.18228240	0.00000180	ROSAT	38107	2452411.38557200	0.00002310	XMM-MOS1
4241	49471.12542480	0.00001090	ROSAT	38107	2452411.38557800	0.00002310	XMM-MOS2
4409	49485.71128140	0.00002760	ROSAT	38108	2452411.47239200	0.00002310	XMM-PN
6328	49652.31962840	0.00002670	ROSAT	38109	2452411.55919321	0.00000337	OPT-SKO
6341	49653.44832830	0.00000660	ROSAT	38133	2452413.64285100	0.00001150	ULTRA-WHT
6390	49657.70253350	0.00000670	ROSAT	38145	2452414.68474000	0.00001150	ULTRA-WHT
6391	49657.78937760	0.00002000	ROSAT	39731	2452552.38184400	0.00001157	OPT-SKO
6403	49658.83119480	0.00001150	ROSAT	39742	2452553.33684100	0.00001157	OPT-SKO
6576	49673.85112920	0.00001340	ROSAT	42352	2452779.93803400	0.00005780	OM-UVM2
6579	49674.11159210	0.00000670	ROSAT	42395	2452783.67129900	0.00001150	ULTRA-WHT
10707	50032.50627770	0.00002460	ROSAT	42441	2452787.66503987	0.00000147	OPT-SAO
12607	50197.46504340	0.00001380	ROSAT	42463	2452789.57509335	0.00000142	OPT-SAO
13064	50237.14200280	0.00001040	EUVE	42464	2452789.66192721	0.00000239	OPT-SAO
13620	50285.41410400	0.00011570	AIP	42486	2452791.57194835	0.00000145	OPT-SAO
13621	50285.50087800	0.00011570	AIP	42487	2452791.65877151	0.00000236	OPT-SAO
13632	50286.45589000	0.00011570	AIP	44534	2452969.38007598	0.00000330	OPT-NOT
13707	50292.96751750	0.00001840	EUVE	44557	2452971.37693769	0.00000853	OPT-NOT
14087	50325.95925400	0.00002770	HST	47253	2453205.44470791	0.00000265	OPT-SKO
14088	50326.04607400	0.00002770	HST	47254	2453205.53152884	0.00000372	OPT-SKO
14115	50328.39032400	0.00011570	AIP	47300	2453209.52527288	0.00000375	OPT-SKO
14116	50328.47716200	0.00011570	AIP	47335	2453212.56400226	0.00000383	OPT-SKO
14138	50330.38704100	0.00011570	AIP	48265	2453293.30695695	0.00001024	OPT-SKO
14139	50330.47386600	0.00011570	AIP	48288	2453295.30382284	0.00000354	OPT-SKO
14236	50338.89548000	0.00002770	HST	48299	2453296.25883361	0.00000657	OPT-SKO
14250	50340.11098560	0.00001100	EUVE	48334	2453299.29755672	0.00000154	OPT-SKO
14740	50382.65297660	0.00001340	ROSAT	50702	2453504.88829400	0.00000560	ULTRA-VLT
14746	50383.17392890	0.00001870	EUVE	50713	2453505.84331700	0.00000560	ULTRA-VLT
16906	50570.70598840	0.00000670	ROSAT	50714	2453505.93013900	0.00000560	ULTRA-VLT
17010	50579.73534410	0.00003060	ROSAT	50724	2453506.79834200	0.00000560	ULTRA-VLT
17030	50581.47173990	0.00000950	EUVE	50725	2453506.88516200	0.00000560	ULTRA-VLT
17994	50665.16664910	0.00002030	EUVE	50737	2453507.92700800	0.00000560	ULTRA-VLT
21014	50927.36427960	0.00001340	ROSAT	51020	2453532.49715946	0.00001001	OPT-SKO
21023	50928.14564910	0.00000670	ROSAT	51032	2453533.53901696	0.00000523	OPT-SKO
21026	50928.40611600	0.00000670	ROSAT	51066	2453536.49090296	0.00000641	OPT-SKO
22478	51054.46934740	0.00000870	EUVE	51067	2453536.57772782	0.00000331	OPT-SKO
22788	51081.38371100	0.00011570	AIP	55466	2453918.50071894	0.00000459	OPT-SKO
25892	51350.87432200	0.00001150	OPT-ESO22	55535	2453924.49134258	0.00001021	OPT-SKO
25926	51353.82621900	0.00001150	OPT-ESO22	55546	2453925.44635626	0.00000745	OPT-SKO
25938	51354.86807800	0.00001150	OPT-ESO22	55627	2453932.47881640	0.00000611	OPT-SKO
27394	51481.27863600	0.00002310	AIP	55661	2453935.43070711	0.00000639	OPT-SKO
29946	51702.84433521	0.00000374	OPT-ESO22	55719	2453940.46627536	0.00001619	OPT-SKO
29957	51703.79935449	0.00000376	OPT-ESO22	59524	2454270.81798900	0.00001570	ULTRA-VLT
29958	51703.88617054	0.00000336	OPT-ESO22	59525	2454270.90481200	0.00001570	ULTRA-VLT
29955	51703.62570500	0.00008100	AIP	59558	2454273.76988400	0.00001570	ULTRA-VLT
29966	51704.58070400	0.00008100	AIP	59559	2454273.85670400	0.00001570	ULTRA-VLT
29955	51703.62570500	0.00009250	CA123	60085	2454319.52424086	0.00000735	OPT-SKO
29966	51704.58070400	0.00009250	CA123	60096	2454320.47925419	0.00000370	OPT-SKO
30265	51730.54003238	0.00000409	OPT-SKO	60097	2454320.56607692	0.00000551	OPT-SKO

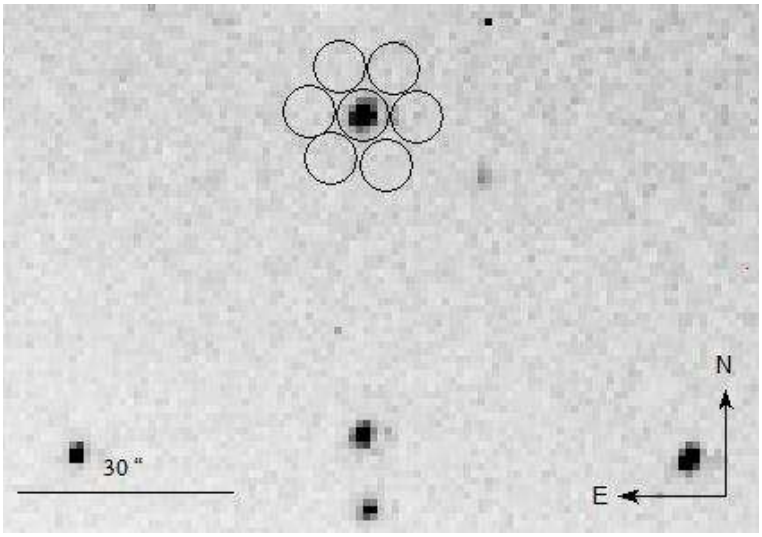

Figure 4.5. OPTIMA fiber bundle centered on HU Aqr. The ring fibers (1−6) are used to monitor the background sky simultaneously

We have generated new fits to eclipse mid-egress times of HU Aqr, as well as reanalyzed many of the already published OPTIMA data. There are 26 eclipses obtained with OPTIMA and published by Schwarz et al. (2009). We were able to reanalyze only 21 out of the 26 light curves, because only those were available in the OPTIMA archive. We derived 23 new eclipse profiles from the OPTIMA data archive spanning 1999−2007 and obtained 19 new OPTIMA optical HU Aqr light curves in 2008−2010. The HU Aqr mid-egress times for the time period 1993−2007, together with the updated OPTIMA egress times and newly derived 23 OPTIMA eclipse times (totally 126 eclipse egress times) are listed in Table 4.1. and the recent 19 eclipse mid-egress times of HU Aqr (for the time period 2008−2010) are listed in Table 4.2. Note that only some of these OPTIMA observations have been used in this thesis and already published in the literature (Nasiroglu et al. 2010). The observations and eclipse egress times were converted to Barycentric Julian Ephemeris Dates (BJD). The reference time for eclipse egress epoch zero is 1993 April 25 10:04:56 = 2449102.92009259 BJD, but is also fitted within the range of uncertainty in each individual model.

In 2011, it has also been gathered and reduced 11 observations performed at the MONET (MOnitoring NEtwork of Telescopes) project which is network of two

Table 4.2. 19 mid-egress times of HU Aqr obtained in the time period 2008−2010 with OPTIMA. BJD is the barycentrically corrected ephemeris time. OPT-SKO – OPTIMA operated at the Skinakas Observatory (Crete)

Cycle Number	Egress Time (BJD) 2400000+	ΔBJD (d)	Telescope Instrument	Cycle Number	Egress Time (BJD) 2400000+	ΔBJD (d)	Telescope Instrument
64657	54716.46714958	0.00000534	OPT-SKO	72121	2455364.49448849	0.00000286	OPT-SKO
64885	54736.26220846	0.00000382	OPT-SKO	72133	2455365.53634443	0.00000148	OPT-SKO
64886	54736.34901810	0.00000156	OPT-SKO	72225	2455373.52380443	0.00000481	OPT-SKO
65265	54769.25399263	0.00000231	OPT-SKO	72237	2455374.56564559	0.00000398	OPT-SKO
67791	54988.56227096	0.00000287	OPT-SKO	72248	2455375.52067145	0.00000403	OPT-SKO
67917	54999.50163911	0.00000169	OPT-SKO	72305	2455380.46942923	0.00000304	OPT-SKO
67918	54999.58845262	0.00000543	OPT-SKO	72351	2455384.46317475	0.00000237	OPT-SKO
68009	55007.48911622	0.00000175	OPT-SKO	72352	2455384.54999444	0.00000223	OPT-SKO
72099	55362.58443706	0.00000323	OPT-SKO	72421	2455390.54061076	0.00000127	OPT-SKO
72110	55363.53945458	0.00000193	OPT-SKO				

Table 4.3. 16 mid-egress times of HU Aqr obtained in 2011 with PIRATE, MONET/N and WFC. BJD is the barycentrically corrected ephemeris time. PIRATE – a telescope at the Astronomical Obs. of Mallorca, MONET/N – the network of telescopes at the McDonald Obs. and the SAO (South Africa), and WFC – the 1.5-m TCS (Canary Islands). Adopted from Gozdziewski & Nasiroglu et al. (2012)

Cycle Number	Egress Time (BJD) 2400000+	ΔBJD (d)	Telescope Instrument	Cycle Number	Egress Time (BJD) 2400000+	ΔBJD (d)	Telescope Instrument
73409	55476.31909710	0.00005780	PIRATE	77067	2455793.90798414	0.00000554	MONET/N
73559	55489.34216980	0.00005780	PIRATE	77078	2455794.86301793	0.00000646	MONET/N
73560	55489.42901510	0.00011560	PIRATE	77546	2455835.49494900	0.00001790	WFC
75467	55654.99542770	0.00000399	MONET/N	77557	2455836.44999050	0.00002950	WFC
75812	55684.94846078	0.00000231	MONET/N	77789	2455856.59228516	0.00000384	MONET/N
76721	55763.86814098	0.00000349	MONET/N	77802	2455857.72093992	0.00000895	MONET/N
77031	55790.78245708	0.00000387	MONET/N	77823	2455859.54417862	0.00000662	MONET/N
77066	55793.82115561	0.00000773	MONET/N	78100	2455883.59340375	0.00000222	MONET/N

1.2 m telescopes operated by the Georg-August-Universität, Göttingen, the McDonald Observatory, and the South African Astronomical Observatory. These precision data in white light (500−800 nm) were binned in 5 s intervals, with 10^{-6} d (0.1 s) accuracy, separated by 3 s readout. Additionally, 5 egress times in white light were obtained from the eclipse observations of HU Aqr (three with PIRATE telescope equipped with the SBIG STL1001E CCD camera (Holmes et al. 2011) and two with the 1.5 m Carlos Sanchez Telescope (TCS) equipped with Wide Fast Cam). These new collected 16 mid-egress times are listed in Table 4.3. The currently available data set of HU Aqr egress times consists of 171 measurements in total, including 10 points presented in Qian et al. (2011). All of these eclipse egress times have been already published in the most recent literature, in Gozdziewski & Nasiroglu et al. (2012).

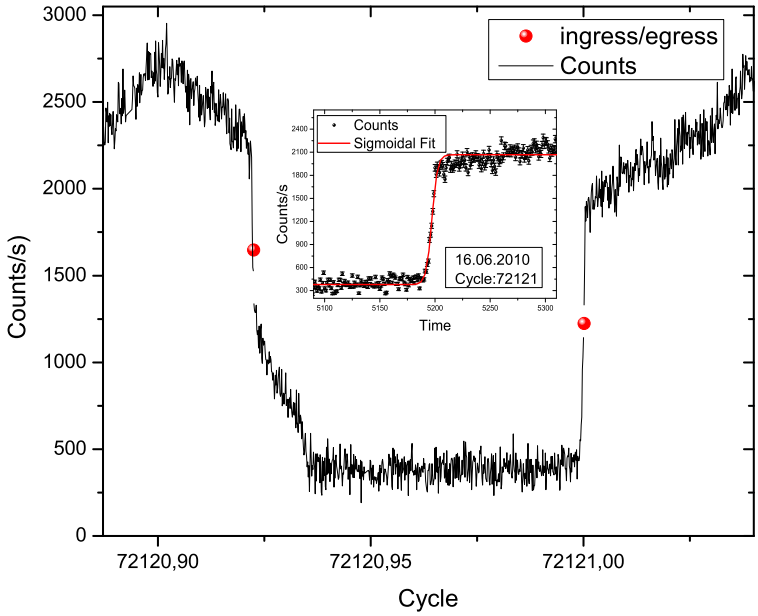

Figure 4.6. An example for sigmoid fit on a eclipse egress of HU Aqr. The reference for phase zero (= 0) is the mid-time of the eclipse egress, which is obtained from a sigmoid fit (Equation (4.1)). The 'mid-time' x_0 is fitted with an accuracy of 0.25 s for the eclipse egress no: 72121 (in 16 June 2010). The exponential scale Δx was found as 2.53 ± 0.2 s

4.2.2. Ephemeris Calculation

Sigmoid Fitting and Error Estimates;

Measuring the time of mid-egress properly is critical to obtain the **O**bserved minus **C**alculated (O−C) diagrams, since it is the time marker of the eclipse (Schwope et al. 2001; Schwarz et al. 2009). To determine the mid-egress times we fitted the OPTIMA count rates with a sigmoid function and took the half intensity point x_0 as reference (Equation (4.1)). Figure 4.6. shows an example for sigmoid fit on the egress and ingress times of HU Aqr. The results of the sigmoid fits with error estimates for OPTIMA data are listed in Table 4.1. and Table 4.2. The sigmoid function is

$$y(x) = A_1 + (A_2 - A_1)/(1 + exp(x_0 - x)/\Delta x) \tag{4.1}$$

where,

x_0: half intensity or the 'mid-point' between limiting values A_1 and A_2,

Δx: width of the range of the change in the x value corresponding to the change in the y value.

A_1: initial counts value before the egress; $y(-\infty)$,

A_2: final counts value after the egress; $y(+\infty)$.

Time−Phase Conversion;

A mean light curve of a periodic variable star can be created by using a phase scale conversion of the observation times. The phase (ϕ) conversion for each observational time is simply expressed as a fraction of the period P. This phase conservation can be shown as

$$Q = (T - T_0)/P = E(T) + \phi \tag{4.2}$$

where Q has both integer and fractional parts as $E(T)$ and (ϕ), respectively. $E(T)$ is the whole number of cycles of the phenomena (primary eclipses) since the epoch (reference time) is T_0, ϕ is the corresponding phase and T is the observation times of the object (Budding & Demircan 2007).

4.2.3. Accretion Spot Ephemeris of HU Aquarii

We adopted Schwope et al. (2001) and Schwarz et al. (2009)' list of egress measurement of HU Aqr in optical, UV and X-rays, and updated the eclipse ephemeris using 8 new mid-egress times measured in 2008-2009 with OPTIMA (first 8 cycles in Table 4.2. cycles number spanning 64657−68009 (Nasiroglu et al. 2010)).

We calculated the eclipse ephemeris using different least square fit models (linear, quadratic and sinusoidal functions). The methods of the least square consider the distances from each data point to the best fit line, which called deviations. For the best fit those deviations should be as small as possible in the least-squares. The sum of all of the deviations squared which is defined as the difference between the observed value and the value provided by the model, is called the residual (χ^2),

$$\chi^2 = \sum_{i=1}^{n} [y_i - f(x_i)]^2 \tag{4.3}$$

where, y_i is the observed eclipse egress time (T_{obs}) and $f(x_i)$ is the calculated egress value from the best fit line. It is standard and sensible practice to define a calculated ephemeris (T_{calc}) for a source of variable brightness of the form,

$$T_{calc} = T_{ref} + E.P_{ref} \tag{4.4}$$

where, T_{ref} and P_{ref} are reference time and period of the eclipse egress, respectively, calculated from the best fit line, E is the number of the eclipse cycles (orbital epoch) in the period P. Additionally, the chi-squared divided by the number of degrees of freedom which is called reduced chi-squared (χ^2_{red}) shown as

$$\chi^2_{red} = \chi^2/\nu \tag{4.5}$$

here, $\nu = (N - n - 1)$ is the number of degrees of freedom, N is the number of the observations, and n is the number of fitted parameters (Budding & Demircan 2007; Andrae et al. 2010). The best-fit parameters for each fit model together with their errors (1σ uncertainty) are calculated down one by one.

Linear Ephemeris;

For the eclipsing binary HU Aqr, the collected 111 mid-egress times (measured in the optical, UV and X-rays band, which listed in paper of Schwarz et al. (2009) and together with the 8 mid-egress times obtained in 2008-2009 with OPTIMA, first 8 mid-egress time listed in Table 4.2.) spreading about 17 yr from 1992 to 2009, might give some new information about period change of the system. Figure 4.7. shows the least-squares linear fitting to the entire observed egress times.

The baseline linear fit to 111 observed egress times yielded the ephemeris Min I (in BJD). The reduced χ^2 is ~ 141 and the mean error in the last digits for each term

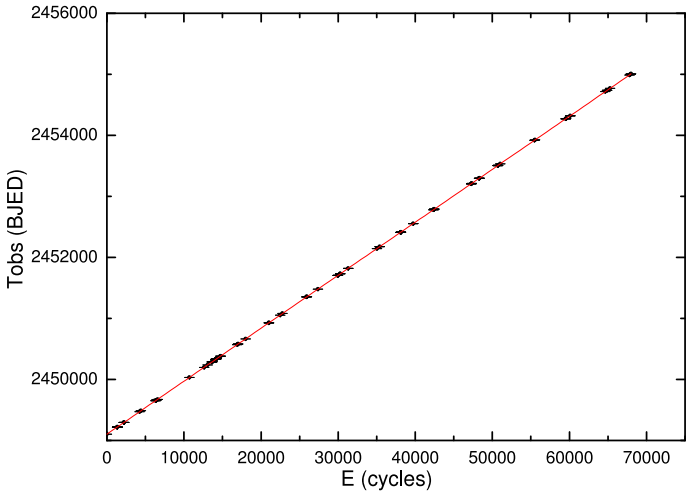

Figure 4.7. Entire observed egress times of HU Aqr and the least-squares linear fit ($f(x) = a + bx$, solid line)

is given in parentheses:

$$MinI = 2449102.9200653(79) + E \times 0.0868204073(2)\ [BJD] \tag{4.6}$$

The corresponding $(O-C)_1$ values of the linear ephemeris is shown in Figure 4.8. Assuming that all the (O−C) values show a roughly sinusoidal variation we applied a least-squares sine fit that reveals the following ephemeris equation with the reduced χ^2 of ~ 38:

$$(O-C)_1 = 7.75(59) + 13.14(79) \times sin\{2 \times \pi[E - 9980(569)]/64426(664)\}\ [s] \tag{4.7}$$

This sinusoidal variation with an amplitude of 13.1 ± 0.8 s has a period of 15.3 ± 0.2 yr. The remaining residuals of egress times $(O-C)_2$ with respect to the ephemeris including the Equations 4.6 and 4.7 are plotted in Figure 4.9. A second least-squares sine fit to these residual values yields a second cyclic ephemeris with a reduced χ^2 of ~ 11.7,

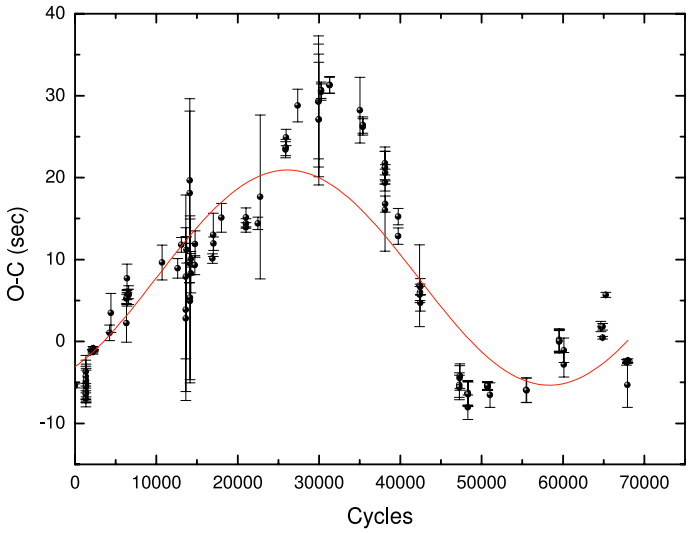

Figure 4.8. O−*C* diagram of HU Aqr with the remaining sine fit (line). The O−C values have been calculated according to the ephemeris in Equation (4.6)

$$(O-C)_2 = 0.324(335) + 6.6(4) \times sin\{2 \times \pi[E - 2229(239)]/25742(184)\}\ [s] \quad (4.8)$$

The remaining sine fit results indicates a cyclical variation with a period of 6.12±0.04 yr (P=$\omega P_{orb}/365.25$ and $\omega = 25742(184)$ from Equation 4.7, where P_{orb} is the orbital period of HU Aqr) and a semi-amplitude of 6.6 ±0.4 s. Schwarz et al. (2009) found similar variations with periods of 13 and 6.99 yr and speculated that these periodic variations might occur because of shape changes induced by a variable magnetic field.

Quadratic Ephemeris;

A weighted quadratic regression to the collected 111 egress times yields the following ephemeris (Min I) with a reduced χ^2 of ~ 91 and mean error for each term:

$$\begin{aligned} MinI = 2449102.9200370(73) + E \times 0.086820416(1) \\ -E^2 \times [1.29(17) \times 10^{-13}] \quad [BJD] \end{aligned} \quad (4.9)$$

This sinusoidal variation with an amplitude of 13.1 $\pm$ 0.8 s has a period of 15.3 $\pm$ 0.2 yr.

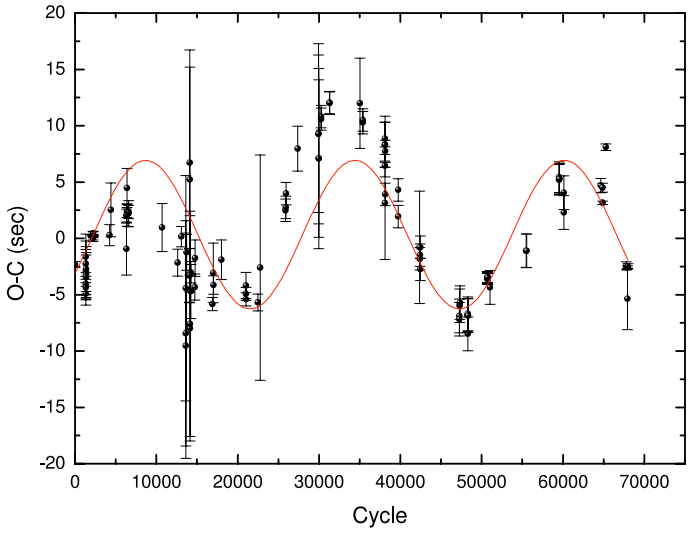

Figure 4.9. The residual of eclipse egress times w.r.t. an ephemeris including models in Equation (4.6) and (4.7) with the remaining fit (line) according to model in Equation (4.8)

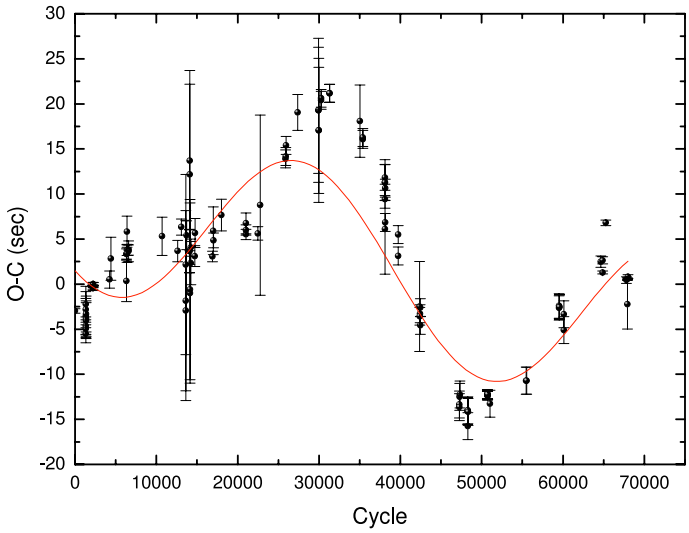

Figure 4.10. (O−C) diagram of HU Aqr with the best least squares sinusoidal fit (line). The (O−C) differences have been calculated according to the quadratic ephemeris in Equation (4.9)

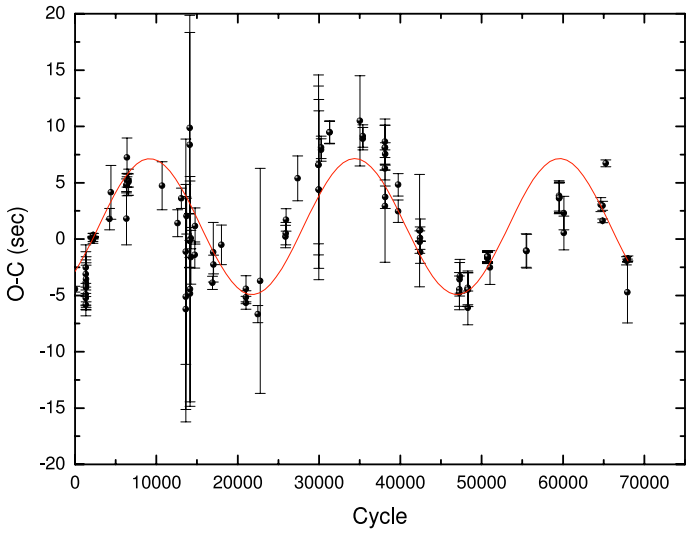

Figure 4.11. Residual of eclipse egress times w.r.t. an ephemeris including models in Equations (4.9) and (4.10) with the remaining fit (line) according to model in Equation (4.11)

The corresponding residual $(O-C)_3$ of the quadratic ephemeris is shown in Figure 4.10. The general trend of $(O-C)_3$ curve can be described by a combination of a linear and sinusoidal variations with an amplitude of 9.8 $\pm$ 0.7 s and a period of 11.0 $\pm$ 0.2 yr. Using a second least-squares fitting on the $(O-C)_3$ values yields the new ephemeris with the reduced $\chi^2 \sim 27.6$,

$$(O-C)_3 = 9.39(71) - E \times 204(17) \times 10^{-6} + 9.81(67) \times sin\{2\pi[E - 16167(699)]/46109(897)\}\ [s] \tag{4.10}$$

The resulting residuals $(O-C)_4$ after application of Equations (4.9) and (4.10) are plotted in Figure 4.11. and show periodic variation similar to Figure 4.9. A second least-squares sine fitting to these values yields a new cyclic ephemeris with the reduced $\chi^2 \sim 6.8$,

$$(O-C)_4 = 1.10(\pm25) + 6.04(\pm34) \times sin\{2\pi[E - 2890(\pm191)]/25196(\pm146)\}\ [s] \tag{4.11}$$

As can be seen in Figure 4.9. this Sinusoidal ephemeris gives a good fit to the general trend of the (O−C) curve. This sine fit reveals a periodic oscillation with a semi-amplitude of 6.0 (±0.3) s and a period of 5.99(±0.03) yr. These results are nearly the same as we calculated in first model.

Using Equation (4.4), the cycle number of the eclipse of the system can be derived as $E = (T - T_{ref})/P$ and it follows that $dE/dT = 1/P$, therefore we can calculate the change rate of the orbital period at any time by

$$dP/dT = \dot{P} = (dP/dE).(dE/dT) = (1/P)(dP/dE) \tag{4.12}$$

From a quadratic form $\Delta T(E) = a + bE + cE^2$, we can derive $dP/dE = 2c$ (Hilditch 2001). Thus, an ephemeris curve that displays a quadratic form is proving the period changing at a constant rate with respect to the cycle number E, and the coefficient of the E^2 term is $c = P\dot{P}/2$. This c coefficient can be determined from the ephemeris curve by a quadratic least-squares solution that represent the observations correctly. Using the relation $\dot{P} = 2c/P$ and the coefficient of the quadratic term $c = -1.29(17) \times 10^{-13}$ (Equation (4.9)), we calculated a continuous orbital period decrease of $\dot{P}_{orb} = (-3.0 \pm 0.4) \times 10^{-12}$ ss^{-1}. Schwope et al. (2001) calculated a period decrease of $\dot{P}_{orb} = -10 \times 10^{-12}$ ss^{-1}, Schwarz et al. (2009) estimated $\dot{P}_{orb} = (-7... - 11) \times 10^{-12}$ ss^{-1}, and Vogel et al. (2008) obtained $\dot{P}_{orb} = -13.3 \times 10^{-12}$ ss^{-1}.

4.2.4. Period Changes in HU Aquarii

From the analysis of the (O−C) curve of HU Aqr, we found a periodic variation which is superimposed on a long-term period decrease, $\dot{P}_{orb} = (-3.0 \pm 0.4) \times 10^{-12}$ ss^{-1}. This kind of periodic variations of (O−C) diagrams for binary systems have often been explained as a effect related to the one of three mechanisms: (i) the presence of a third body orbiting the binary, (ii) the magnetic activity in the binary system and (iii) the angular momentum loss by gravitational radiation or magnetic braking (Hilditch

2001; Qian & Boonrucksar 2003; Brinkworth et al. 2006; Budding & Demircan 2007; Manzoori 2007; Beuermann et al. 2011; and reference therein).

Third Body Orbiting the Binary;

The presence of smaller 'planetary' bodies orbiting the compact binary at large distances. This mechanism effects the light-travel-time (LTT), which is seen as a small but significant changes (a monotonic increase or decrease) in the binary period. For example, when the binary moves towards the observer, the light from the eclipse may seem to reach much faster to the observer (take shorter time) than when the binary is moving away. Therefore, the LTT effect causes the times of the eclipses to trace out as a cyclic changes in the (O−C) diagram. The period, amplitude and shape of this sinusoid depend on the period, semi-major axis and eccentricity of the binary orbit around the system centre of mass.

For HU Aqr, if the period variations occur as a result of the LTT effect via the presence of additional bodies orbiting the binary with the semi-amplitudes of 9.8 $\pm$ 0.7 s and 6.0 $\pm$ 0.3 s (from the quadratic plus sinusoidal ephemeris, for long and short period oscillations, respectively) of the (O−C) variations, the physical parameters for two bodies are calculated by using the mass function (*f(m)*) which is given in the following:

$$f(m) = \frac{(M_3 \sin i')^3}{(M_1 + M_2 + M_3)^2} = \frac{4\pi^2}{GT_3^2} \times (a'_{12} \sin i')^3 \tag{4.13}$$

where, M_1, M_2 and M_3 are the masses of the primary, the secondary and the third body, respectively, i' is the angle between the line of sight and the normal of the orbital plane (the orbital inclination), T is the orbital period of the third body, G is the gravitational constant,[5] a'_{12} is the semi-amplitude of the orbital motion of the system (here is the semi-amplitude of (O−C) oscillation in AU[6]) and f(m) is the mass function of the observed system which provides a lower limit on the mass of unseen companion star (or third body). The calculated mass functions for the two bodies are $f_1(m)$ = 6.19

[5] Gravitational constant: 6.674 E-08 cm^3/gs^2

[6] 1 AU (astronomical unit): 1.49597870691 E+13 cm

$(\pm 1.5) \times 10^{-8}$ and $f_2(m)$ = 4.77 $(\pm 0.7) \times 10^{-8}$. Taking the absolute parameters for HU Aqr, $M_1 = \sim 0.88\ M_\odot$ and $M_2 = \sim 0.21\ M_\odot$ and if we assume the compact binary and its 'outer' bodies move in co-planar orbits (with an inclination of 85.5°, given by Vogel et al. (2008)) the values of the mass, the orbital radius and the orbital period of the two bodies are calculated to be: the first one with a mass of 4.42 (±0.28) $M_{Jupiter}$ at distance of 5.1 (±0.07) AU and period of 11.0 (±0.2) yr, and second one with a mass of 4.05 (±0.2) $M_{Jupiter}$ at distance of 3.4 (±0.02) AU and period of 6 (±0.03) yr.

Magnetic Activity in the Binary System;

The (O−C) variability can also be caused by the magnetic activity in the binary system, as a consequence of possible magnetic cycles in both components (Applegate mechanism, which has been put forward by Applegate (1992), and modified by Lanza et al. (1998). Applegate (1992) proposed that the orbital period modulations observed in binary stars can be explained by the gravitational coupling of the binary orbit to changes in the shape of the magnetically active star in the system. The shape changes are assumed to be driven by the solar type magnetic activity cycles. In the mechanism, it has been assumed that a certain amount of angular momentum is periodically exchanged between the inner and the outer parts of the convection zone, and therefore the shape (oblateness) of the star changes when the star goes through its activity cycles. This change will be communicated to the orbit by gravity, leading to variations in the orbital period of the system.

If the Applegate mechanism is the case in HU Aqr, by inserting the physical parameters given by Vogel et al. (2008), $M_1 = \sim 0.88\ M_\odot$ and $M_2 = \sim 0.21\ M_\odot$ $R_1 = \sim 0.01\ R_\odot$ and $R_2 = \sim 0.22\ R_\odot$ and using the equation given by Applegate (1992), and Lanza et al. (1998):

$$\frac{\Delta P}{P} = -9\left(\frac{R_{act}}{a}\right)^2 \frac{\Delta Q}{M_{act} R_{act}^2} = -9\frac{\Delta Q}{M_{act} a^2} \tag{4.14}$$

where ΔP is the orbital period change during the observation cycles (T_{obs} = 16.177 yr), P is the orbital period of the system, ΔQ is the gravitational quadrupole moment of the

active star, a is the orbital separation of the binary (0.004 AU, given by Newton's form of Keplers third law $a = (P_{orb}/2\pi)^{2/3}(GM)^{1/3} = (GM/\omega^2)^{1/3}$, where ω is the angular velocity of the binary), M_{act} and R_{act} are the mass and radius of the active star. In order to reproduce the orbital period change ($\Delta P = T_{obs} \times \dot{P}_{orb} = 1.53 \times 10^{-3}$s) in the system the required quadruple moment changes are calculated to be 1.388×10^{47} g.cm^2 and 0.334×10^{47} g.cm^2 for the primary and the secondary component, respectively. The Applegate mechanism for the possible sinusoidal modulation of the orbital period in the HU Aqr data was also studied in detail by Vogel et al. (2008) and by Schwarz et al. (2009). They discarded this possibility since the HU Aqr stellar setup does not provide enough energy to drive changes of the orbital period.

Angular Momentum Loss from the Binary System;

The period changes in binary systems can also be resulted from the angular momentum loss by magnetic braking or gravitational radiation (Andronov et al. 2003; Brinkworth et al. 2006; Vogel 2008; and reference therein). The secondary star in the binary possesses a magnetic field powered by a shell dynamo mechanism. In combination with the stellar wind this leads to an angular momentum loss which is depending on the magnetic field strength and the wind loss rate of the secondary. This mechanism is called shortly 'magnetic braking'. Gravitational radiation is a second angular momentum loss mechanism, which is important at short periods. While the binary systems emit gravitational radiation, they carries away angular momentum. The angular momentum loss rate by the stellar wind is much bigger than the angular momentum loss rate caused by gravitational radiation. The rates of angular momentum loss caused by both mechanisms must be added together to find the total angular momentum loss for the system. This loss rate increases as the orbital separation decreases, but it decreases as the total mass of the system decreases.

The total angular momentum 'J' and the angular momentum loss '$\dot{J}$' for constant masses of the primary and the secondary star with a low mean accretion rates in CVs (the mass transfer can be neglected, $\sim< 10^{-10}$ $M_\odot$ yr^{-1}, for the systems below the period gap) can be calculated by Equations (4.15) and (4.16), respectively, where, M is total mass (M_1 + M_2), P_{orb} and $\dot{P}_{orb}$ are the orbital period and orbital period

decrease of the binary system, respectively.

$$J = M_1 M_2 \left(\frac{Ga}{M}\right)^{1/2} \tag{4.15}$$

$$\dot{J} = \frac{1}{3}\left(\frac{G^2}{2\pi M}\right)^{\frac{1}{3}} M_1 M_2 \frac{\dot{P}_{orb}}{P_{orb}^{\frac{2}{3}}} \tag{4.16}$$

By inserting the physical parameters of HU Aqr, the calculated values of angular momentum and the observed angular momentum loss of the system are J = 9.95 $\times 10^{50}$ erg.s and $\dot{J}_{obs} = -1.33 \times 10^{35}$ erg, respectively. $\dot{J}_{obs}$ value is about 3 times smaller than the value obtained by Vogel et al. (2008).

The average angular momentum loss caused by the gravitational radiation ($\dot{J}_{grav}$ = -1.026 $\times 10^{34}$ erg) for HU Aqr is calculated from Equation (4.17), where, c is the velocity of light[7] .

$$\left(\frac{dJ}{dt}\right)_{grav} = -\frac{32}{5}\frac{G^{7/2}}{c^5}\, a^{-7/2} M_1^2 M_2^2 M^{1/2} \tag{4.17}$$

This value accounts only for a small fraction of the angular momentum loss, the dominant part is compatible with magnetic breaking.

In the previous work, Vogel (2008) calculated the angular momentum loss for HU Aqr caused by magnetic braking, using a reduced magnetic braking model '$\dot{J}_{rmb}$' (Equation (4.18)) presented in Andronov et al. (2003) and a standard magnetic braking model '$\dot{J}_{mb}$' (Equation (4.19)) developed by Rappaport et al. (1983):

$$\left(\frac{dJ}{dt}\right)_{mb} = -3.8 \times 10^{-30} M R_{\odot}^4 \left(\frac{R}{R_{\odot}}\right)^{\gamma} \omega^3 \tag{4.18}$$

[7] Velocity of light: 2.99792458 E+10 cm/s

$$\left(\frac{dJ}{dt}\right)_{rmb} = -K_{\omega}\left(\frac{R_2}{M_2}\right)^{1/2}\frac{2\pi}{P_{orb}}\omega_{crit}^2 \tag{4.19}$$

where, $0 \leq \gamma \leq 4$ is a dimensionless parameter, ω is the angular frequency of rotation of secondary star (binary period for CVs) in rad s^{-1}, ω_{crit} (=$2\pi/P_{orb}$) is the critical angular frequency at which the angular momentum loss rate enters the saturated regime. The constant K_{ω} = 2.7×10^{47} g cm s^{-1} is calibrated to give the known solar rotation rate at the age of the Sun, R_2 and M_2 are radius and mass of the secondary star, respectively.

According to the standard CV theory, while the CVs evolve through the period gap (2−3 h) the magnetic braking is cut-off at orbital period of 3 h as the secondary becomes fully convective (radiative/convective boundary stop to anchor the magnetic field, so it either dissipates or is rearranged, resulting in a lowered stellar wind). Mass transfer ceases until the system evolves to a period of 2 h and gravitational radiation becomes strong enough to drive mass transfer, repopulating the period distribution below the gap (Andronov et al. 2003; Brinkworth et al. 2006).

The standard magnetic braking model (commonly used in CV studies) is based on studies of the solar wind and the rotation periods of solar-type stars in open clusters. Andronov et al. (2003) suggested that the reduced magnetic braking model inferred from open-cluster low-mass stars shows that there is no cut-off of the magnetic braking when the secondary becomes fully convective and that the angular momentum loss rate predicted by the standard model is to high. In both models the cut-off of magnetic braking is ignored. By inserting the physical parameters, the resulting angular momentum loss for HU Aqr $5.6\times10^{34} < \dot{J}_{mb} < 2.2\times10^{37}$ erg and $\dot{J}_{rmb}$ = 1.4×10^{33} erg. The $\dot{J}_{grav}$ together with the $\dot{J}_{rmb}$ is one orders of magnitude below the observed value $\dot{J}_{obs}$ and thus these values are not able to explain the period decrease of HU Aqr. The standart magnetic braking model can explain the observed angular momentum loss rates implied by the observed period decrease, but this induces severe problems since neither period gap nor period minimum are compatible with that explanation by Vogel et al. (2008).

In an alternative explanation, if the period change is due to conservative mass exchange between the the two components, the mass transfer rate ($\dot{M}_2$) of the secondary can be calculated by Equation (4.20).

$$\dot{M}_2 = \frac{\dot{P_{orb}}}{P_{orb}} \frac{M_1 M_2}{3(M_1 - M_2)} \tag{4.20}$$

The resultant mass transfer rate from the secondary star for the derived orbital period is $1.16 \times 10^{-9}\ M_{\odot}\ yr^{-1}$.

4.3. Intermediate Polar V2069 Cygni

V2069 Cyg (RX J2123.7+4217) was discovered as a hard X-ray source by Motch et al. (1996) and identified as a CV. Thorstensen & Taylor (2001) reported a most probable orbital period of 0.311683 d (7.48 h) from their spectroscopic observations. de Martino et al. (2009) performed a preliminary analysis of *XMM–Newton* observations that showed a strong peak at the fundamental frequency of 116.3 cycles d^{-1} and harmonics up to the third in the power spectrum. Additionally, the sinusoidal fit to the profile from both EPIC-pn and EPIC-MOS data revealed a fundamental period of 743.2 ± 0.4 s and 55% pulsed fraction. They also reported a spectral fit consisting of a 56 eV black body (bbody) component plus 16 keV thermal plasma emission and a Gaussian at 6.4 keV emission line with an equivalent width (EW) of 159 eV, being absorbed by a partial (69%) covering model with $N_{\rm H} = 1.1 \times 10^{23}$ cm^{-2} and a total absorber with $N_{\rm H} = 5 \times 10^{21}$ cm^{-2}. Their spectral analysis confirmed that V2069 Cyg is a hard X-ray emitting IP with a soft X-ray component. Butters et al. (2011) carried out an analysis of *RXTE* data in the $2.0-10.0$ keV energy range and found the spin period of the V2069 Cyg WD to be 743.2 ± 0.9 s with a double-peak modulation. They also reported the spectral results with a 6.4 keV iron line which is typical of IPs.

In IPs the WD has weaker magnetic field strengths (typically $1-10$ MG) than polars, not strong enough to force the WD to rotate with the same period of the binary orbit, therefore $P_{spin} < P_{orb}$. In these systems the mass accretion from the secondary

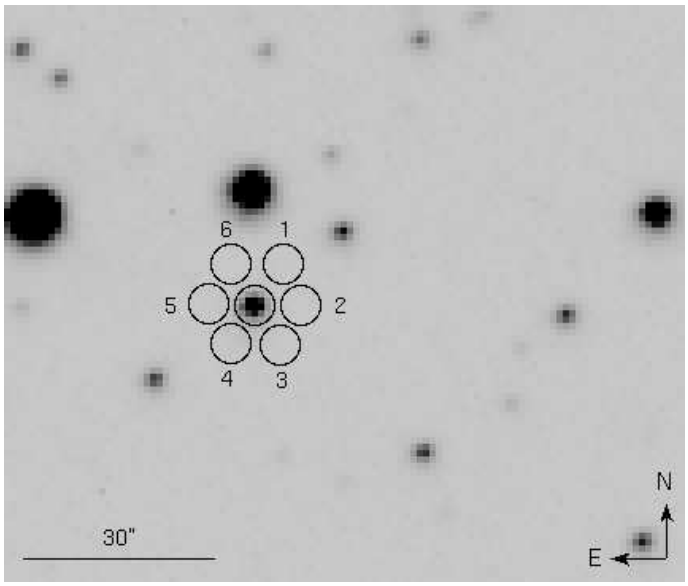

Figure 4.12. OPTIMA fiber bundle centered on V2069 Cyg. The ring fibers (1–6) are used to monitor the background sky simultaneously

happens either through an accretion disk or accretion stream (or disc-overflow accretion, depending on WD magnetic fields strength of the WD) until it reaches to the magnetospheric boundary. The accretion in the case of a weak magnetic field (or a high accretion rate), so called '*disk-fed accretion*', the WD has smaller magnetosphere and the accreted material can form an accretion disk around WD. The inner region of the accretion disk is truncated by the WD magnetic field (up to point of the magnetospheric boundary) which channels the material into accretion curtains towards the magnetic poles. However, in the case of the'*stream-fed accretion*' or 'discless' scenario the WD has stronger magnetic fields and larger magnetosphere, therefore the magnetic field might prevents formation of an accretion disk, and thus the accreted material flows directly in the form of a narrow stream and encounters the magnetosphere, where it becomes coupled to the magnetic field lines. The third possible accretion scenerio, which is some combination of both disc-fed and stream-fed accretion, is known as '*disk overflow accretion*'. In this scenerio an acrretion disk can be form but a part of the accretion stream will bypass the accretion disk outside the orbital plane, interact with the WD magnetosphere, and flow down towards the field lines (Norton et

Table 4.4. Log of the photometric (OPTIMA) and X-ray (*Swift*/XRT and *XMM–Newton*/EPIC) observations of V2069 Cyg

No.	Date 2009	Detector	ObsBeg (MJD)	Expo. (h)
1	Jul 02	OPTIMA	55014.922	2.5
2	Jul 18	OPTIMA	55030.951	1.2
3	Jul 19	OPTIMA	55031.845	2.1
4	Jul 21	OPTIMA	55033.820	4.1
5	Jul 22	OPTIMA	55034.871	3.0
6	Jul 24	OPTIMA	55036.804	1.2
7	Jul 26	OPTIMA	55038.040	1.4
8	Jul 26	OPTIMA	55038.827	1.7
9	Jul 28	OPTIMA	55040.897	1.5
A	Jul 21	*Swift*	55033.786	0.8
B	Jul 22	*Swift*	55034.048	0.9
C	Apr 30	*XMM–Newton*	54951.463	7.8

al. 1999; Evans et al. 2004; Staude et al. 2008; and reference therein).

Then, in these systems, the magnetically channeled accretion material falls onto the WD almost radially at free-fall velocities thus forming stand-off shocks near the WD surface and heating the material to 10^8 K, and transforming kinetic energy into radiation (hard X-ray/soft gamma-ray emission from the bremsstrahlung cooling and cyclotron emission in the optical and IR) in the hot post-shock region. The soft X-ray emission is also observed in some IPs which is believed to arise from reprocessing of the hard X-rays, see Figure 2.4. in Section 2.3 (Aizu 1973; Patterson 1994; Warner 1995; Hellier 2001). Since the magnetic axis (accretion regions) is offset from the spin axis of the WD, the accretion process will give rise in the X-ray and optical wavelength bands pulsating at the WD spin period which is the defining characteristic of IPs. In addition to the spin period, if the material transferred directly via an accretion stream (stream-fed or disc-overflow accretion) towards the magnetic poles of WD, the accreted material falling onto each pole will vary according to the rotation phase of the WD in the reference frame of the binary, and produce a periodic pulsation at the beat period between the spin and orbital cycles, where $1/P_{beat} = 1/P_{spin} - 1/P_{orbit}$ (Norton et al. 1999; Evans et al. 2004; Staude et al. 2008).

4.3.1. Observations and Data

High Time Resolved Photometric Observations;

We performed the photometric observations of V2069 Cyg with OPTIMA instrument at the 1.3 m telescope of Skinakas Observatory. Single photons are recorded in all channels with absolute time tagging accuracy of $\sim$4 μs (Kanbach et al. 2003). To observe V2069 Cyg OPTIMA was pointed at RA(J2000) = 21^h 23^m $44.^s82$, Dec(J2000) = $+42^o$ $18'$ $01.''7$, corresponding to the central aperture of a hexagonal bundle of fibers (Figure 4.12.) A separate fiber is located at a distance of $\sim 1'$ as a night sky background monitor. The log of the observations is given in Table 4.4.

***Swift*/XRT Observations**;

The simultaneous soft X-ray observations of V2069 Cyg were performed with the *Swift*'s X-ray telescope (XRT; Burrows etal. 2005) in the energy range of 0.3$-$10 keV (Table 4.4.) The CCD of the *Swift*/XRT was operated in the Photon-Counting mode which retains full imaging and spectroscopic resolution with a time resolution of 2.54 s. The *Swift* source position is: RA(J2000) = 21^h 23^m $44.^s69$ Dec.(J2000) = $+42^o$ $17'$ $59.''6$ with an error radius of $3.''5$. For the XRT data we applied the following types of filters: grade 0–4, and a circular region filter centered at the position of the source with 10-pixels radius (corresponding to $\sim 23.''5$).

***XMM–Newton* Observations**;

The *XMM–Newton* observation of V2069 Cyg was performed on 2009 April 30 (Observation ID: 0601270101, Table 4.4.). The EPIC instruments were operated in full-frame imaging mode with thin and medium optical blocking filters for EPIC-pn (Strueder et al. 2001) and EPIC-MOS (Turner et al. 2001), respectively. The exposure times were 26433 s for EPIC-pn, 28023 s for EPIC-MOS1, 28029 s for EPIC-MOS2. We used the *XMM–Newton* Science Analysis Software (SAS) v.10.0.0 to process the event files. The source was placed on CCD 4 of the pn, and on CCD 1 of both MOS instruments. The source coordinates derived from a standard source detection analysis of the combined EPIC images are RA(J2000) = 21^h 23^m $44.^s60$, Dec(J2000) = $+42^o$ $18'$ $00.''1$. We used the *eregionanalyse* task of SAS to identify circular photon

extraction regions (with radius of $36''$ $53''$, $56''$ for pn, MOS1 and MOS2 respectively) around the source by optimizing the signal to noise ratio. A circular region was used for the background extraction from a nearby source-free area (with radius of $35.''$) on the same CCD as the source. The source light curve extraction was done using the *etimeget* and *epiclccor* and the spectrum extraction was done using the *evselect* tasks within SAS. To create spectra we selected single-pixel events (PATTERN=0) from EPIC-pn data and single- to quadruple-pixel events (PATTERN 0–12) from EPIC-MOS data. For the timing analysis we used single- and double-pixel events from the EPIC-pn data (PATTERN 0–4), and single- to quadruple-pixel events from EPIC-MOS data. We sorted out bad CCD pixels and columns (FLAG=0). After the standard pipeline processing of the EPIC photon event files, we rejected some part of the data which was affected by very high soft proton background. We created good time intervals (GTIs) from background light curves ($7.0-15.0$ keV band) using count rates below 15 cts ks^{-1} arc-min^{-2} for EPIC-pn data and 2.5 cts ks^{-1} arc-min^{-2} for MOS data. The spectra of EPIC-pn, EPIC-MOS1 and EPIC-MOS2 contain 10576, 5908, and 6000 background subtracted counts, respectively.

4.3.2. Data Analysis

Timing Analysis of the OPTIMA and *Swift*/XRT Data;

We analyzed the data using the *HEASOFT* analysis package v.6.9. The X-ray and optical photon arrival times were converted to the solar system barycenter. OPTIMA count rates of the source were obtained from the central fiber (see Figure 4.12.). Raw data were binned with 1 s and, after 'flat-fielding' all fiber channels on a source free region of sky background, the corresponding calibrated background counts were subtracted. We chose the fiber number 5 as the best representative of the background, because its APD response was closest to the APD response of channel 0 (Figure 4.13.).

The resulting photometric light curve shows a prominent periodic variability (Figure 4.14.). The power spectrum was computed with the Fast Fourier Transform (FFT) algorithm and normalized such that the white noise level expected from the data

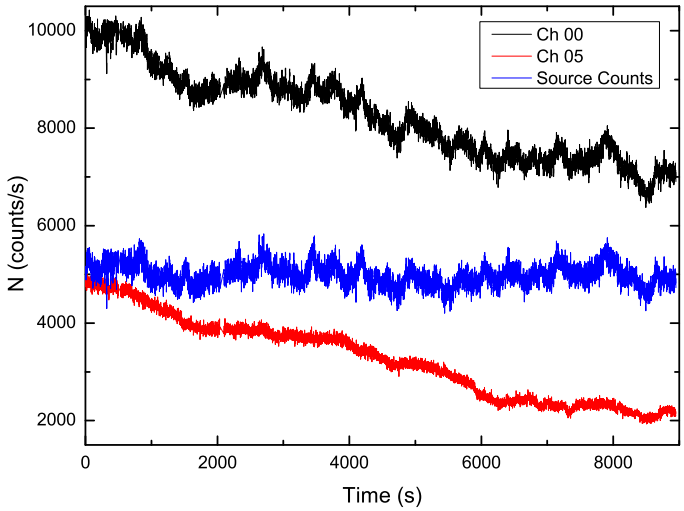

Figure 4.13. OPTIMA light curves of V2069 Cyg from July 2nd, 2009 observation (no. 1 in Table 4.4.), shown as raw, uncalibrated count-rates binned in 1 s intervals. Source count rates were obtained from the central fiber (channel 0) after subtraction of the properly calibrated sky background trace (channel 5). The sky background is decreasing in brightness because of the setting Moon

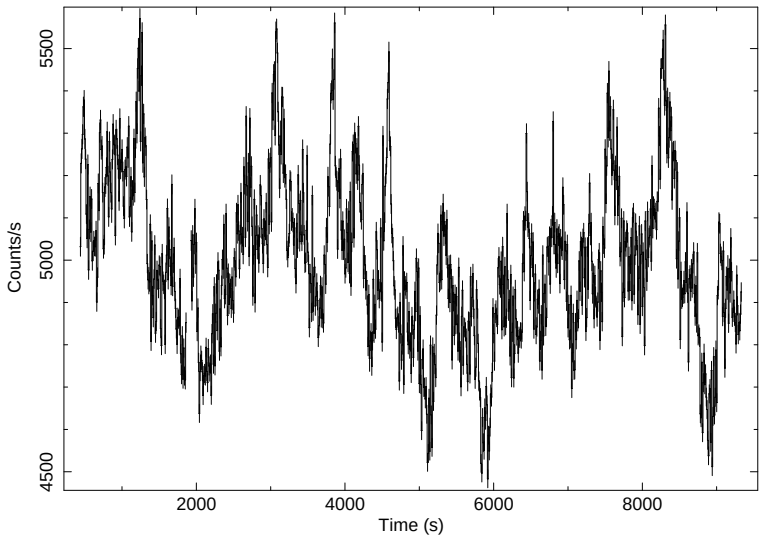

Figure 4.14. Light curve of V2069 Cyg as derived in Figure 4.10, zoomed in the count rate scale for better visibility. The optical periodicity is clearly visible. The data are background subtracted and binned into 10 s intervals. Time 0 corresponds to MJD = 55014.92172

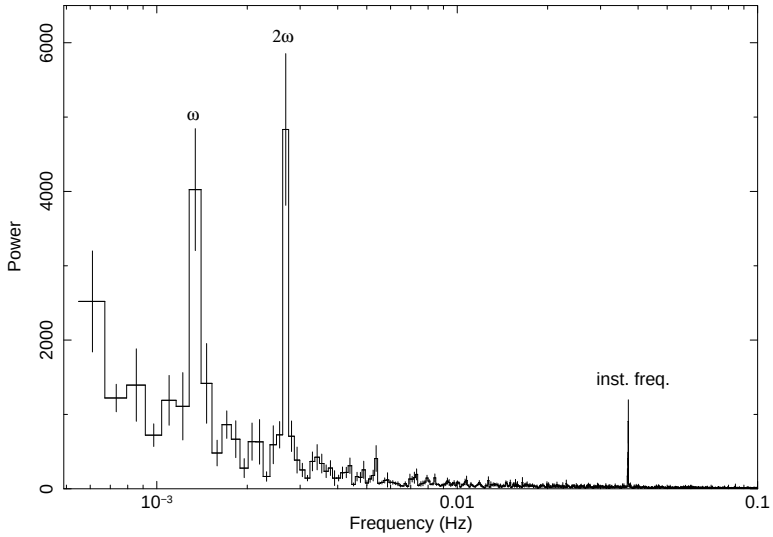

Figure 4.15. Power spectrum obtained from OPTIMA data (Table 4.4., all epochs). It shows prominent peaks at the fundamental spin frequency (first harmonic) of 0.00134277 Hz and its second harmonic of 0.00268555 Hz. An instrumental frequency at 0.0371094 Hz is also visible

uncertainties corresponds to a power of 2 (Figure 4.15.). The power spectrum shows peaks at the fundamental spin frequency (first harmonic) 0.00134277 Hz and its second harmonic 0.00268555 Hz (periods 744.73 s and 372.35 s, respectively), as well as a known systematic frequency of 0.03718 Hz (26.9 s). A χ^2 folding analysis, which folds the data over a range of periods and determines the chisquare of the folded light curve against a constant as function of the trial period, reveals the best spin period of the WD as 743.38 ± 0.25 s, Figure 4.16.

The optical light curve folded with the 743.38 s spin period shows a double-peaked profile (see Figure 4.17.) with very high duty cycle ($\sim 90\%$), that is the percentage of the rotation phase where there is a pulsed emission. Since the power spectrum of the optical data is dominated by the second harmonic of the spin frequency it is clearly seen that these two peaks are similar and separated by about half of the cycle in phase. Norton et al. (1999) reported the same result in the X-ray data of IP YY Dra, where the power spectrum is dominated by the second harmonic (i.e. $2/P_{spin}$). On the other hand, due to low statistics, we could not determine the spin period from

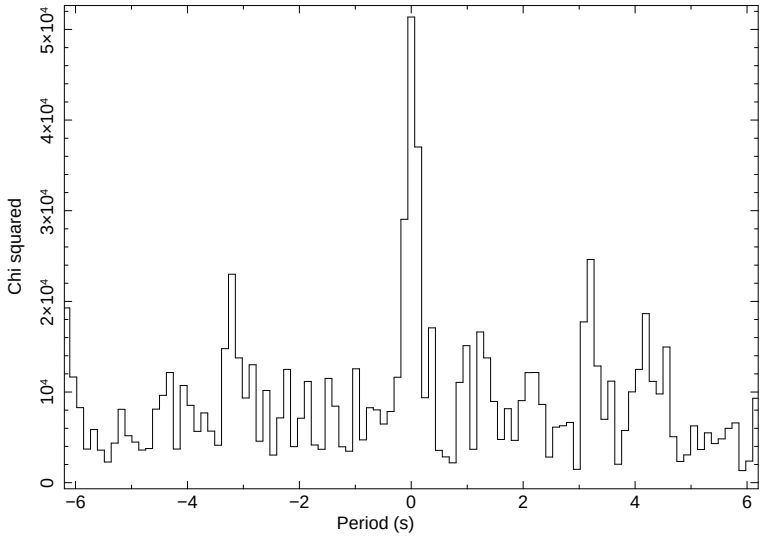

Figure 4.16. χ^2 periodogram as a function of the period, obtained from OPTIMA data. The central value (=0) corresponds to the best spin period of 743.38 s

the *Swift*-XRT data, therefore the XRT data were folded according to the optical period. The *Swift*/XRT also shows a double-peak modulation at the WD spin period of 743.38 s (see Figure 4.18.). However, the weaker peak is only marginally visible and is separated by less than half the pulse cycle.

Timing Analysis of the *XMM–Newton* Data;

For the timing analysis of the *XMM–Newton* data we corrected the event arrival times to the solar system barycenter using the *barycen* task of SAS. The background subtracted X-ray light curves in the $0.2-10.0$ keV energy band obtained from EPIC-pn and combined MOS data with a time binning of 55 s are shown in Figure 4.19. The periodic variations around 745 s can be seen clearly in the X-ray light curves. To improve the statistics for timing analysis a combined EPIC-pn, EPIC-MOS1 and EPIC-MOS2 event list from the source extraction region was created. The FFT timing analysis of the combined X-ray data revealed the presence of four harmonic frequencies with a strong peak at the fundamental frequency of 0.00134277 Hz that corresponds to a period of 744.73 s, as shown in Figure 4.20. We found that the fundamental frequency is much stronger than the second harmonic at energies above 0.5 keV, while

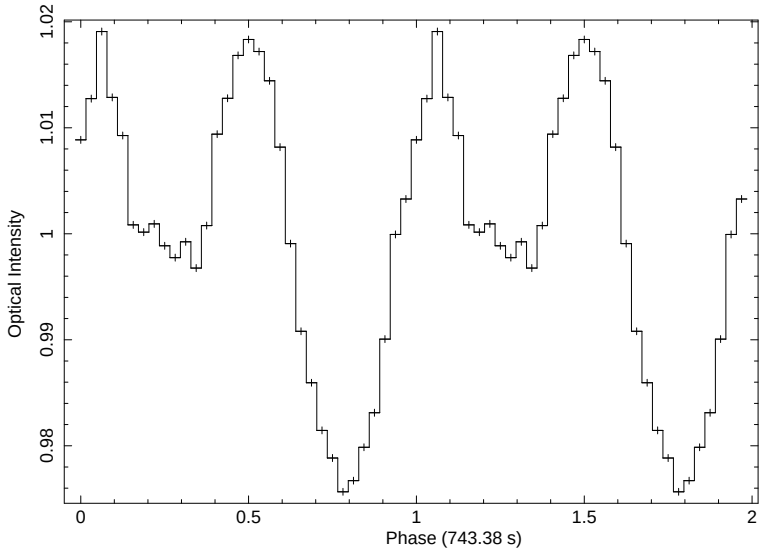

Figure 4.17. Pulse profile obtained from all OPTIMA data (Table 4.4., all epochs) folded with the 743.38 s spin cycle (32 bins/period). The profile is background subtracted and normalized to the average count rate of 4621 cts s^{-1}. Epoch, MJD = 54951.0

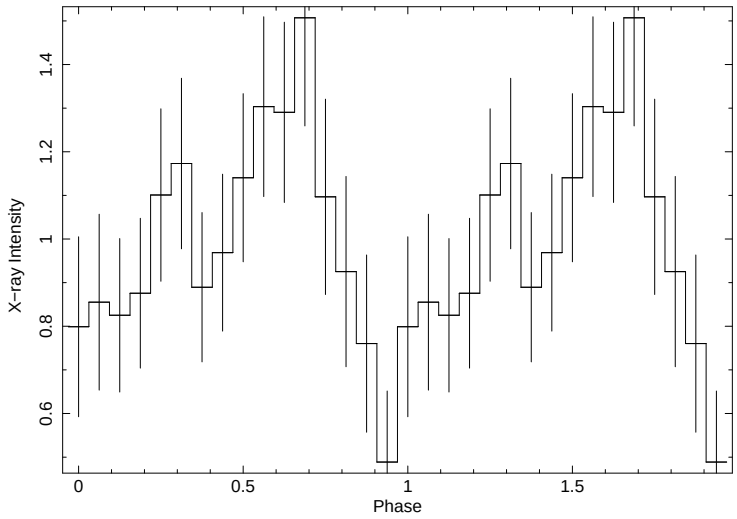

Figure 4.18. Pulse profile obtained from *Swift*-XRT data (0.3−10.0 keV) folded at 743.38 s (16 bins/period) with an arbitrary zero point (MJD = 55014.0). The profile is background subtracted and normalized to an average count rate of 0.0918 cts s^{-1}

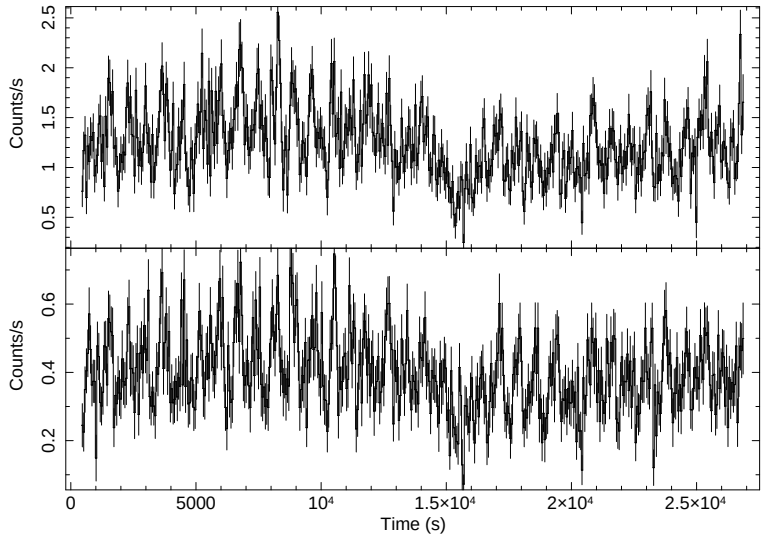

Figure 4.19. X-ray broad-band (0.2−10.0 keV) light curves of V2069 Cyg obtained from the EPIC-pn (top) and summed MOS1 and MOS2 (bottom) data. The periodic variations can be seen clearly. The data are background subtracted and binned to 55 s. Time 0 corresponds to MJD = 54951.46333

the second harmonic (with very weak power) is stronger than the fundamental frequency at energies below 0.5 keV. A similar behavior was also reported by Evans & Hellier (2004) for V405 Aur. To determine the pulse period and its error we applied the Bayesian formalism as described in Gregory & Loredo (1996). Using the combined and merged EPIC data in the 0.2−10 keV energy band reveals the spin period of the WD as 742.35 ± 0.23 s, 1σ uncertainty. We obtained the optical spin period a bit longer than the X-ray spin period, however both periods are compatible within their errors.

We folded the light curve to obtain the pulse profiles from the EPIC data (Figure 4.21.) with the spin period in the different energy bands of 0.2−1.0 keV, 1.0−2.0 keV, 2.0−4.5 keV and 4.5−10.0 keV and calculated hardness ratios (Figure 4.22.) as a function of pulse phase. The hardness ratios were derived from the pulse profiles in two neighboring standard energy bands [$HR_i=(R_{i+1}-R_i)/(R_{i+1}+R_i)$, where R_i denotes the background subtracted count rate in the energy band *i*, with *i* from 1 to 4]. The *XMM–Newton* data also show a double-peaked modulation with 742.35 s period consistent

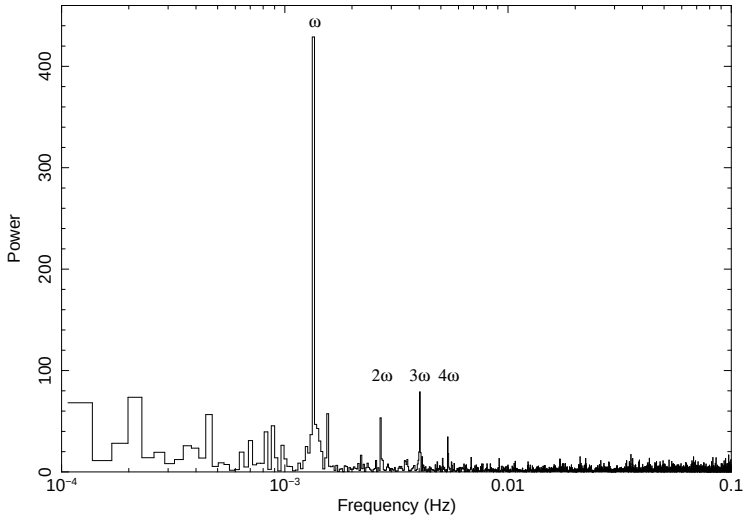

Figure 4.20. Power spectrum obtained from the combined and merged event data of EPIC-pn and EPIC-MOS (0.2−10.0 keV). It shows a strong peak at the fundamental frequency of 0.00134277 Hz which corresponds to the spin period of 744.73 s, and peaks at the second (0.00268555 Hz), third (0.00402832 Hz) and fourth (0.00537109 Hz) harmonic. The time binning of the input light curve is 1 s

with the values obtained from OPTIMA, *Swift*/XRT and *RXTE* data. The double-peaked pulse profile is more prominent at lower energies (0.2−0.7 keV), while the second peak is weaker at the higher energies (0.7−10.0 keV; see Figure 4.23.). Here the second peak is separated by less than half of the pulse cycle, and the power spectrum of the X-ray data is dominated by the fundamental spin frequency (i.e. $1/P_{\rm spin}$). A similar behavior was observed in the X-ray data of IP V709 Cas by Norton et al. (1999), where the power spectrum is dominated by the fundamental harmonic. The pulse profiles have highly asymmetrical rise and decay flanks. A dip feature is significant before the primary pulse maximum in the 0.2−1.0 keV band and centered on the primary maximum in the 1.0−2.0 keV band, while the primary maximum is more symmetric at higher energies (Figure 4.21.). A similar feature was also observed in V709 Cas (de Martino et al. 2001), in NY Lup (Haberl et al. 2002) and in UU Col (de Martino et al. 2006b). The evolution of the pulse profiles with double-peaked structure from lower energies to higher, is causing the variations in the hardness ratios. In Figure

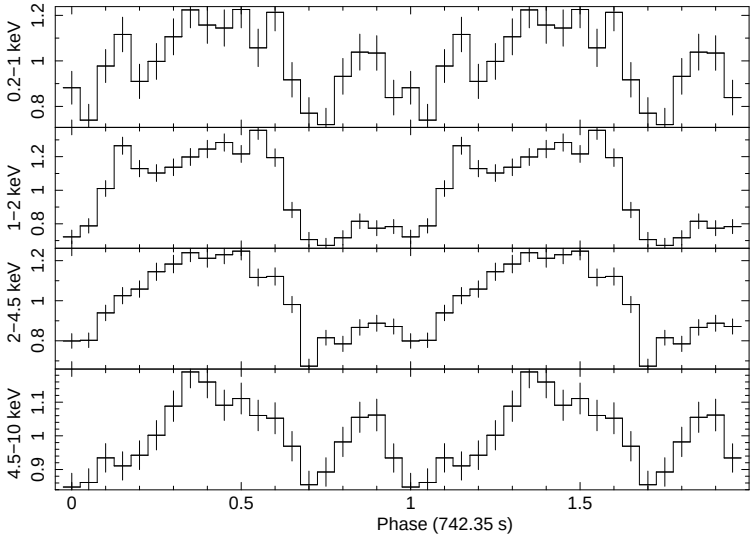

Figure 4.21. Pulse profiles obtained from EPIC binned data folded with 742.35 s spin cycle (20 bins/period) for different energy ranges: 0.2−1.0 keV, 1.0−2.0 keV, 2.0−4.5 keV and 4.5−10.0 keV from top to bottom. The intensity profiles are background subtracted and normalized to average count rates of 0.078, 0.167, 0.221, and 0.196 cts s^{-1} (from top to bottom). Epoch, MJD = 54951.0

4.22. the hardness ratios show a hardening (increase) at spin minimum and a softening (decrease) at spin maximum which is more prominent in HR3. This typical behavior is often observed from IPs and is generally produced by the larger photoelectric absorption when viewing along the accretion curtain (de Martino et al. 2001; Haberl et al. 2002). In HR2, the ratio shows two asymmetric maxima, separated by a dip centered on the primary spin maximum seen in the 1.0−2.0 keV band and a second one appearing with a toothed-shape produced by the secondary spin maximum (see Figure 4.21.). In HR1, an anti-phase behavior is observed with respect to HR2.

Orbital Phase Resolved Timing Analysis;

We investigated if the pulse shape of the rotating WD is changing with orbital phase of the binary system. The orbital phase was determined with the following ephemeris: phase (BJD) = $[T - 2451066.7837(20)]/0.311683(2)$, where, T is the observation time (Thorstensen & Taylor 2001). For this purpose we obtained the WD pulse profiles in four orbital phase ranges: 0.0−0.25, 0.25−0.5, 0.5−0.75 and

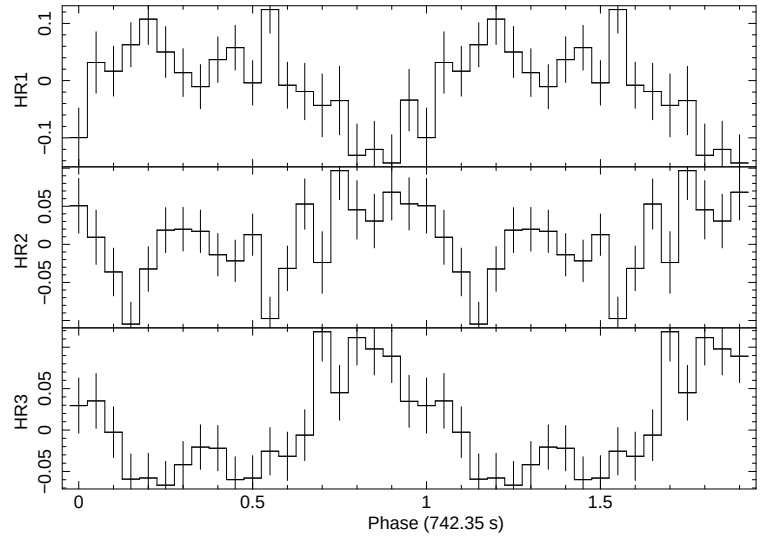

Figure 4.22. Hardness ratio as a function of phase derived from the pulse profiles (Figure 4.21.) in two neighboring standard energy bands (0.2−1.0 keV and 1.0−2.0 keV, 1.0−2.0 keV and 2.0−4.5 keV and 2.0−4.5 keV and 4.5−10.0 keV, from top to bottom)

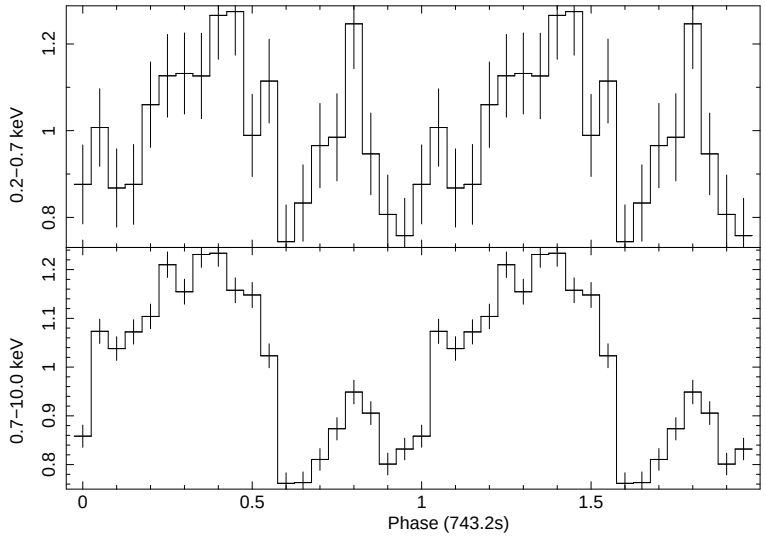

Figure 4.23. Pulse profiles folded with 742.35 s (20 bins/period) obtained from combined EPIC data (pn, MOS1 and MOS2) in the energy range 0.2−0.7 keV and 0.7−10.0 keV. Epoch, MJD = 54951.0

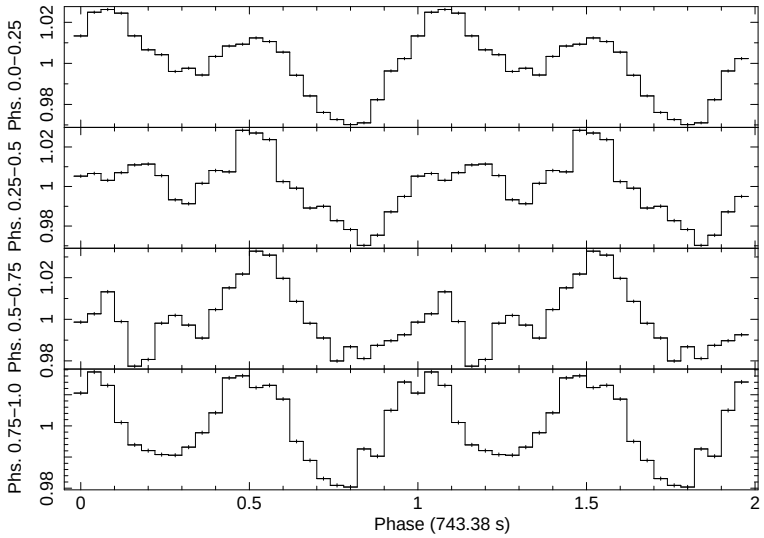

Figure 4.24. Orbital phase resolved (0.0−0.25, 0.25−0.5, 0.5−0.75 and 0.75−1.0) pulse profiles folded with 743.38 s (25 bins/period) obtained from OPTIMA data (Table 4.4. all epoch). Epoch, MJD = 54951.0

0.75−1.0. Results are shown in the Figure 4.24. and Figure 4.25. for OPTIMA and EPIC data, respectively. There is some indication of a profile change, especially in the orbital phase range 0.5−0.75, for both optical and X-ray light curves.

Spectral Analysis of the *XMM–Newton* Data;

In order to estimate the basic parameters of the emitting region, a spectral analysis of the X-ray data was performed with XSPEC v.12.5.0x (Arnaud 1996). The three EPIC spectra were fitted simultaneously with a model consisting of thermal plasma emission (MEKAL; Mewe et al. (1985)), a soft **bbody** component (as suggested by de Martino et al. 2009) and **gaussian**, absorbed by a simple photoelectric absorber (*phabs*) and a partially-covering photoelectric absorber (**pcfabs**). **phabs** and **pcfabs** are used to correct the absorption along the line of sight and inside the system by the accretion curtain/stream, respectively (Staude et al. 2008). To account for cross-calibration uncertainties a constant factor was introduced. The composite model which used to fit the EPIC spectra is:

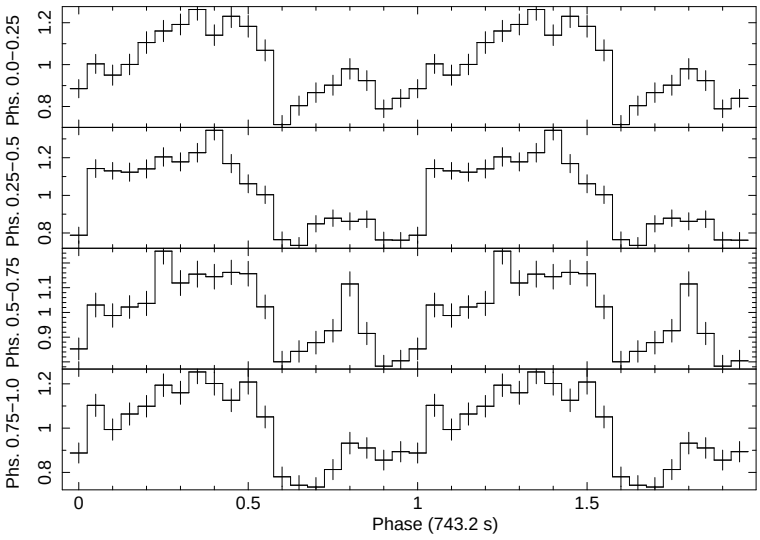

Figure 4.25. Orbital phase resolved (0.0−0.25, 0.25−0.5, 0.5−0.75 and 0.75−1.0) pulse profiles folded with 742.35 s (16 bins/period) obtained from combined EPIC data (pn, MOS1 and MOS2). Epoch, MJD = 54951.0

$$(phabs * pcfabs * (mekal + bbody + gaussian) * constant)^{8} \tag{4.21}$$

Here, **phabs** is the simple photoelectric absorbers, describes the absorptions of the interstellar medium along the line of sight which can be defined as:

$$M(E) = \exp(-N_H \sigma(E)) \tag{4.22}$$

where, $\sigma(E)$ is the photo-electric cross-section and N_H is the equivalent hydrogen column (in units of 10^{22} atoms/cm^2).

The **pcfabs** is the partially-covering photoelectric absorbers (mainly responsible for the absorption of soft photons in the mekal component), describes the absorptions of the circumstellar crossing the line of sight, which is caused by the accretion

[8] http://heasarc.gsfc.nasa.gov/xanadu/xspec/manual/Toc.html

curtain/stream inside the system (Evans & Hellier 2007; Staude et al. 2008). pcfabs can be defined as:

$$M(E) = f\exp(-N_H\sigma(E)) + (1-f) \tag{4.23}$$

where, f is the covering fraction (0< f <=1).

The **MEKAL** component (developed by Rolf **ME**WE, Jelle **KA**ASTRA and Duane **L**iedahl, (Kaastra & Mewe 2000)) produces an emission spectrum (describing the emitted hard component) from hot diffuse gas (post-shock material) above the WD's surface (Staude et al. 2008) and includes line emissions from various elements. The MEKAL outputs are: kT is the plasma temperature in keV; n_H is the hydrogen density in cm^{-3} and other metal abundances with changing subscript (like C, N, O, Ne, Na, Mg, Al, Si, S, Ar, Ca, Fe, Ni). The normalization of the MEKAL is defined as:

$$norm = (10^{-14}/(4\pi(D_A(1+z))^2))\int n_e n_H dV, \tag{4.24}$$

where, D_A is the angular diameter distance to the source (cm), n_e and n_H are the electron and H densities (cm^{-3}) respectively. z is the (fixed) redshift.

The **Gaussian** (Equation (4.21)) component represents the iron (Fe) K fluorescent emission line at 6.4 keV which is often seen from classical IPs and generally interpreted as the reprocessing of X-rays. The corresponding formula for the gaussian line is:

$$A(E) = K(1/\sigma\sqrt{(2\pi)})\exp(-0.5((E-E_l)/2\sigma^2) \tag{4.25}$$

where, E_l is the line energy in keV; σ is the line width in keV and the norm 'K' is total photons/cm^2s^{-1} in the line.

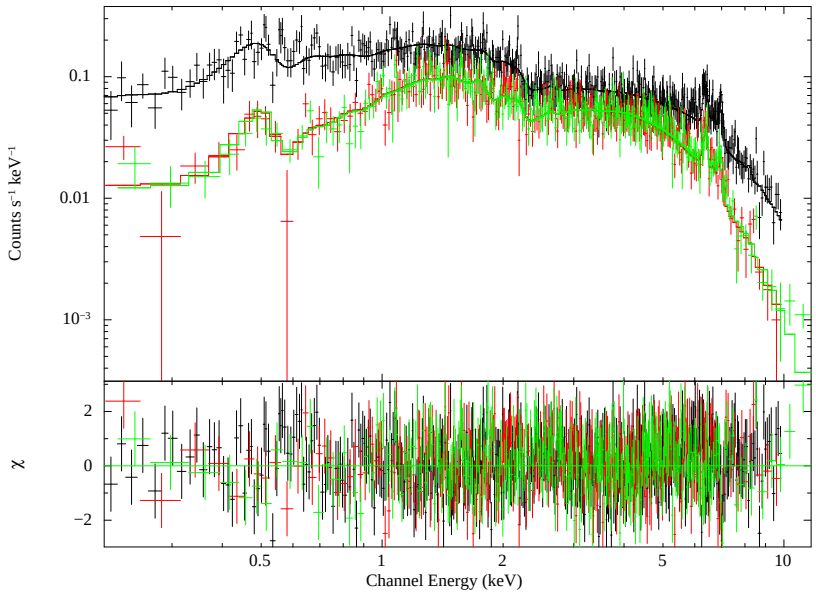

Figure 4.26. The composite model (phabs*pcfabs* (mekal + bbody + gaussian)*constant) fitted to the spectrum of the EPIC-pn (black) and MOS (green and red) data in the 0.2−10 keV energy band. The bottom panel shows the residuals

The **bbody** (blackbody) component describes the soft X-ray emission in the observed spectrum. In IPs the soft X-ray blackbody emission believed to arise from WD surface, heated by reprocessing of the hard X-rays from the accretion column (Evans & Hellier 2007). The bbody component can be defined as:

$$A(E) = K \times 8.0525 E^2 dE/(kT)^4(\exp(E/kT)-1)) \tag{4.26}$$

where, kT is temperature in keV, K is norm (where, L_{39}/D_{10}^2, L_{39} is the source luminosity in units of 10^{39} ergs/s and D_{10} is the distance to the source in units of 10 kpc). And, **Constant** is an energy-independent multiplicative factor.

In a first fit to the spectra, the plasma temperature for the MEKAL component could not be constrained. Therefore, we fixed the plasma temperature at 20 keV, a value typical for IPs (Staude et al. 2008). We obtained a best fit with reduced χ_r^2 of 1.002 (χ^2 of 1014.69 with 1013 degrees of freedom). The spectral parameters for the

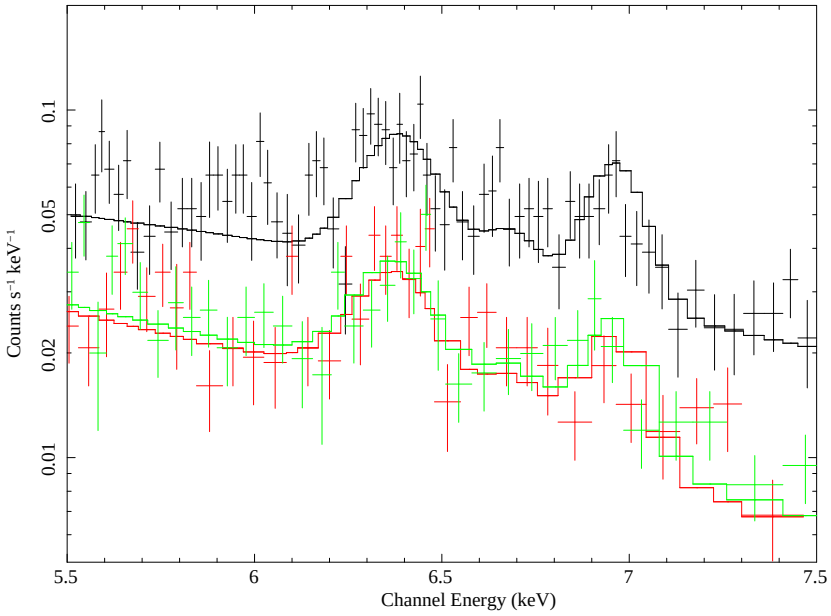

Figure 4.27. Enlarged part of Figure 4.26. showing the Fe line complex in the EPIC spectra

fit are summarized in Table 4.5. and the spectra including the best fit model is shown in Figure 4.26.

We determined the hydrogen column density as $N_{\rm H} = 3.84 \times 10^{21}$ cm^{-2}. This is higher (by an order of magnitude) than the total Galactic hydrogen column density (3.79×10^{20} cm^{-2}, an interpolated value from Dickey & Lockman (1990) that was calculated using the HEASARC N_H web interface[9]) in the direction of the source. Our result is comparable to the value (5×10^{21} cm^{-2}) obtained by de Martino et al. (2009). For the partial absorber (pcfabs) we find, $N_{\rm H} = 8.29 \times 10^{22}$ cm^{-2} with a covering fraction of 0.65. Similar values were derived for V2069 Cyg (de Martino et al. 2009) and the other soft IPs observed with *XMM–Newton* (see Table 4.6.). The absorbed flux of V2069 Cyg in the 0.2−10.0 keV energy band (derived for EPIC-pn) is 7.93×10^{-12} ergs cm^{-2}s^{-1} which corresponds to a source intrinsic flux (with absorption set to 0) of 2.64×10^{-11} ergs cm^{-2}s^{-1} (EPIC-MOS values are 2 per cent higher corresponding to the constant factors derived from the fit). The spectra around the

[9] http://heasarc.nasa.gov/cgi-bin/Tools/w3nh/w3nh.pl

Table 4.5. Spectral fit result for the *XMM–Newton* EPIC data

Model	Parameter	Unit	Value	error
phabs	N_H	10^{21} cm $^{-2}$	3.84	(-0.04, +0.05)
pcfabs	N_H	10^{22} cm $^{-2}$	8.29	(-1, +1.2)
	CvrFract		0.65	$\pm$0.02
mekal	kT	keV	20.0	frozen
	n_H	cm^{-3}	1.0	frozen
	Abundance		1.0	frozen
	norm		6.29×10^{-3}	$(-2.4, +2.6)\times10^{-4}$
bbody	kT	keV	7.68×10^{-2}	$(-4.3, +4.2)\times10^{-3}$
	norm		2.18×10^{-4}	$(-0.75, +1.2)\times10^{-4}$
gaussian	LineE	keV	6.385	$\pm$0.017
	Sigma	eV	51	(-32, +27)
	norm		2.6×10^{-5}	$(-5.4, +3.9)\times10^{-6}$
constant factor	pn		1.0	frozen
	MOS1		1.026	$\pm$0.018
	MOS2		1.028	$\pm$0.018

Table 4.6. The parameters of the partial absorber (pcfabs) obtained for V2069 Cyg and some soft IPs observed with *XMM–Newton*

Source	$N_{\rm H}(cm^{-2})$	CvrFract	Reference[a]
V2069 Cyg	11×10^{22}	0.69	1
MU Cam	7.9×10^{22}	0.61	2
PQ Gem	11.1×10^{22}	0.45	3
UU Col	10×10^{22}	0.51	4
V405 Aur	6.1×10^{22}	0.52	5
NY Lup	9.7×10^{22}	0.47	6

[a]References: (1) de Martino et al. (2009); (2) Staude et al. (2008); (3) Evans et al. (2006); (4) de Martino et al. (2006b); (5) Evans & Hellier (2004); (6) Haberl et al. (2002)

Fe-K emission line complex are shown enlarged in Figure 4.27. The iron fluorescence and FeXXVI lines are clearly resolved in the EPIC spectra. The FeXXVI line energy identified from the XSPEC possible lines list is $\sim$6.95 keV and the fluorescence line energy derived from the fit is $\sim$6.385 $\pm$0.017 keV. The EW of the fluorescent line is 243 eV.

5. DISCUSSION and CONCLUSION

5.1. Discussion

In this part, we present the discussion of the results of the two mCVs, HU Aqrii and V2069 Cygni (RX J2123.7+4217), and an overall conclusion of the thesis.

5.1.1. HU Aquarii

Recently, the HU Aqr system has received much attention in the literature. Schwarz et al. (2009) carried out an analysis of the orbital ephemeris and derived mid-egress times of the system. They detected (O−C) variability which is explained by the presence of a planatery companion in the system orbit. Shortly after this work, Qian et al. (2011) presented and discussed 10 new light curves in the optical wavelength. They explained the deviations of the observed midegress times with a linear and quadratic ephemeris, concluding that the variations in (O−C) diagram may be explained by the Light Travel Time (LTT) due to two jovian-mass planetary companions orbiting the system at a distance of few AU. After a few months of this work, Wittenmyer et al. (2012) and Hinsen et al. (2012) re-analysed data in Qian et al. (2011) together with the existing data in the literature and found also a 2-planet configuration in the system orbit.

The ephemeris models presented in Section 4.2.3 are characterized by the presence of large deviations from simple linear and quadratic descriptions of the orbital timing (Nasiroglu et al. 2010). The overall amplitude of the residuals spans about 30-40 s and thus comparable to the diameter of the white dwarf moving at a speed of about 200 km/s. Explanations for the timing deviations in terms of shifting the light emitting polar spot on the surface of the WD are therefore unlikely. We then fitted the residuals in sequence with two sinusoidal variations, and find a long period one over 11−15 yr and an amplitude between 10−13 s, and a short period oscillation over about 6 yr and 6−7 s amplitude. We realize that the sequential fits can only be a preliminary

result. A complete simultaneous fit with two periodic functions together with the linear/quadratic ephemeris will be needed to describe the data correctly. Explanations purely intrinsic to the binary system in terms of *(i)* cyclic movement of the accretion spot on the WD surface due to changes in the accretion flow or *(ii)* due to orbital period changes caused by a regular stellar activity cycle of the secondary star have been discussed by Schwope et al. (2001) and Schwarz et al. (2009) but were not fully convincing to reconcile with the data. The sinusoidal variations and the presence of two different periods seems to hint strongly at an explanation in terms of changes in the light travel time (LTT) due to the presence of smaller 'planetary' bodies orbiting the compact binary at large distances. The latest system parameters of the HU Aqr binary were derived by Vogel et al. (2008) and we followed the arguments presented by Qian et al. (2010) for the system of DP Leo, to derive the properties of potential planets around HU Aqr. We assumed that the compact binary and its 'outer' satellites move in co−planar orbits (inclination 85.5°,Vogel et al. (2008)). We tentatively suggested that there might be two planets, one with a mass of 4.42 (±0.28) $M_{Jupiter}$ (the mass function $f(m) = 6.19(\pm 1.5) \times 10^{-8}$) at a distance of 5.1 (±0.07) A.U in a 11 (±0.2) yr orbit, and another with a mass of 4.05 (±0.2) $M_{Jupiter}$ ($f(m) = 4.77(\pm 0.7) \times 10^{-8}$) at distance of 3.4 (±0.02) A.U in a 6.0 (±0.03) yr orbit.

In a very recent paper (Gozdziewski & Nasiroglu et al. 2012), we developed a Keplerian, kinematic model of LTT signal in the three-body configuration and re-analyse the data set published in the literature, following the 2-planet hypothesis by Qian et al. (2011) and further investigated by Wittenmyer et al. (2012). Using a new formulation of the LTT of the (O−C) to the available data of the HU Aqr system, we found that the 2-planet hypothesis by Qian et al. (2011) is not likely. We used the new set of precision OPTIMA mid-egress measurements, as well as observations performed at PIRATE, TCS and MONET/N telescopes and we re-analysed planetary models to the whole set of data (in total 171 measurements) up to November 18th, 2011 (see Section 4.2.1). We fitted the data with the linear and quadratic ephemeris models which are given in Equations (5.1) and (5.2), respectively.

$$(O-C) = T_{ep}(l) - t_0 - lP_{bin} = \tau(t_l, K_{1,2}, P_{1,2}, e_{1,2}, \omega_{1,2}, T_{1,2}) \tag{5.1}$$

$$(O-C) = T_{ep}(l) - t_0 - lP_{bin} - \beta l^2 = \tau(t_l, K_{1,2}, P_{1,2}, e_{1,2}, \omega_{1,2}, T_{1,2}) \tag{5.2}$$

$$K_1 = (\frac{1}{c})\frac{m_1}{m_1+m_*} a_1 sin\ i_1, \qquad \beta = \frac{1}{2} P_{bin}\dot{P}_{bin},$$

$$K_2 = (\frac{1}{c})\frac{m_1}{m_1+m_2+m_*} a_2 sin\ i_2, \tag{5.3}$$

where, $l(l = 0, ..., N)$ is the eclipse cycle number, t_l is the date of the eclipse time-mark, t_0 is the reference epoch ($l = 0$), P_{bin} is the orbital period of the binary, m is the masses of the compact binary, m_1 and m_2 are the masses of two planets. Two tuples $(a_i, e_i, i_i, \omega_i, T_i, P_i)$ i= 1, 2, which consist of the semi major axis, eccentricity, inclination, argument of pericentre, the time of pericentre passage, and the orbital period of a given object, respectively, are for the geometric Keplerian elements. K_1 and K_2 are the semi amplitude factors. β is the describe the binary period damping (change) due to the mass transfer, magnetic braking, gravitational radiation, and/or influence of a very distant companion and τ is the binary contribution (for more detail see Gozdziewski & Nasiroglu et al. (2012)).

First, we tested the one-planet hypothesis. For the linear ephemeris model, the one-planet solution is characterized by extreme eccentricity and displays large residuals and a strong trend present in the (O−C) diagram as in Figure 5.1. A more general 1-planet LTT model with quadratic ephemeris to all available data (171 measurements) are shown in Figure 5.2. This model fits the data very well in a large part of the time-window between l = 25000 and l = 80000. But, over approximately one fourth of the time-window from l = 0 to l = 25, 000, the data fit the synthetic curve rather poorly. Results of this analysis show that the recent observations by Qian et al. (2011) appear

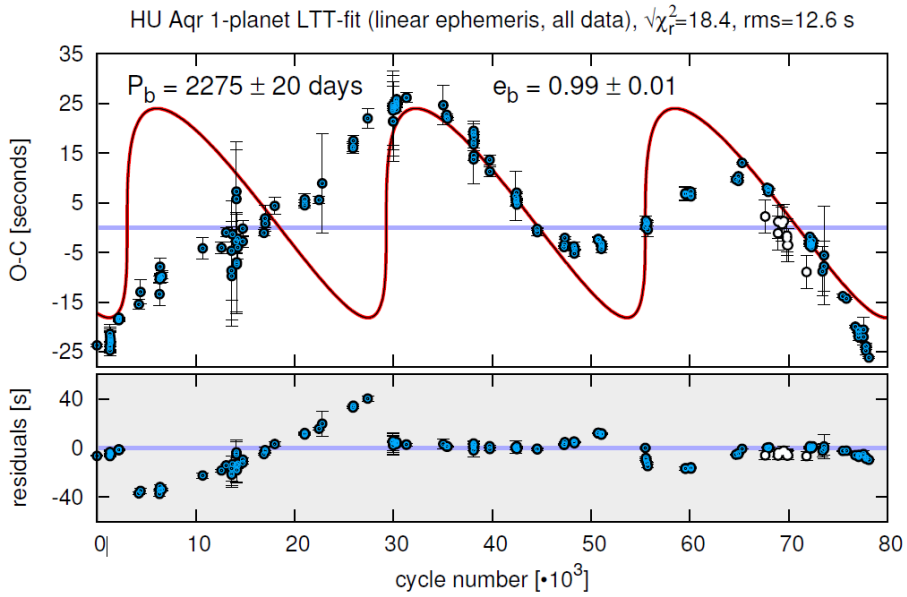

Figure 5.1. Synthetic curve of the 1-planet LTT model with linear ephemeris to all available data, including the very recent egress times collected by the OPTIMA photometer, as well as PIRATE, TCS and MONET/N telescopes. Open circles are for measurements in Qian et al. (2011). [Taken from Gozdziewski & Nasiroglu et al. (2012)]

to be outliers to our 1-planet solution, as the mid-egress times are shifted by about of 3−10 s with respect to the synthetic curve. Because these observations overlap in the time window with much more precise OPTIMA data, that discrepancy between these two data sets cannot be avoided.

In an effort to explain the strange behaviour of the residuals, we realized, as it was discussed already, that (1) the available observations come from different telescopes/instrumentation, and to make the matter worse, (2) the egress times are measured on the basis of light curves in different spectral windows. In particular, the first part of the data set contains the egress times derived from X-rays (ROSAT and XMM) and ultraviolet (EUVE, XMM OM-UVM2 and HST/FOS) light curves, and some eclipses were observed with OPTIMA in polarimetric mode. To remove the possible inconsistency due to the different spectral windows and filters, we considered data sets consisting of the egress times measured only in the optical range (white light and the V band). The results are shown in Figure 5.3. for the optical data without X-ray

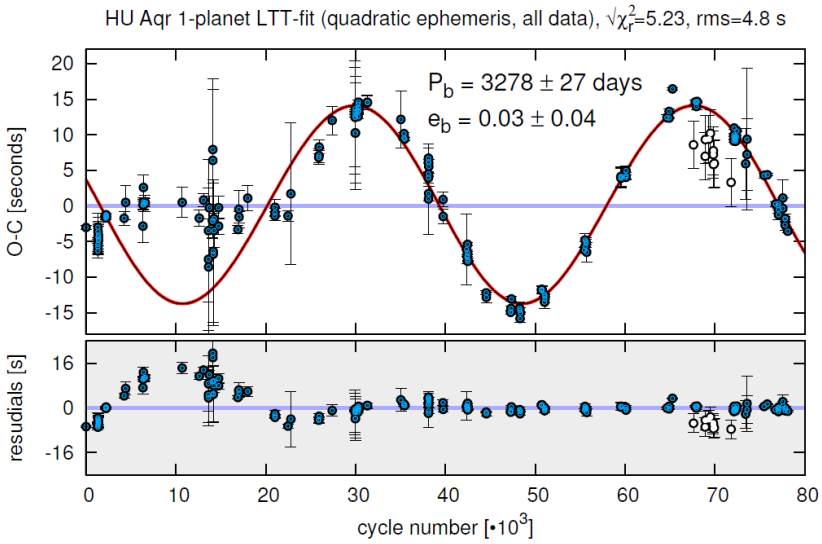

Figure 5.2. Synthetic curve of the 1-planet LTT model with quadratic ephemeris to all available data, gathered in this work, including the very recent midegress times collected by the OPTIMA photometer, as well as PIRATE, TCS and MONET/N telescopes with orbital parameters given in Table 5.1. (Fit I). The white filled circles mark the Qian et al. (2011) measurements. [Taken from Gozdziewski & Nasiroglu et al. (2012)]

and UV, but including polarimetric measurements (note that the polarimetry was done in the white-light band). As can be seen from Figure 5.3. the 'damping' effect has almost vanished, suggesting that it could have appeared due to the presence of X-ray and UV-derived eclipses.

Still, there is a group of data points with large errors, around l∼14000, which do not fit well to the clear quasi-sinusoidal variation of the (O−C). The deviations of these points may be explained by poor time-resolution (∼12 s of the AIP07 CCD camera), that has been used to observe the HU Aqr eclipses (Schwope et al. 2001). Let us also note that the Qian et al. (2011) data points are again systematically outliers with respect to the synthetic signal. After removing these data and all points (seven measurements) in the polarimetric mode, we obtained a homogeneous optical data set to which we fitted the quadratic ephemeris 1-planet model again. The synthetic curve of this fit with data points over-plotted is shown in Figure 5.4. Parameters of this fit are presented in Table 5.1. as the final solution Fit II and are well constrained by the

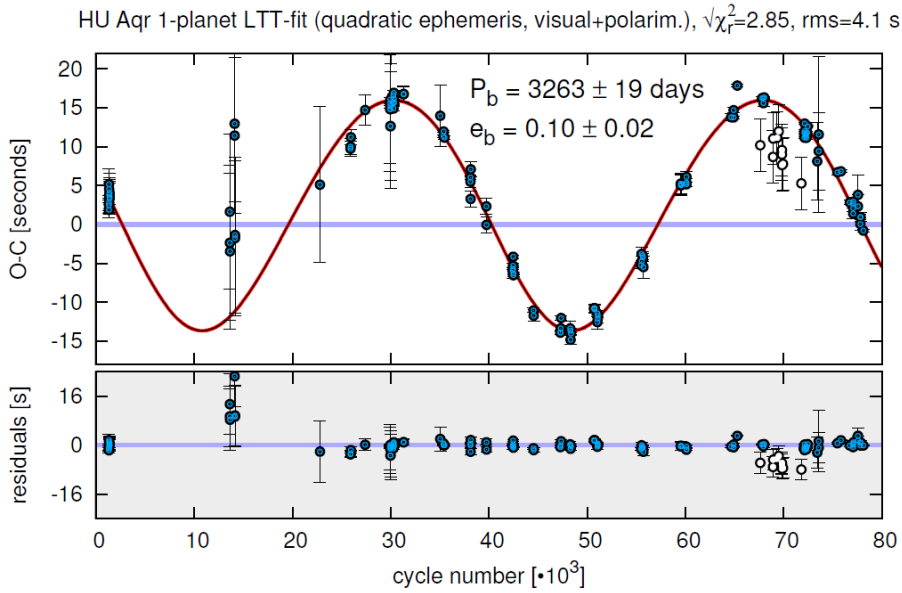

Figure 5.3. Synthetic curve of the 1-planet LTT model with quadratic ephemeris to white light and visual band (V) data, including polarimetric observations by OPTIMA (i.e., the UV- and X-band observations are excluded). The white filled circles mark the Qian et al. (2011) measurements. [Taken from Gozdziewski & Nasiroglu et al. (2012)]

observations.

The best-fit model seem to constrain the damping factor $\beta \sim -3 \times 10^{-13}$ day/cycle^2 very well. Such a value is close to estimates in the literature, e.g., $\sim -5 \times 10^{-13}$ day/cycle^2 by Schwarz et al. (2009) and $\sim -2.5 \times 10^{-13}$ day/cycle^2 by Qian et al. (2011). It is still larger by more than one order of magnitude to be explained by gravitational radiation, but remains in the range of magnetic braking (Schwarz et al. 2009).

The results of these models show that the 1-planet solution is relatively well constrained by available optical observations selected as a homogeneous data set. Because the early optical data (the white light and V-band measurements) are coherent with an impressive, very clear quasi sinusoidal signal exhibited by superior-precision OPTIMA measurements, as well as with the recent MONET/N, PIRATE and WFC data, a single-companion hypothesis seems well justified. The observed (O−C) variations may be consistently explained by the presence of only one circumbinary planet

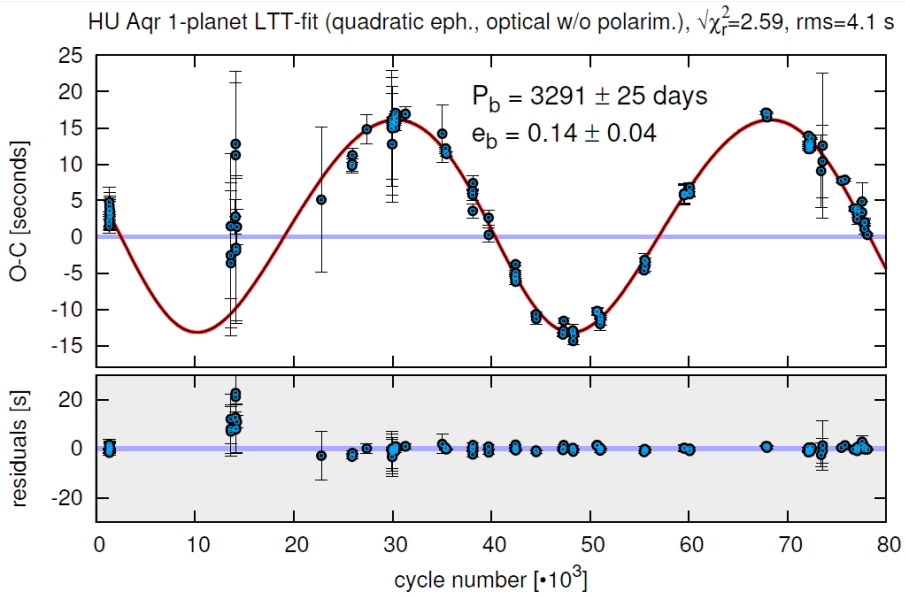

Figure 5.4. Synthetic curve of the 1-planet LTT model with quadratic ephemeris to observations in white light + V band without measurements in Qian et al. (2011) and polarimetric data. Orbital parameters of this solution are given in the Table 5.1. (Fit II). [Taken from Gozdziewski & Nasiroglu et al. (2012)]

of the minimal mass of $\sim$7 $M_{Jupiter}$, in an orbit with a small eccentricity of $\sim$0.1 at a distance of $\sim$4.5 AU and an orbital period of $\sim$10 yr, similar to Jupiter in the Solar System. Our results support the original 1-planet hypothesis by Schwarz et al. (2009) rather than the 2-planet model proposed by Qian et al. (2011). Besides the disagreement between our conclusions and the previous works, our results suggest that the kinematic modeling of 2-planet configurations is not fully justified on the grounds of the dynamics because the best-fit models may imply large masses (up to stellar range), large eccentricities, and similar orbital periods indicating a possibility of strong mean motion resonances. Moreover, the (O−C) variability that suggests 2-planet solutions most likely appears due to mixing observations done in different spectral windows.

5.1.2. V2069 Cygni

We have presented the optical and X-ray observations of the IP V2069 Cyg obtained by OPTIMA, *Swift*-XRT and *XMM–Newton*/EPIC, respectively. The timing

Table 5.1. Keplerian parameters for the 1-planet LTT fit model with quadratic ephemeris to all data gathered in this work (Fit I) and to measurements selected in the optical and V-band domain (Fit II). Synthetic curves with mid-egress times overplotted are shown in Figure 5.3. and Figure 5.4. Numbers in parentheses represent the uncertainty at the last significant digit. Total mass of the binary is 0.98 $M_{\odot}$ (Schwope et al. 2011). [Taken from (Gozdziewski & Nasiroglu et al. 2012)]

Model parameter	Fit I all measurements	Fit II optical measurements
K_b [seconds]	13.9± 0.3	14.7 ±0.2
P_b [days]	3278 ± 28	3287 ±19
e_b	0.03 ±0.04	0.13 ± 0.04
ω_b [degrees]	[degrees] 211 ± 40	226 ± 10
T_b [BJD 2,440,000+]	6233 ±360	6361 ±102
P_{bin} [days]	0.0868204226(5)	0.0868204259(4)
T_0 [BJD 2,440,000+]	9102.92004(2)	9102.91994(1)
β [$\times 10^{-13}$ day cycle^{-2}]	-2.61(5)	-2.95(4)
a_b [au]	4.29	4.30
m_b sin i [M_{Jup}]	6.71	7.10
N data	171	115
$(\chi^2_v)^{1/2}$	5.23	2.48
rms [seconds]	4.8	3.7

analysis of the optical data reveal pulsations at periods of 743.38 ± 0.25 s and X-ray data 742.35 ± 0.23 s, representing the spin period of the WD. We have found that the second harmonic is much stronger than the fundamental in the power spectrum obtained from the optical data. Furthermore, the fundamental frequency from XMM data is weak or even absent at energies < 0.5 keV, while it is stronger at > 0.5 keV, compared to the second harmonic. IP V405 Aur has shown very similar behaviour in the *XMM–Newton* data (Evans & Hellier 2004). The double-peaked pulsations at the spin period are clearly observed in the optical and X-ray data ($0.2-10$ keV). The folded light curves show a more prominent double-peaked pulse profile when the power spectrum is dominated by the second harmonic. When the second harmonic is weak the curve possesses a similar profile but with a weaker second peak (Figure 4.23.). The peak separation is around 0.5 for the optical data (Figure 4.17.), and less than 0.5 for the X-ray data (Figure 4.23.). Therefore, the power spectrum of the optical data is dominated by the second harmonic, while the X-ray data is the fundamental.

IP systems (assuming equilibrium rotation) with a short spin period will have

relatively small magnetospheres, corresponding to the shorter Keplerian periods in the inner accretion disk. In such short period systems the WD is therefore expected to have a weak magnetic field. The magnetic forces of the WD pick up the material from the accretion disk approximately at the co-rotation radius. The material attaches to the field lines and is channelled onto the WD magnetic poles, where it undergoes a strong shock. After that it is settling on the surface and cooling by the emissions of X-ray bremsstrahlung and optical/infrared cyclotron (Rosen et al. 1988; Norton et al. 2004a). As proposed by Evans & Hellier (2004) the prominent double-peaked modulation in the soft X-ray emission is most likely due to the changing viewing geometry onto the accreting polar caps. We view the heated surface of the WD most favourably when one of the poles points towards us. Nevertheless, due to the highly inclined dipole axis, the external regions of the accretion curtains will not quite cross the line of sight, therefore the hard X-ray emission exhibits a double-peaked pulse profiles with a weaker secondary peak. However, the intensity of the pulse profiles could be also affected by the opacity resulting in electron scattering and absorption in the highly ionized post-shock region, or an offset of the magnetic axis from the WD center (Allan et al. 1996; Norton et al. 1999; Evans & Hellier 2004).

The pulse profiles of the optical and X-ray data (each folded with both 742.35 s and 743.38 s spin period and with a same reference time) are out of phase. As an example we show these profiles folded with 743.38 s in Figure 5.5. de Martino et al. (2009) also reported that the X-ray pulses (from EPIC-pn) are anti-phased with the optical pulses (in the B-band from optical monitor on the XMM-Newton). X-ray and optical/infrared photons in some IPs originate from two different regions. The X-ray photons are thought to originate from the surface of the WD, whereas the optical/infrared photons are thought to originate in the X-ray heated magnetic polar caps (or X-ray irradiated surface of the companion star), and possibly in the accretion stream (Eracleous et al. 1994; Israel et al. 2003; Revnivtsev et al. 2010). Norton et al. (2004b) suggested that one of the magnetic poles heated by the accretion flow will leave behind a heated trail on the WD surface which will emit optical/infrared photons. During the emission some part of the optical/infrared photons will be absorbed by the flow while the

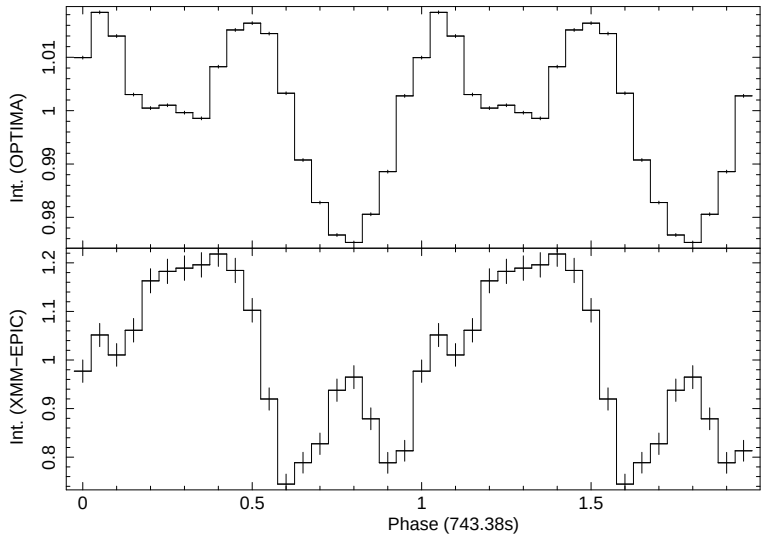

Figure 5.5. Pulse profiles folded with 743.38 s (20 bins/period) obtained from combined XMM EPIC 0.2−10 keV data and OPTIMA data. Epoch, MJD = 54951.0

accretion flow is heating the second pole. At that time the rest of the optical/infrared modulations will be seen which is shifted with respect to the X-rays. The phase shift observed between the optical and X-ray pulse profiles in V2069 Cyg is most probably caused by this X-ray heated mechanism.

On the other hand, Norton et al. (1999) suggested that IPs which show a single-peaked pulse profile resulting from stream-fed (or disk-overflow) accretion are an indicator of a WD with a relatively strong magnetic field. These IPs with long WD spin periods (longer than 700 s) might show X-ray beat periods ($1/P_{\rm beat}=1/P_{\rm spin}-1/P_{\rm orb}$) at some time in their lives (FO Aqr, TX Col, BG CMi, AO Psc, V1223 Sgr and RX J1712.6-2414). Conversely, IPs with short WD spin periods (shorter than 550 s) have shown double-peaked pulse profiles and must therefore have weak magnetic fields. These short period systems did not exhibit X-ray beat periods (AE Aqr, DQ Her, XY Ari, V709 Cas, GK Per, YY Dra and V405 Aur). In the power spectrum of V2069 Cyg we have not found any specific signal at the beat frequency. This absence indicates that in these short period IPs and V2069 Cyg accretion does not occur in a stream-fed or disk-overflow scenario (Norton et al. 1999).

Table 5.2. 39 IPs with known spin and orbital periods

Name	P_{orb} (h)	P_{spin} (s)	P_{spin} / P_{orb}	Properties [a]	Period References [b]
0.01 < P_{spin} / P_{orb} ≤ 0.1	*and P_{orb} > 3 h*				
V709 Cas	5.341	312.780	0.01627	DP	33,41
NY Lup	9.870	693.010	0.01950	SXR	2, 21, 17, 41
RXS J213344.1+510725	7.193	570.800	0.02204	SXR	2, 11, 42
Swift J0732.5-1331	5.604	512.420	0.02540	-	5, 41
V2069 Cyg	7.480	743.384	0.02756	SXR, DP	18, 41
RXS J070407.9-262501	4.380	480.670	0.03205	SXR	2, 22,44
El Uma	6.430	741.660	0.03204	-	3
V405 Aur	4.160	545.456	0.03642	SXR, DP	2, 20, 23, 41
YY Dra	3.969	529.310	0.03705	DP	24, 33
IGR J15094-6649	5.890	809.700	0.03819	-	12, 41
IGR J00234+6141	4.033	563.500	0.03881	-	6
RXS J165443.5-191620	3.700	546.000	0.04099	-	40
IGR J16500-3307	3.617	579.920	0.04454	-	36, 41
PQ Gem	5.190	833.400	0.04461	SXR	2, 19, 21, 27, 41
V1223 Sgr	3.366	745.630	0.06153	-	11, 41
AO Psc	3.591	805.200	0.06229	-	11, 41
UU Col	3.450	863.500	0.06952	SXR	2, 9, 21, 43
MU Cam	4.719	1187.250	0.06989	SXR	2,38, 41
FO Aqr	4.850	1254.400	0.07184	-	11, 16, 41
V2400 Oph	3.430	927.660	0.07513	SXR, Diskless	2, 8, 21, 26
WX Pyx	5.540	1557.300	0.07808	SXR	2, 21,39
BG Cmi	3.230	913.000	0.07852	-	4, 41
IGR J17195-4100	4.005	1139.500	0.07902	-	36, 41
TX Col	5.718	1910.000	0.09284	-	41
V2306 Cyg	4.350	1466.600	0.09365	-	11, 34
RXS J180340.0-401214	4.402	1520.510	0.09595	SXR	2, 22
TV Col	5.486	1911.000	0.09676	-	41
V1062 Tau	9.982	3726.000	0.10368	-	30, 42
P_{spin} / P_{orb} ≥ 0.1	*and P_{orb} < 2 h*				
HT Cam	1.433	515.0592	0.09984	-	31
V1025 Cen	1.410	2147.000	0.42297	-	29, 37
DW Cnc	1.435	2314.660	0.44806	-	35
SDSS J233325.92+152222.1	1.385	2500.000	0.50127	-	25
EX Hya	1.637	4021.000	0.68231	SXR	1,2 21, 41
Period Gap	*(2 h < P_{orb} < 3 h)*				
XSS J00564+4548	2.624	465.680	0.04929	-	7, 10
Fast rotator	*(P_{spin} / P_{orb} < 0.01)*				
AE Aqr	9.880	33.076	0.00093	DP, Propeller	11, 13, 26, 33, 41
GK Per	47.923	351.332	0.00204	SXR, DP	14, 21, 32, 33
IGR J17303-0601	15.420	128.000	0.00231	SXR	2, 11
DQ Her	4.650	142.000	0.00848	DP	11, 33, 45
XY Ari	6.065	206.300	0.00945	DP	28, 33, 41

[a] SXR: soft X-ray bbody components; DP: double-peaked pulse profiles.

[b] References: (1) (Allan et al. 1998); (2) (Anzolin et al. 2008); (3) (Baskill et al. 2005); (4) (Kim et al. 2005); (5) (Butters et al. 2007); (6) (Bonnet-Bidaud et al. 2007); (7) (Bonnet-Bidaud et al. 2009); (8) (Buckley et al. 1995); (9) (Burwitz et al. 1996); (10) (Butters et al. 2008); (11) (Butters et al. 2009a); (12) (Butters et al. 2009b); (13) (Choi et al. 1999); (14) (Crampton et al. 1986); (15) (de Martino et al. 2008); (16) (de Martino et al. 1999); (17) (de Martino et al. 2006a);(18) (de Martino et al. 2009); (19) (Duck et al. 1994); (20) (Evans & Hellier 2004); (21) (Evans & Hellier 2007); (22) (Gaensicke et al. 2005); (23) (Harlaftis & Horne 1999); (24) (Haswell et al. 1997); (25) (Hilton et al. 2009); (26) (Hellier 2007); (27) (Hellier et al. 1994); (28) (Hellier et al. 1997); (29) (Hellier et al. 2002a); (30) (Hellier et al. 2002b); (31) (Kemp et al. 2002); (32) (Mauche 2004); (33) (Norton et al. 1999); (34) (Norton et al. 2002); (35) (Patterson et al. 2004); (36) (Pretorius 2009); (37) (Hellier et al. 1998); (38) (Staude et al. 2003); (39) (Schlegel 2005); (40) (Scaringi et al. 2011); (41) (Scaringi et al. 2010); (42) (Thorstensen et al. 2010); (43) (de Martino et al. 2006b); (44) (Patterson et al. 2011); (45) (Zhang et al. 1995);

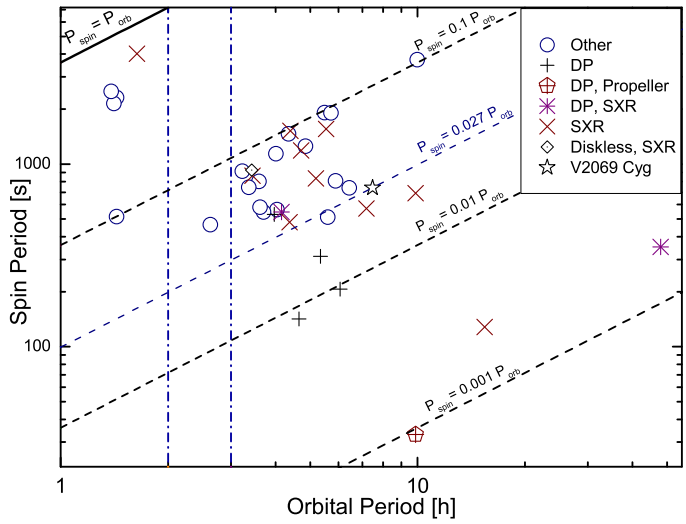

Figure 5.6. $P_{\rm orb}$–$P_{\rm spin}$ diagram of 39 IPs: DP, double-peak pulsation; SXR, soft X-ray component; disk-less, have no accretion disk. The vertical dashed lines show the approximate location of the 'period gap', and the diagonal lines are for $P_{\rm spin}$=$P_{\rm orb}$ (solid) and $P_{\rm spin}$ = *0.1/0.01/0.001* $\times$ $P_{\rm orb}$ (dashed). V2069 Cyg (shown with a star) is located well within the population of double-peak IPs with soft X-ray component but has a rather low spin-orbit period ratio of 0.0276

The X-ray spectra of V2069 Cyg obtained from the *XMM–Newton* were modelled by a thermal plasma emission (kT of $\sim$ 20 keV) and a soft black body component with a partial covering photo-electric absorption model with covering fraction of 0.65. An additional Gaussian emission line at 6.385 keV with an equivalent width of 243 eV is required to account for fluorescent emission from neutral iron. The iron fluorescence ($\sim$6.4 keV) and FeXXVI lines ($\sim$6.95 keV) are clearly resolved in the EPIC spectra. V2069 Cyg and V405 Aur show similar bbody parameters with kT of $\sim$77 eV and $\sim$40 eV (Evans & Hellier 2004), respectively. Moreover, the two IPs have quite similar spin-orbit period ratios of 0.0276 for V2069 Cyg (743.38 s/26928 s) and 0.036 for V405 Aur (545.5 s/14986 s).

We adopted Mukai's classification[10] of IPs and updated his $P_{\rm spin}$–$P_{\rm orb}$ diagram to include V2069 Cyg (see Figure 5.6. and Table 5.2.) Several IPs are found close to $P_{\rm spin}/P_{\rm orb}$ = 0.1. There are 28 systems in the range of $0.01 < P_{\rm spin}/P_{\rm orb} \leq 0.1$ and $P_{\rm orb} > 3$ h, 5 systems with $P_{\rm spin}/P_{\rm orb} \geq 0.1$ and $P_{\rm orb} < 2$ h, and only one system

[10] http://asd.gsfc.nasa.gov/Koji.Mukai/iphome/iphome.html

with $P_{\rm spin}/P_{\rm orb} \sim 0.049$ that lies in the 'period gap'. Finally, there are 5 systems with $P_{\rm spin}/P_{\rm orb} < 0.01$. Those are defined as fast rotating WDs. Only one of them, AE Aqr, shows propeller behaviour. They also show the soft X-ray bbody component in their spectrum (Norton et al. 2004c; Parker et al. 2005; Evans & Hellier 2007; Norton & Mukai 2007; Anzolin et al. 2008).

5.2. Conclusion

Our conclusion can be summarized on two points:

HU Aquarii;

We investigated the long term orbital period change of the eclipsing binary system HU Aqr. We presented new modeling of the orbital ephemeris and created observed minus calculated (O−C) diagram of the system including recent 2008-2011 observations together with the existing data in the literature. In our earlier work (section 4.2.2, by Nasiroglu et al. 2010) we reported a model including a linear and quadratic term as well as two sinusoidal oscillatory terms provides the best fit to the observed eclipses. We found that the orbital period of the system is change with time. We proposed that these variations can be explained in terms of changes in the Light Travel Time due to the presence of smaller 'planetary' bodies orbiting the compact binary at large distances. Also we discussed other probable mechanism which cause the orbital period change of binary systems.

In our later work (by Gozdziewski & Nasiroglu et al. (2012)), we improve the Keplerian, kinematic model of Light Travel Time effect and re-analyse the whole currently available data set. We added almost 60 new, yet unpublished, mostly precision light curves. We determine new mid-egress times with a mean uncertainty at the level of 1 second or better (see section 4.2.1). We claim that because the observations that currently exist in the literature are non-homogeneous with respect to spectral windows (ultraviolet, X-ray, visual, polarimetric mode) and the reported mid-egress measurement errors, they may introduce systematics that affect orbital fits. Indeed, we find that the published data, when taken literally, cannot be explained by any unique

solution. Many qualitatively different and best-fit 2-planet configurations, including self-consistent, Newtonian N-body solutions may be able to explain the data. However, using a new formulation of the Light Travel Time model of the (O−C) to the available data of the HU Aqr system, we found that the previous 2-planet hypothesis is not likely. Morover, using a much extended, precision data set obtained by OPTIMA, we have found that the (O−C) deviations may be consistently explained by the presence of a single circumbinary companion orbiting (with an orbital period of $\sim$10 yr) at a distance of $\sim$4.5 AU with a small eccentricity of $\sim$0.1 and having $\sim$7 Jupiter-masses. This object could be the next circumbinary planet detected from the ground, similar to the announced companions around close binaries HW Vir, NN Ser, UZ For, DP Leo or SZ Her, and planets of this type around Kepler-16, Kepler-34 and Kepler-35.

V2069 Cygni;

We presented fast timing photometric (using OPTIMA at the 1.3 m telescope of Skinakas Observatory) and X-ray observations (Swift/XRT and XMM-Newton) of the intermediate polar V2069 Cygni (Nasiroglu et al. 2012). The optical (450-950 nm) light curve of V2069 Cygni was measured with sub-second resolution for the first time during July 2009. The timing analysis of the optical and X-ray data reveal double-peaked pulsations at periods of 743.38 ± 0.25 s and 742.35 ± 0.23 s respectively, representing the spin period of the WD accretor. We obtained the optical spin period a bit longer than the X-ray spin period, however both periods are compatible within their errors. We conclude that V2069 Cyg is an example of an IP that shows double-peaked emission profiles in both optical and X-ray wavelength at the WD spin period which are probably caused by a weak magnetic field, in a WD with short spin period. The emission profiles of the optical and X-ray data are out of phase. This phase shift exists most probably due to the X-ray and optical/infrared photons originate from two different regions. We also performed simultaneous optical/X-ray observations of V2069 Cyg to search for delays between these two energy bands. However the low count rates in the *Swift* data did not allow to constrain these delays. The X-ray spectra of V2069 Cyg obtained from the *XMM–Newton* described by thermal plasma emission (kT of $\sim$ 20 keV) plus a soft blackbody component with complex absorption and an

additional fluorescent iron-K emission line, which originates on the WD surface (at 6.4 keV, with an EW of 243 eV). In the $P_{\rm orb}$–$P_{\rm spin}$ diagram of IPs, V2069 Cyg shows a low spin to orbit ratio of $\sim$0.0276 in comparison with $\sim$0.1 for other intermediate polars.

REFERENCES

AIZU K., 1973. X-Ray Emission Region of a White Dwarf with Accretion. Progress of Theoretical Physics, 49, 1184-1194.

ALLAN A., HORNE K., HELLIER C., et al., 1996. The spin period of the intermediate polar RX J0558+53.. Monthly Notices of the Royal Astronomical Society, 279, 1345-1348.

ALLAN A., HELLIER C., BEARDMORE A., 1998. ASCA X-ray observations of EX Hya - Spin-resolved spectroscopy. Monthly Notices of the Royal Astronomical Society, 295, 167.

AMARI S., GAO X., NITTLER L. R., et al., 2001. Presolar Grains from Novae. The Astrophysical Journal, 551, 1065-1072.

ANDRONOV N., PINSONNEAULT M., and SILLS A., 2003. Cataclysmic Variables: an emprical angular momentum loss prescription from open cluster data. The Astrophysical Journal, 582:, 358-368.

ANDRAE R., SCHULZE-HARTUNG T., MELCHIOR P., 2010.Dos and don'ts of reduced chi-squared.ArXiv e-prints, arXiv:1012.3754.

ANUPAMA G. C., MIKOLAJEWSKA J., 1999. Recurrent novae at quiescence: systems with giant secondaries. Astronomy and Astrophysics, 344, 177-187.

ANUPAMA G. C., 2002. The Recurrent Novae and Their Relation with Classical Novae. AIP Conference Proceedings, 637, 32-41.

ANUPAMA G. C., 2008. The Recurrent Nova Class of Objects. ASP Conference Series, 401, 31.

ANZOLIN G., DE MARTINO D., BONNET-BIDAUD J.-M., MOUCHET M., GAENSICKE B. T., MATT G., MUKAI K., 2008. Two new intermediate polars with a soft X-ray component. Astronomy and Astrophysics, 489, 1243-1254.

APPLEGATE J. H., 1992. A mechanism for orbital period modulation in close binaries. Astrophysical Journal, 385, 621-629.

ARNAUD K. A., 1996. XSPEC: The First Ten Years. Astronomical Data Analysis Software and Systems V, 101, 17.

AUGUSTEIJN T., TAPPERT C., DALL T., MAZA J., 2010.Cataclysmic variables from the Calaen-Tololo Survey - II. Spectroscopic periods.Monthly Notices of the Royal Astronomical Society, 405, 621-637.

BACKER D. C., FOSTER R. S., SALLMEN S., 1993. A second companion of the millisecond pulsar 1620 - 26. Nature, 365, 817-819.

BALMAN S., 2005. Chandra Observation of the Shell of Nova Persei 1901 (GK Persei): Detection of Localized Nonthermal X-Ray Emission from a Miniature Supernova Remnant. The Astrophysical Journal, 627, 933-952.

BARBON R., CIATTI F., ROSINO L., 1979. Photometric properties of type II supernovae. Astronomy and Astrophysics, 72, 287-292.

BARLOW E., J., et al. 2006. 20-100 keV properties of CVs detected in the INTEGRAL/IBIS survey. Mon. Not. R. Astron. Soc., 372, 224-232.

BASKILL D. S., WHEATLEY P. J., OSBORNE J. P., 2005. The complete set of ASCA X-ray observations of non-magnetic cataclysmic variables. Monthly Notices of the Royal Astronomical Society, 357, 626-644.

BATH G. T., EVANS W. D., PRINGLE J. E., 1974. An oblique rotator model for DQ Herculis. Monthly Notices of the Royal Astronomical Society, 166, 113-121.

BECKER R. H., 1981. X-ray observations of cataclysmic variables. Astrophysical Journal, 251, 626-629.

BECKER R. H., MARSHALL F. E., 1981. An X-ray survey of nine historical novae. Astrophysical Journal, 244, 93-95.

BEDNAREK W., PABICH J., 2011. X-rays and gamma-rays from cataclysmic variables: the example case of intermediate polar V1223 Sgr. Monthly Notices of the Royal Astronomical Society, 411, 1701-1706

BERNARDINI F., de MARTINO D., FALANGA M., MUKAI K., MATT G., BONNET-BIDAUD J. M., MASETTI N., MOUCHET M., 2012. Characterization of new hard X-ray Cataclysmic Variables. Accepted for publication in Astronomy and Astrophysics in April 2012. arXiv, arXiv:1204.3758.

BERRIMAN G., SZKODY P., CAPPS R. W., 1985. The Origin of the infrared light of CV stars. Monthly Notices of the Royal Astronomical Society, 217, 327-346.

BEUERMANN K., BUHLMANN J., DIESE J., et al., 2011. The giant planet orbiting the cataclysmic binary DP Leonis. Astronomy and Astrophysics, 526, A53.

BIRD A. J., et al., 2007. The Third IBIS/ISGRI Soft Gamma-Ray Survey Catalog. The Astrophysical Journal Supplement Series, 170, 175-186.

BODE M. F., EVANS A., 1980. Infrared Emission by Dust Grains near Variable Primary Sources. Astron. Astrophys., 89, 158-168.

BODE M. F., SEAQUIST E.R., EVANS A., 1987. Radio Survey of Classical Novae. Monthly Notices of the Royal Astronomical Society, 228, 217-227.

BODE M. F., LLOYD H. M., 1996. The Origin and Evolution of Radio Emission in Classical and Recurrent Novae. Astronomical Society of the Pacific, 93, 165-173.

BOND H. E., WHITE R. L., BECKER R. H., O'BRIEN M. S., 2002. FIRST J102347.6+003841: The First Radio-selected Cataclysmic Variable. The Publications of the Astronomical Society of the Pacific, 114, 1359-1363.

BONNET-BIDAUD J. M., DE MARTINO D., FALANGA M., MOUCHET M., MASETTI N., 2007. IGR J00234+6141: a new INTEGRAL source identified as an intermediate polar. Astronomy and Astrophysics, 473, 185-189.

BONNET-BIDAUD J. M., DE MARTINO D., MOUCHET M., 2009. XSS J0056+4548 : a hard X-ray intermediate polar in the period gap. The Astronomer's Telegram, 1895, 1.

BRINKWORTH C. S., MARSH T. R., DHILLON V. S., KNIGGE C., 2006. Detection of a period decrease in NN Ser with ULTRACAM: evidence for strong magnetic braking or an unseen companion. Monthly Notices of the Royal Astronomical Society, 365, 287-295.

BRUNSCHWEIGER, J.; GREINER, J.; AJELLO, M.; OSBORNE, J., 2009. Intermediate polars in the Swift/BAT survey: spectra and white dwarf masses. Astronomy and Astrophysics, 496, 121-127.

BUCKLEY D. A. H., SEKIGUCHI K., MOTCH C., O'DONOGHUE D., CHEN A.-L., SCHWARZENBERG-CZERNY A., PIETSCH W., HARROP-ALLIN M. K., 1995. RX J1712.6-2414: a polarized intermediate polar from the ROSAT Galac-

tic Plane Survey. Monthly Notices of the Royal Astronomical Society, 275, 1028-1048.

BUDDING E., DEMIRCAN O., 2007. Introduction to astronomical photometry. Cambridge University Press, Cambridgeiap.

BUNNER A. N., 1978. Soft X-ray results from the Wisconsin experiment on OSO-8. Astrophysical Journal, 220, 261-271

BURROWS D. N., HILL J. E., NOUSEK J. A., et al., 2005. The Swift X-Ray Telescope. Space Science Reviews, 120, 165-195.

BURWITZ V., REINSCH K., BEUERMANN K., THOMAS H. C., 1996. A new soft intermediate polar: RX J0512.2-3241 in Columba. Astronomy and Astrophysics 310, 25-28.

BURWITZ V., 1997. X-ray and optical properties of ROSAT discovered magnetic cataclysmic variables. Dissertation zur Erlangung des Doktorgrades der Mathematisch-Naturwissenschaftlichen Fakultaeten der Georg-August Universitaet zu Goettingen. Publisher, Goettingen, 1997. Length, 99 pages

BURWITZ V., 1998. X-ray and optical properties of ROSAT discovered mCVs. ASP Conference Series, 137.

BUTTERS O. W., BARLOW E. J., NORTON A. J., MUKAI K., 2007. RXTE confirmation of the intermediate polar status of Swift J0732.5-1331. Astronomy and Astrophysics, 475, L29-L32.

BUTTERS O. W., NORTON A. J., HAKALA P., MUKAI K., BARLOW E. J., 2008. RXTE determination of the intermediate polar status of XSS J00564+4548, IGR J17195-4100, and XSS J12270-4859. Astronomy and Astrophysics, 487, 271-276.

BUTTERS O. W., KATAJAINEN S., NORTON A. J., LEHTO H. J., PIIROLA V., 2009a. Circular polarization survey of intermediate polars I. Astronomy and Astrophysics, 496, 891-902.

BUTTERS O. W., NORTON A. J., MUKAI K., BARLOW E. J., 2009b. RXTE confirmation of the intermediate polar status of IGR J15094-6649. Astronomy and Astrophysics, 498, L17-L19.

BUTTERS O. W., NORTON A. J., MUKAI K., TOMSICK J. A., 2011. RXTE and XMM observations of intermediate polar candidates. Astronomy and Astrophysics, 526, A77.

CANNIZZO J. K., 1993, in Accretion Disks in Compact Stellar Systems, ed. J. C. Wheeler, (Singapore: World Scientific), 6.

CHANMUGAM G., DULK G. A., 1982. Radio Emission from AM Herculis-Type Binaries. The Astrophysical Journal, 255, 107-110.

CHANMUGAM G., RAY A., 1984. The rotational and orbital evolution of cataclysmic binaries containing magnetic white dwarfs. Astrophysical Journal, ApJ, 285, 252-257.

CHANMUGAM G., 1987. Radio Emission from Cataclysmic Variables. Astrophysics and Space Science, 130, 53-68.

CHANMUGAM G., RAY A., SINGH K. P., 1991. The formation and detection of strongly magnetic white dwarf binaries in globular clusters. Astrophysical Journal, 375, 600-607.

CHARMANDARIS V., 2006. Astronomy, Astrophysics, and Space Physics in Greece. Organizations and Stragegies in Astronomy, Volume 7, Astrophysics and Space Science Library, Volume 343. arXiv:physics/0604144.

CHOI C.-S., DOTANI T., AGRAWAL P. C., 1999. A Study of the X-Ray Emission of the Magnetic Cataclysmic Variable AE Aquarii. The Astrophysical Journal, 525, 399-406.

CLAYTON D. D., HOYLEF., 1974. Gamma-Ray Lines from Novae. Astrophysical Journal, 187, 101.

CLAYTON D. D., 1981. Li-7 gamma-ray lines from novae. Astrophysical Journal, 244, 97-98.

CORDOVA F. A., MASON K. O., NELSON J. E., 1981. X-ray observations of selected cataclysmic variable stars using the Einstein Observatory. Astrophysical Journal, 245, 609-617.

CORDOVA F. A., MASON K. O., HJELLMING R. M., 1983. A Radio Survey of CV Stars Using The Very Large Array. Publications of The Astronomical Society of

the Pacific, 95, 69-71.

CRAMPTON D., FISHER W. A., COWLEY A. P., 1986. The orbit of GK Persei. The Astrophysical Journal, 300, 788-793.

CRAWFORD J. A., KRAFT R. P., 1956. An Intrepretation of AE Aquarii. Astrophysical Journal, 123, 44.

CRONIN T. W., WARRANT E. J., GREINER B., 2005. Polarization patterns of the twilight sky. Proceedings of the SPIE, 5888, 204-211.

CROPPER M., 1990. The Polars. Space Science Reviews, 54, 195-295.

de MARTINO D., SILVOTTI R., BUCKLEY D. A. H., GAENSICKE B. T., MOUCHET M., MUKAI K., ROSEN S. R., 1999. Time-resolved HST and IUE UV spectroscopy of the intermediate polar FO AQR. Astronomy and Astrophysics, 350, 517-528.

de MARTINO D., MATT G., MUKAI K., et al., 2001. The X-ray emission of the intermediate polar V 709 Cas. Astronomy and Astrophysics, 377, 499-511.

de MARTINO D., BONNET-BIDAUD J.-M., MOUCHET M., GAENSICKE B. T., HABERL F., MOTCH C., 2006a. The long period intermediate polar 1RXS J154814.5-452845. Astronomy and Astrophysics, 449, 1151-1160.

de MARTINO D., MATT G., MUKAI K., et al., 2006b. The X-ray properties of the magnetic cataclysmic variable UU Columbae. Astronomy and Astrophysics, 454, 287-294.

de MARTINO D., MATT G., MUKAI K., et al., 2008. 1RXS J173021.5-055933: a cataclysmic variable with a fast-spinning magnetic white dwarf. Astronomy and Astrophysics, 481, 149-159.

de MARTINO D., BONNET-BIDAUD J. M., FALANGA M., MOUCHET M., MOTCH C., 2009. XMM-Newton discovery of pulsations from IGR J21237+4218=V2069 Cyg. The Astronomer's Telegram, 2089, 1.

DICKEY J. M., LOCKMAN F. J., 1990. H I in the Galaxy. Annual Review of Astronomy and Astrophysics, 28, 215-261.

DOBROTKA A., MINESHIGE S., CASARES J., 2011. Flickering study of nova like systems KR Aur and UU Aqr. arXiv:1111.3744, Accepted for publication in

MNRAS.

DOGGETT J. B. and BRANCH D., 1985. A comparative study of supernova light curves. Astronomical Journal, 90, 2303-2311.

DUCK S. R., ROSEN S. R., PONMAN T. J., NORTON A. J., WATSON M. G., MASON K. O., 1994. ROSAT observations of a soft X-ray emission component in the intermediate polar RE 0751+14.. Monthly Notices of the Royal Astronomical Society, 271, 372-384.

DULK G. A., BASTIAN T. S., CHANMUGAM G., 1983. Radio Emission From AM Her: The Quiescent Component And An Outburst. The Americal Astronomical Society, 273, 249-254.

DUSCHA S., 2007. Software design and development of the improved OPTIMA data acquisition system. Degree Master of Science (Experimental Physics) of the National University of Ireland, Galway.

ELVEY C. T., BABCOCK H. W., 1943. The Spectra of U Geminorum Type Variable Stars. Astrophysical Journal, 97, 412.

ERACLEOUS M., HORNE K., ROBINSON E. L., ZHANG E.-H., MARSH T. R., WOOD J. H., 1994. The ultraviolet pulsations of the cataclysmic variable AE Aquarii as observed with the Hubble Space Telescope. The Astrophysical Journal, 433, 313-331.

EVANS P. A., HELLIER C., 2004. Why does the intermediate polar V405 Aurigae show a double-peaked spin pulse?. Monthly Notices of the Royal Astronomical Society, 353, 447-452.

EVANS P. A., HELLIER C., RAMSAY G., CROPPER M., 2004. Twisted accretion curtains in the intermediate polar FO Aquarii. Monthly Notices of the Royal Astronomical Society, 349, 715-721.

EVANS P. A., HELLIER C., RAMSAY G., 2006. XMM-Newton observations of the complex spin pulse of the intermediate polar PQ Geminorum. Monthly Notices of the Royal Astronomical Society, 369, 1229-1234.

EVANS P. A., HELLIER C., 2007. Why Do Some Intermediate Polars Show Soft X-Ray Emission? A Survey of XMM-Newton Spectra. The Astrophysical Journal,

663, 1277-1284.

FRONING C. S., LONG K. S., KNIGGE C., 2003. Accretion and Outflow in Interacting Binary Systems: Far Ultraviolet Spectroscopic Explorer Observations of the Nova-like Cataclysmic Variable UX Ursae Majoris. The Astrophysical Journal, 584, 433-447.

GALLAGHER J. S., STARRFIELD, S., 1978. Theory and observations of classical novae. Annual review of astronomy and astrophysics 16, 171-214.

GALLAGHER J. S., HEGE E. K, KOPRIVA D. A, WILLIAMS R. E., 1980. Spectrophotometry of the nebula surrounding nova T Aurigae 1891. The Astrophysical Journal, 237, 55-60.

GAENSICKE B. T., JORDAN S., BEUERMANN K., et al., 2004. A 150 MG Magnetic White Dwarf in the Cataclysmic Variable RX J1554.2+2721. The Astrophysical Journal, ApJ, 613, 141-144.

GAENSICKE B. T., MARSH T. R., EDGE A., et al., 2005. Cataclysmic variables from a ROSAT/2MASS selection - I. Four new intermediate polars. Monthly Notices of the Royal Astronomical Society, 361, 141-154.

GEHRZ R. D., TRURAN J. W., WILLIAMS R. E. AND STARRFIELD S., 1998. Nucleosynthesis in Classical Novae and Its Contribution to the Interstellar Medium. The Publications of the Astronomical Society of the Pacific, 110, 3-26.

GEHRZ R. D. et al., 1998. Nucleosynthesis in Classical Novae and Its Contribution to the Interstellar Medium. The Publications of the Astronomical Society of the Pacific, 110, 3-26.

GEISEL S. L., KLEINMANN D. E., LOW F. J., 1970. Infrared Emission of Novae. The Astrophysical Journal,161, 101.

GEHRZ R. D., 1988. The infrared temporal development of classical novae. Annual review of astronomy and astrophysics, 26, 377-412.

GEHRZ R. D., et al. 1995. The Neon Nova. III. The Infrared Light Curves of Nova QU Vulpeculae (Nova VUL 1984-2). Astronomical Journal 110, 325.

GEHRZ R. D., TRURAN J. W., WILLIAMS R. E., STARRFIELD S., 1998. Nucleosynthesis in Classical Novae and Its Contribution to the Interstellar Medium.

The Publications of the Astronomical Society of the Pacific, 110, 3-26.

GIANNONE P., WEIGERT A., 1967. Entwicklung in engen Doppelsternsystemen III. Zeitschrift fr Astrophysik, 67, 41.

GREGORY P. C., LOREDO T. J., 1996. Bayesian Periodic Signal Detection: Analysis of ROSAT Observations of PSR 0540-693. The Astrophysical Journal, 473, 1059.

GOZDZIEWSKI K., Nasiroglu I., et al., 2012. On the HU Aquarii planetary system hypothesis. Monthly Notices of the Royal Astronomical Society,

GOMAZ-GOMAR J., HERNANZ M., JOSE J., ISERN J., 1998. Gamma-ray emission from individual classical novae. Monthly Notices of the Royal Astronomical Society, 296, 913920.

HABERL F., MOTCH C., 1995. New intermediate polars discovered in the ROSAT survey: two spectrally distinct classes. Astronomy and Astrophysics, 297, 37-40.

HABERL F., MOTCH C., ZICKGRAF F.-J., 2002. X-ray and optical observations of 1RXS J154814.5-452845: A new intermediate polar with soft X-ray emission. Astronomy and Astrophysics, 387, 201-214.

HARLAFTIS E. T., HORNE K., 1999. The emission-line pulse pattern in the intermediate polar RX J0558+53. Monthly Notices of the Royal Astronomical Society, 305, 437-448.

HARLAND D. M., 2003. The big bang : a view from the 21st century. Springer-Verlag, London, UK.

HARRIS M. J., et al. 1999. Transient Gamma Ray Spectrometer Observations of Gamma-Ray Lines from Novae. I. Limits on the Positron Annihilation Line in Five Individual Novae. The Astrophysical Journal, 522, 424-432.

HASWELL C. A., PATTERSON J., THORSTENSEN J. R., HELLIER C., SKILLMAN D. R., 1997. Pulsations and Accretion Geometry in YY Draconis: A Study Based on Hubble Space Telescope Observations. The Astrophysical Journal, 476, 847.

HAUSCHILDT P. H., WEHRSE R., STARRFIELD S., SHAVIV G., 1992. Spherically symmetric, expanding, non-LTE model atmospheres for novae during their early

stages. The Astrophysical Journal, 393, 307-328.

HAUSCHILDT P. H., SHORE S. N., SCHWARZ G. J., BARON E., STARRFIELD S., ALLARD F., 1997. Detailed Non-LTE Model Atmospheres for Novae during Outburst. I. New Theoretical Results. The Astrophysical Journal, 490, 803.

HEARN D. R., MARSHALL F. J., 1979. Discovery of a soft X-ray flux from an Ursae Majoris. The Astrophysical Journal, 232, 21-23.

HELLIER C., RAMSEYER T. F., JABLONSKI F. J., 1994. An ephemeris for the intermediate polar RE 0751+14.. Monthly Notices of the Royal Astronomical Society, 271, L25-L29.

HELLIER C., MUKAI K., BEARDMORE A. P., 1997. An outburst of the magnetic cataclysmic variable XY ARIETIS observed with RXTE. Monthly Notices of the Royal Astronomical Society, 292, 397.

HELLIER C., BEARDMORE A. P., BUCKLEY D. A. H., 1998. X-ray confirmation of the new intermediate polar RXJ1238-38. Monthly Notices of the Royal Astronomical Society, 299, 851-854.

HELLIER C., 2001. Cataclysmic Variable Stars. Springer-Praxis, Chichester, UK.

HELLIER C., WYNN G. A., BUCKLEY D. A. H., 2002a. On the accretion mode of the intermediate polar V1025 Centauri. Monthly Notices of the Royal Astronomical Society, 333, 84-92.

HELLIER C., BEARDMORE A. P., MUKAI K., 2002b. The spin pulse of the intermediate polar V1062 Tauri. Astronomy and Astrophysics, 389, 904-907.

HELLIER C., 2007. Disc magnetosphere interactions in cataclysmic variable stars. Star-Disk Interaction in Young Stars, IAU Symposium, 243, 325-336.

HELLIER C., HARMER S., BEARDMORE A. P., 2004. On the magnetic accretor GK Persei in outburst. Monthly Notices of the Royal Astronomical Society, 349, 710-714.

HELLIER C., 2007. Disc magnetosphere interactions in cataclysmic variable stars. Star-Disk Interaction in Young Stars, IAU Symposium, 243, 325-336.

HENRY P., CRUDDACE R., LAMPTON M., PARESCE., BOWYER S., 1975. Limits on the soft X-ray and extreme ultraviolet flux from RX Andromedae and U

Geminorum. Astrophysical Journal, 197, L117-L121.

HERBST W., HESSER J. E., OSTRIKER J. P., 1974. The 71-second variation of DQ Herculis. The Astrophysical Journal, 193, 679-686.

HERNANZ M., JOSE J., 1998. Nucleosynthesis in Classical Novae: Recent Results from TNR Theory. ASP Conference Series, 137, 368.

HERNANZ M., JOSE J., COC A., GOMEZ-GOMAR J., ISERN J., 1999. Gamma-Rays Emission from Novae related to positron annihilation. The Astrophysical Journal, 526, 97-100.

HERNANZ M., et al., 2000. BATSE observations of classical novae. In: McConnell, M.L., Ryan, J.M.(Eds.), 5th COMPTON Symposium, 82. AIP, New York.

HERNANZ M., GOMEZ-GOMAR J., JOSE J., 2002. The prompt gamma-ray emission of novae. New Astronomy Reviews, 46, 599-563.

HERNANZ M., JOSE J., 2004. Gamma-rays from classical novae: expectations from present and future missions. New Astronomy Reviews, 48, 35-39.

HERNANZ M., JOSE J., 2005. Gamma-rays from classical nova explosions: theory and observations. Nuclear Physics A, 758, 721-724.

HILDITCH R. W., 2001. An Introduction to Close Binary Stars. Cambridge University Press, Cambridge, UK.

HILL J. E., et al., 2004. Readout Modes and Automated Operation of the Swift X-Ray Telescope. Proc. SPIE, Vol. 5165.

HILTON E. J., SZKODY P., MUKADAM A., HENDEN A., DILLON W., SCHMIDT G. D., 2009. XMM-Newton and Optical Observations of Cataclysmic Variables from the Sloan Digital Sky Survey. The Astronomical Journal, 137, 3606-3614.

HINSE T. C., LEE J. W., GOZDZIEWSKI K., HAGHIGHIPOUR N., LEE C.U., SCULLION E. M., 2012. New light-travel time models and orbital stability study of the proposed planetary system HU Aquarii. Monthly Notices of the Royal Astronomical Society, 420, 3609-3620.

HJELLMING R., M., WADE C. M., 1970. Radio Novae. The Astrophysical Journal, 162, 1-4.

HJELLMING R. M., GORKOM J. H., TAYLOR A. R., SEAQUIST E. R., PADIN S., DAVIS R. J., BODE M. F., 1986. Radio observations of the 1985 outburst of RS Ophiuchi. The Astrophysical Journal, 305, 71-75.

HOLMES S., et al., 2011. PIRATE: A Remotely Operable Telescope Facility for Research and Education. Publications of the Astronomical Society of the Pacific, 123, 1177.

HONEYCUTT R. K., ROBERTSON J. W., TURNER G. W., 1998. Unusual 'Stunted' Outbursts in Old Novae & Nova-Like Cataclysmic Variables. The Astronomical Journal, 115, 2527-2538.

HONEYCUTT R. K., 2001. Similarities between Stunted Outbursts in Nova-like Cataclysmic Variables and Outbursts in Ordinary Dwarf Novae. The Publications of the Astronomical Society of the Pacific, 113, 473-481.

HORNE K., 1993, in Accretion Disks in Compact Stellar Systems, ed. J. C. Wheeler (Singapore: World Scientific), 117.

HORNER J., MARSHALL J. P., WITTENMYER R. A., TINNEY C. G., 2011. A dynamical analysis of the proposed HU Aquarii planetary system. Monthly Notices of the Royal Astronomical Society, 416, 11-15.

ISRAEL G. L., COVINO S., STELLA L., et al., 2003. Unveiling the Nature of the 321 Second Modulation in RX J0806.3+1527: Near-Simultaneous Chandra and Very Large Telescope Observations. The Astrophysical Journal, 598, 492-500.

IYUDIN A. F., et al. 1995. COMPTEL search for ^{22}Na line emission from recent novae. Astronomy and Astrophysics, 300, 422.

IYUDIN A. F., et al. 1999. COMPTEL Constraints on Nova-Produced ^{22}Na. Astrophysical Letters and Communications, 38, 371.

JAMESON R. F., KING A. R., SHERRINGTON M. R., 1982. Infrared, optical and Ultraviolet observations of TT Ari. Monthly Notices of the Royal Astronomical Society, 200, 455-462.

JENKINS D. G.,2004. Reevaluation of the ^{22}Na (p,γ) Reaction Rate: Implications for the Detection of ^{22}Na Gamma Rays from Novae. Physical Review Letters, 92, id. 031101.

JOSE J., HERNANZ M., 1998. Nucleosynthesis in Classical Novae: CO versus ONe White Dwarfs. The Astrophysical Journal 494, 680.

JOY A. H.,1954. Spectroscopic Observations of AE Aquarii. The Astrophysical Journal, 120, 377.

KAASTRA J., MEWE R., 2000. Coronal Plasmas Modeling and the MEKAL code. Atomic Data Needs for X-ray Astronomy, p. 161, 2000adnx.conf..161K.

KANBACH G., KELLNER S., SCHERY F. Z., STEINLE H., STAUBMEIER C., SPRUIT H. C., 2003. Design and results of the fast timing photo-Polarimeter OPTIMA. Society of Photo-Optical Instrumentation Engineers (SPIE) Conference Series, 4841, 82-93.

KANBACH G., STEFANESCU A., DUSCHA S., et al., 2008. OPTIMA: A High Time Resolution Optical Photo-Polarimeter. Astrophysics and Space Science Library, 351, 153.

KATAJAINEN S., BUTTERS O., NORTON A. J., LETHO H. J., PIIROLA V., BERDYUGIN A., 2010. Discovery of Polarized Emission from Two Soft X-ray-emitting Intermediate Polars: UU Col and NY Lup. The Astrophysical Journal, 724, 165-170.

KATO M., 2002. Recurrent novae, classical novae, symbiotic novae, and population II novae. Astronomical Society of the Pacific, p.595.

KEMP J., PATTERSON J., THORSTENSEN J. R., FRIED R. E., SKILLMAN D. R., BILLINGS G., 2002. Rapid Oscillations in Cataclysmic Variables. XV. HT Camelopardalis (=RX J0757.0+6306). Publications of the Astronomical Society of the Pacific, 114, 623-629.

KIM Y. G., ANDRONOV I. L., PARK S. S., JEON Y.-B., 2005. Orbital and spin variability of the intermediate polar BG CMi. Astronomy and Astrophysics, 441, 663-674.

KENYON S. J., 1988. The Symbiotic Phenomenon. In Astrophysics and Space Science Library, Vol. 145, IAU Colloq. 103, ed. J. Mikolajewska, M. Friedjung, S. J. Kenyon, R. Viotti, 11

KOENIG M., BEUERMANN K., GÄNSICKE B. T., 2006. Irradiated atmospheres of accreting magnetic white dwarfs with an application to the polar AM Herculis. Astronomy and Astrophysics, 449, 1129-1137.

KOKHANOVSKY A. A., 2008. Aerosol Optics: Light Absorption and Scattering by Particles in the Atmosphere. Praxis Publishing Ltd, Chichester, UK.

KRAFT R. P., 1959. The Binary System Nova DQ Herculis. II. an Interpretation of the Spectrum during the Eclipse Cycle. Astrophysical Journal, 130, 110.

KRAFT R. P., 1964. Binary Stars Among Cataclysmic Variables. III. Ten Old Novae. The Astrophysical Journal, 139, 457.

KRAUTTER J., et al. 2002. Hubble Space Telescope NICMOS Observations of Classical Nova Shells. The Astronomical Journal, 124, 28882898.

LAMB D. Q., MASTERS A. R., 1979. X and UV radiation from accreting magnetic degenerate dwarfs. Astrophysical Journal,234, 117-122.

LANDI R., BASSANI L., DEAN A. J., BIRD. J., FIOCCHI M., BAZZANO A., NOUSEK J. A., OSBORNE J. P., 2009. INTEGRAL/IBIS and Swift/XRT observations of hard cataclysmic variables. Monthly Notices of the Royal Astronomical Society, 392, 630-640.

LANZA A. F., RODONO M., ROSNER R., 1998. Orbital period modulation and magnetic cycles in close binaries. Monthly Notices of the Royal Astronomical Society, 296, 4, 893-902.

LASOTA J. P., HAMEURY J. M., HURE J. M., 1995. Dwarf novae at low mass transfer rates. Astronomy and Astrophysics. 302, 29.

LASOTA J. P., 2004. Magnetic Cataclysmic Variables: a Summary. Astronomical Society of the Pacific, 315, 365.

LEISING M. D., CLAYTON D. D., 1987. Positron annihilation gamma rays from novae. Astrophysical Journal, 323, 159-169.

LIVIO M., MASTICHIADIS A., OGELMAN H., TRURAN J. W., 1992. On the role of radioactive decays in powering gamma rays and X-rays from novae. Astrophysical Journal, 394, 217-220.

MASON K. O., LAMPTON M., CHARLES P., BOWYER S., 1978. The discovery of low-energy X-ray emission from U Geminorum. Astrophysical Journal, 226, 129-132.

MASON, P. A., GRAY C. L., 2007.AR Ursae Majoris Discovered to Be a Persistent Radio Polar: Results from a VLA Survey of Magnetic Cataclysmic Variables. The Astrophysical Journal, 660, 662-668.

MATEO M., SZKODY P., GARNAVICH P., 1991. Near-Infrared Time-Resolved Spectroscopy of the CV YY Draconis. Astrophysical Journal, 370, 370-383.

MAUCHE C. W., 2004. The Spin-Up Rate of the White Dwarf in GK Per. IAU Colloq. 190: Magnetic Cataclysmic Variables, in Vrielmann S., Cropper M., eds, ASP Conf. Ser. Vol. 315, 120.

MAZZUCA L., SPARKS B., AXON D., 1998. Methodologies to Calibrating NICMOS Polarimetry Characteristics. Instrument Science Report NICMOS 98-017, 17.

MCLAUGHLIN, D. B., 1960. The Spectra of Novae. Published by the University of Chicago Press, Chicago, 585.

MEWE R., GRONENSCHILD E. H. B. M., VAN DEN OORD G. H. J., 1985. Calculated X-radiation from optically thin plasmas. V. Astronomy and Astrophysics Supplement Series, 62, 197-254.

MIKOLAJEWSKA J., 2003. Orbital and Stellar Parameters of Symbiotic Stars. ASP Conference Series, 303, 9.

MIKOLAJEWSKA .J, 2011. Symbiotic stars as possible progenitors of SNe Ia: binary parameters and overall outlook. IAU Symposium No. 281.

MANZOORI D., 2007. Orbital Period Modulation in SW Cygni. Publications of the Astronomical Society of Australia, 24, 61-68.

MOTCH C., HABERL F., GUILLOUT P., PAKULL M., REINSCH K., KRAUTTER J., 1996. New cataclysmic variables from the ROSAT All-Sky Survey.. Astronomy and Astrophysics, 307, 459-469.

MOUCHET M., BONNET-BIDAUD J. M., de MARTINO D., 2012. The X-ray emission of magnetic cataclysmic variables in the XMM-Newton era.

ArXiv:1202.3594.

MUERSET U., NUSSBAUMER H., SCHMID H. M., VOGEL M., 1991. Temperature and luminosity of hot components in symbiotic stars. Astronomy and Astrophysics, 248, 458-474.

MUHLEGGER M., 2006. Entwicklung und Einsatz eines Wollaston-Polarimeters fr die Hochgeschwindigkeitsastronomie mit OPTIMA-Burst". Diploma thesis, University of Technology Munich.

MUMFORD G. S., 1967. Novae and Novalike Variables. Publications of the Astronomical Society of the Pacific, 79, 283.

MUNO. M., P., et al. 2006. The Spectra and variability of X-ray sources in a deep Chandra observation of Galactic center. The Astrophysical Journal, 613, 1179-1201.

NAGEL T., RAUCH T., DREIZLER S., WERNER K., 2004. Modeling He-rich Disks in AM CVn Binaries. Revista Mexicana de Astronomay Astrofsica(Serie de Conferencias) 20, 228-228.

NASIROGLU I., SLOWIKOWSKA A., KANBACH G., SCHWARZ R., SCHWOPE A. D., 2010, in High Time Resolution Astrophysics (HTRA) IV-48. The orbital ephemeris of HU Aquarii observed with OPTIMA. Are there two giant planets in orbit?

NASIROGLU I., SLOWIKOWSKA A., KANBACH G., HABERL F., 2012. Very fast photometric and X-ray observations of the intermediate polar V2069 Cygni (RX J2123.7+4217). Monthly Notices of the Royal Astronomical Society, 420, 3350-3359.

NORTON A. J., BEARDMORE A. P., ALLAN A., HELLIER C., 1999. YY Draconis and V709 Cassiopeiae: two intermediate polars with weak magnetic fields. Astronomy and Astrophysics, 347, 203-211.

NORTON A. J., QUAINTRELL H., KATAJAINEN S., LEHTO H. J., MUKAI K., NEGUERUELA I., 2002. Pulsations and orbital modulation of the intermediate polar 1WGA J1958.2+3232. Astronomy and Astrophysics, 384, 195-205

NORTON A. J., SOMERSCALES R. V., PARKER T. L., WYNN G. A., WEST R. G., 2004a. Accretion Flows in Magnetic Cataclysmic Variables. Revista Mexicana de Astronomiay Astrofisica Conference Series, 20, 138-139.

NORTON A. J., HASWELL C. A., WYNN G. A., 2004b. Face-on, stream-fed intermediate polars: An alternative model for RX J1914.4+2456 and RX J0806.3+1527. Astronomy and Astrophysics, 419, 1025-1033.

NORTON A. J., WYNN G. A., SOMERSCLAES R. V., 2004c. The Spin Periods and Magnetic Moments of White Dwarfs in Magnetic Cataclysmic Variables. The Astrophysical Journal, 614, 349-357.

NORTON A. J., MUKAI K., 2007. A precessing accretion disc in the intermediate polar XY Arietis?. Astronomy and Astrophysics, 472, 225-232.

NORTON A. J., BUTTERS O. W., PARKER T. L., WYNN G. A., 2008. The Accretion Flows and Evolution of Magnetic Cataclysmic Variables. The Astrophysical Journal, 672, 524-530.

O'DELL S. L., et al. 2010. High-resolution x-ray telescopes. Proceedings of the SPIE, 7803, 78030-78030.

ORIO M., COVINGTON J., OGELMAN H., 2001a. X-ray emission from classical and recurrent novae observedwith ROSAT. Astronomy and Astrophysics, 373, 542-554.

ORIO M., et al. 2001b. The X-ray emission from Nova V382 Velorum - I. The hard component observed with BeppoSAX. Monthly Notices of the Royal Astronomical Society, 326, 13-17.

ORIO M., 2004. X-Ray Observations of Classical and recurrent Novae in Outburst. Revista Mexicana de Astronomay Astrofsica(Serie de Conferencias), 20, 182-186.

OSAKI Y., 1996. Dwarf Nova Outbursts. The Publications of the Astronomical Society of the Pacific, 108, 39-60.

PATTERSON J., 1994. The DQ Herculis stars. Publications of the Astronomical Society of the Pacific, 106, 209-238.

PARKER T. L., NORTON A. J., MUKAI K., 2005. X-ray orbital modulations in intermediate polars. Astronomy and Astrophysics, 439, 213-225.

PATTERSON J., THORSTENSEN J. R., VANMUNSTER T., et al., 2004. Rapid Oscillations in Cataclysmic Variables. XVI. DW Cancri. Publications of the Astronomical Society of the Pacific, 116, 516-526.

PATTERSON J., THORSTENSEN J. R., SHEETS H. A., et al., 2011. Rapid Oscillations in Cataclysmic Variables. XVII. 1RXS J 070407 + 262501. Publications of the Astronomical Society of the Pacific, 123, 130-137.

PAVELIN P.E., SPENCER R.E., DAVIS R. J., 1994. A 5-GHz radio survey of Magnetic CVs. Mon. Not. R. Astron. Soc., 269, 779-784.

PARKER T. L., NORTON A. J., MUKAI K., 2005. X-ray orbital modulations in intermediate polars. Astronomy and Astrophysics, 439, 213-225.

PATTERSON J., RAYMOND L. C., 1985. X-ray emission from cataclysmic variables with accretion disks. I-Hard X-rays. II-EUV/soft X-ray radiation. Astrophysical Journal, Part 1, 292, 535-558.

PATTERSON J., THORSTENSEN J. R., VANMUNSTER T., et al., 2004. Rapid Oscillations in Cataclysmic Variables. XVI. DW Cancri. Publications of the Astronomical Society of the Pacific, 116, 516-526.

PATTERSON J., THORSTENSEN J. R., SHEETS H. A., et al., 2011. Rapid Oscillations in Cataclysmic Variables. XVII. 1RXS J 070407 + 262501. Publications of the Astronomical Society of the Pacific, 123, 130-137.

PAYNE-GAPOSCHKIN C., 1957. The Galactic Novae. Amsterdam, North Holland.

PERCY J. R., 2007. Understanding Variable Stars. Cambridge University Press.

PERLMUTTER S., 1999. Constraining Dark Energy with Type Ia SNe and Large-Scale Structure. Physical Review Letters, 83, 670-73.

POTTER S. B., ROMERO-COLMENERO E., KOTZE M., ZIETSMAN E., BUTTERS O. W., PEKEUR N., BUCKLEY D. A. H., 2012. On the spin modulated circular polarization from the intermediate polars NY Lup and IGR J15094-6649. Monthly Notices of the Royal Astronomical Society, 420, 2596-2602.

PRETORIUS M. L., 2009. Time-resolved optical observations of five cataclysmic variables detected by INTEGRAL. Monthly Notices of the Royal Astronomical Society, 395, 386-393.

PRIALNIK D., SHARA M. M., SHAVIV G., 1979. The evolution of a fast nova model with a Z = 0.03 envelope from pre-explosion to decline. Astronomy and Astrophysics, 72, 192203.

PRIALNIK D., KOVETZ A., 1984. The effect of diffusion on prenova evolution - CNO- enriched envelopes. Astrophysical Journal, 281, 367374.

PRIALNIK D., 1986. The evolution of a classical nova model through a complete cycle. Astrophysical Journal, 310, 222237.

QIAN S.-B., LIAO W.-P., ZHU L.-Y., DAI Z.-B., 2010. Detection of a Giant Extrasolar Planet Orbiting the Eclipsing Polar DP Leo. The Astrophysical Journal, 708, 66-68.

QIAN S.-B., LIU L., LIAO W.-P., et al., 2011. Detection of a planetary system orbiting the eclipsing polar HU Aqr. Monthly Notices of the Royal Astronomical Society, 414, 16-20.

QIAN S.-B.,Qian, BOONRUCKSAR S., 2003. Long-Term Orbital Period Variations for EU Hydrae. Publications of the Astronomical Society of Japan, 55, 499-502.

RAPPAPORT S., CASH W., DOXSEY R., MCCLINTOCK J., MOORE G., 1974. Possible Detection of Very Soft X-Rays from SS Cygni. Astrophysical Journal, 187, 5.

RAPPAPORT S., VERBUNT F., JOSS P. C., 1983. A new technique for calculations of binary stellar evolution, with application to magnetic braking. Astrophysical Journal, 275, 713.

REVNIVTSEV M., SAZONOV S., GILFANOV M., CHURAZOV E., SUNYAEV R., 2006. Origin of the Galactic ridge X-ray emission Astronomy and Astrophysics, 452, 169-178

REVNIVTSEV M., BURENIN R., BIKMAEV I., et al., 2010. Aperiodic optical variability of intermediate polars - cataclysmic variables with truncated accretion disks. Astronomy and Astrophysics, 513, A63.

RIESS A. G. et al., 1998. Observational Evidence from Supernovae for an Accelerating Universe and a Cosmological Constant. ApJ, 116, 1009-1038.

RINGWALD F. A., NAYLOR T., 1998. High-Speed Optical Spectroscopy of a Cataclysmic Variable Wind: BZ Cam. The Astronomical Journal, 115:286-295.

RITTER H., KOLB U., 2011. Catalogue of cataclysmic binaries, low-mass X-ray binaries and related objects (Seventh edition). Astronomy and Astrophysics, 404, 301-303.

RODRIGUES C. V., JABLONSKI F. J, D'AMICO F., CIESLINSKI D., STEINER J. E., DIAZ M. P., HICKEL G. R., 2006. Optical polarimetry and infrared photometry of two AM Her binaries: 1RXS J161008.8+035222 AND 1RXS J231603.9 -052713. Monthly Notices of the Royal Astronomical Society, 369, 1972-1982.

ROSEN S. R., MASON K. O., CORDOVA F. A., 1988. EXOSAT X-ray observations of the eclipsing magnetic cataclysmic variable EX Hya. Monthly Notices of the Royal Astronomical Society, 231, 549-573.

RUITER A. J., BELCZYNSKI K., HARRISON T. E., 2006. The Nature of the Faint Chandra X-Ray Sources in the Galactic Center. The Astrophysical Journal, 640, 167-170.

SCARINGI S., BIRD A. J., NORTON A. J., et al., 2010. Hard X-ray properties of magnetic cataclysmic variables. Monthly Notices of the Royal Astronomical Society, 401, 2207-2218.

SCARINGI S., CONNOLLY S., PATTERSON J., ET AL., 2011. Confirmation of ASTROBJ 1RXS J165443.5-191620 /ASTROBJ as an intermediate polar and its orbital and spin periods. Astronomy and Astrophysics, 530, A6.

SCHATZMAN E. 1965. The Theory of Novae and Supernovae. Published by the University of Chicago Press, Chicago, ILL USA, 1965, 327.

SCHLEGEL E., M., 1999. ROSAT High Resolution Imager Observations of Three Magnetic Cataclysmic Variables. The Astronomical Journal, 117, 2494-2502.

SCHLEGEL E. M., 2005. A serendipitous XMM-Newton observation of the intermediate polar WX Pyx. Astronomy and Astrophysics, 433, 635-639.

SCHWARZ R., SCHWOPE A. D., VOGEL J., DHILLON V. S., MARSH T. R., COPPERWHEAT C., LITTLEFAIR S. P., KANBACH G., 2009. Hunting high and low: XMM monitoring of the eclipsing polar HU Aquarii. Astronomy and Astrophysics, 496, 833-840.

SCHWOPE A. D., THOMAS H. C., BEUERMANN K., 1993. Discovery of the Bright Eclipsing Polar RX:J2107.9-0518. Astronomy and Astrophysics, 271, 25.

SCHWOPE A. D., SCHWARZ R., SIRK M., HOWELL S. B., 2001. The soft X-ray eclipses of HU Aqr. Astronomy and Astrophysics, 375, 419-433.

SCHWOPE A. D., HORNE K., STEEGHS D., STILL M., 2011. Dissecting the donor star in the eclipsing polar HU Aquarii. Astronomy and Astrophysics, 531, 34.

SENZIANI F., SKINNER G. K., JEAN P.; HERNANZ M., 2008. Detectability of gamma-ray emission from classical novae with Swift/BAT. Astronomy and Astrophysics, 485, 223-231.

SHARA M. M., PRIALNIK D., SHAVIV G., 1980. What determines the speed class of novae. Astrophysical Journal, 239, 586591.

SHARA M. M., 1989. Recent progress in understanding the eruptions of classical novae. Astronomical Society of the Pacific, Publications, 101, 5-31.

SION E. M., 2001. Hubble Space Telescope Spectroscopy of the Dwarf Nova RX Andromedae. The Underlying White Dwarf. The Astrophysical Journal, 555, 834838.

SKOPAL A. et al., 2004. Photometry of symbiotic stars. Contributions of the Astronomical Observatory Skalnat Pleso, 34, 45-69.

SMAK J., 1994. Eclipses in Cataclysmic Variables with Stationary Accretion Disks. II. UX UMa. Acta Astronomica, 44, 59-74.

SOUTHWORTH J., COPPERWHEAT C. M., GAENSICKE B. T., PYRZAS S., 2010. Orbital periods of cataclysmic variables identified by the SDSS. VII. Four new eclipsing systems.Astronomy and Astrophysics, 510, A100.

SPARKS W. B., AXON D. J., 1999. Panoramic Polarimetry Data Analysis. Publications of the Astronomical Society of the Pacific, 111, 1298-1315.

STARRFIELD S., 1971. On the cause of the Nova outburst. Monthly Notices of the Royal Astronomical Society, 152, 307.

STARRFIELD S., TRURAN J. W., SPARKS W. M., KUTTER G. S., 1972. CNO Abundances and Hydrodynamic Models of the Nova Outburst. The Astrophysical Journal, 176, 169.

STARRFIELD S., TRURAN J. W., SPARKS W. M., 1974a. CNO Abundances and Hydrodynamic Models of the Nova Outburst. II - 1.00 solar mass models with enhanced carbon and oxygen. The Astrophysical Journal Supplement Series, 28, 247-270.

STARRFIELD S., TRURAN J. W., SPARKS W. M., 1974b. CNO Abundances and Hydrodynamic Models of the Nova Outburst. III - 0.5 solar mass models with enhanced carbon, oxygen, and nitrogen. Astrophysical Journal, 192, 647-655.

STARRFIELD S., TRURAN J. W., SPARKS W. M., 1978. CNO Abundances and Hydrodynamic Studies of the Nova Outburst. 1.00 solar mass models with small mass envelopes. The Astrophysical Journal, 192, 647-655.

STARRFIELD S., SPARKS W. M., TRURAN J. W., 1985. Recurrent novae as a consequence of the accretion of solar material onto a 1.38 solar mass white dwarf. ApJ, 291, 136-146.

STARRFIELD S., SPARKS W. M., TRURAN J. W., 1986. Hydrodynamic models for novae with ejecta rich in oxygen, neon, and magnesium. ApJ, 303, L5.

STARRFIELD S. et al., 1988. A model for the 1987 outburst of the recurrent nova U Scorpii. Astrophysical Journal, 325, L35-L38.

STARRFIELD S., 1989, in Classical Novae, 1st ed., ed. M.Bode, A.Evans, New York and Chichester: Wiley, p. 3

STARRFIELD S. et al., 1998. Observational and Theoretical Studies of the Nova Outburst. ASP Conference Series, 137, 352.

STARRFIELD, S., 2002. Studies of Novae in the 20th Century. International Conference on Classical Nova Explosions. AIP Conf. Proceedings, 637, 89-98.

STAUDE A., SCHWOPE A. D., KRUMPE M., HAMBARYAN V., SCHWARZ R., 2003. 1RXS J062518.2+733433: A bright, soft intermediate polar. Astronomy

and Astrophysics, 406, 253-257.

STAUDE A., SCHWOPE A. D., SCHWARZ R., VOGEL J., KRUMPE M., NEBOT GOMEZ-MORAN A., 2008. The changing accretion states of the intermediate polar MU Camelopardalis. Astronomy and Astrophysics, 486, 899-909.

STEFANESCU A., 2004. Anpassung und Einsatz des OPTIMA Photometers zur Messung von GRB-Afterglow-Kandidaten. Master thesis, University of Technology Munich.

STEFANESCU A., 2011. Design and Application of an Optical High Time Resolution Instrument for High-Energy Transients, PhD Thesis, University of Technology Munich.

STRAUBMEIER C., KANBACH G., SCHREY F., 2001. OPTIMA: A Photon Counting High-Speed Photometer. Experimental Astronomy, 11, 157-170.

STRUEDER L., BRIEL U., DENNERL K., et al., 2001. The European Photon Imaging Camera on XMM-Newton: The pn-CCD camera. Astronomy and Astrophysics, 365, L18-L26.

SULEIMANOV V., POUTANEN J., FALANGA M., WERNER K., 2008. Influence of Compton scattering on the broad-band X-ray spectra of intermediate polars. Astronomy and Astrophysics, 491, 525-529.

SUZUKI A., SHIGEYAMA T., 2010. Compton Degradation of Gamma-ray Line Emission from Radioactive Isotopes in the Classical Nova V2491 Cygni. The Astrophysical Journal Letters, 723, L84-L88.

SZKODY P., et al. 2010. Finding the instability of accreting pulsating white dwarfs from HST and Optical obsrvations 2010. The Astrophysical Journal. 710, 64

SZKODY P., ANDERSON S. F., BROOKS K., et al., 2011. Cataclysmic Variables from the Sloan Digital Sky Survey. VIII. The Final Year (2007-2008).The Astronomical Journal, 142, 181.

TANG S. et al., 2011. Discovery of A Peculiar Slow Nova in A Peculiar Symbiotic Binary. 2011arXiv1110.0019T. 30 pages, 7 figures, submitted to ApJ.

TANZI E. G., CHINCARINI G., TARENGHI M.,1980.Infrared Observations of AE Aquarii. Publications of the Astronomical Society of the Pacific, 93, 68-70.

THORSTENSEN J. R., TAYLOR C. J., 2001. Spectroscopy and orbital periods of four cataclysmic variable stars. Monthly Notices of the Royal Astronomical Society, 326, 1235-1242.

THORSTENSEN J. R., PETERS C. S., SKINNER J. N., 2010. Optical Studies of 20 Longer-Period Cataclysmic Binaries. Publications of the Astronomical Society of the Pacific, 122, 1285-1302.

TINBERGEN J., 1996. Astronomical Polarimetry. Cambridge University Press, Cambridge.

TOWNSLEY D.M., BILDSTEN L., 2005. Classical Novae as a Probe of the Cataclysmic Variable Population. ApJ, 628, 395-400.

TURNER M. J. L., ABBEY A., ARNAUD M., et al., 2001. The European Photon Imaging Camera on XMM-Newton: The MOS cameras : The MOS cameras. Astronomy and Astrophysics, 365, L27-L35.

TURNSHEK D. A., 1996. An Atlas of Hubble Space Telescope Photometric, Spectrophotometric, and Polarimetric calibration objects. Astron. J. 99, 1243-1261.

URBAN J. A., and SION E. M., 2006. The Dwarf Novae during Quiescence. The Astrophysical Journal, 642, 1029-1041. Urban-Sion2006

VAN TEESELING A., VERBUNT F., 1994. ROSAT X-ray observations of ten cataclysmic variables. Astronomy and Astrophysics, 292, 519-533 .

VERBUNT F., 1987. Ultraviolet observations of cataclysmic variables: the IUE archive. Astron. Astrophys. Suppl. Ser. 71, 339-361.

VERBUNT F., BUNK W. H., RITTER H., PFEFFERMANN E., 1997. Cataclysmic variables in the ROSAT PSPC All Sky Survey. Astronomy and Astrophysics, 327, 602-613.

VOGEL J., SCHWOPE A., SCHWARZ R., KANBACH G., DHILLON V. S., MARSH T. R., 2008. On the orbital period of the magnetic cataclysmic variable HU Aquarii. High Time Resolution Astrophysics: The Universe at Sub-Second Timescales, 984, 264-267.

VOGEL J., 2008. The spectral energy distribution of polars. PhD Thesis, University of Technology Berlin.

WALKER M. F., 1954. Nova DQ Herculis (1934): an Eclipsing Binary with Very Short Period. Publications of the Astronomical Society of the Pacific, 66, 230.

WALKER M. F., 1956. A Photometric Investigation of the Short-Period Eclipsing Binary. Astrophysical Journal, 123, 68.

WARNER B., 1972. Observations of Blue Rapid Blue Variables-VII EX Hydrae. Monthly Notices of the Royal Astronomical Society, 158, 425-430.

WARNER B., 1995. Cataclysmic Variable Stars. Cambridge University Press, Cambridge, UK.

WARNER B., 2006. Cataclysmic Variables: From Radio to Gamma Rays. The Journal of the American Association of Variable Star Observers, 35, 98-106.

WEBBINK R. F. et al., 1987. The nature of the recurrent novae. The Astrophysical Journal, 314, 653-72.

WHEELER J. C. and HARKNESS R. P., 1990. Type I Supernovae. Rep. Prog. Phys., 53, 1467-1557.

WICKRAMASINGHE D. T., FERRARIO L., 2000. Magnetism in Isolated and Binary White Dwarfs. he Publications of the Astronomical Society of the Pacific, 112, 873-924.

WILLIAMS R. E., WOLLF N. J., HEGE E. K., MOORE R. L., KOPRIVA D. A., 1978. The shell around nova DQ Herculis 1934. The Astrophysical Journal, 224, 171-181.

WILLIAMS R. E., GALLAGHER J. S., 1979. Spectrophotometry of filaments surrounding nova RR Pictoris 1925. The Astrophysical Journal, 228, 482-490.

WILLIAMS R. E., NEY E. P., SPARKS W. M., STARRFIELD S. G., WYCKOOF S., TRURAN J. W., 1984. Ultraviolet spectral evolution and heavy elemnt abundance in Nova Coronae Austrinae 1981. Monthly Notices of the Royal Astronomical Society, 212, 753.

WILLIAMS R. E., NEY E. P., SPARKS W. M., STARRFIELD S. G., WYCKOOF S., TRURAN J. W., 1984. Ultraviolet spectral evolution and heavy elemnt abundance in Nova Coronae Austrinae 1981. Monthly Notices of the Royal Astronomical Society, 212, 753.

WITTENMYER R.A., HORNER J., MARSHALL J. P., BUTTERS 0. W. TINNEY C. G., 2012. Revisiting the proposed planetary system orbiting the eclipsing polar HU Aquarii. Monthly Notices of the Royal Astronomical Society, 419, 3258-3276

WOOD J. H., 1992. Studying CVs with the Hubble Space Telescope. Publications of the Astronomical Society of the Pasific. 104, 780.

ZHANG E., ROBINSON E. L., STIENING R. F., HORNE K., 1995. The 71 Second Oscillation in the Light Curve of the Old Nova DQ Herculis. The Astrophysical Journal, 454, 447.

CIRRICULUM VITAE

I was born in Antakya (Hatay), in 10/10/1978. After completing the first, middle and high school educations in Antakya, I registered to the Balikesir University Physics Department in 1998. I graduated from the Pyhsics Department in 2002. In 2003, I started to M.Sc. education in Cukurova University, Institute of Basic and Applied Sciences. The first year I took English Preparatory course. I completed my M.Sc. education on the high energy astrophysics and observational optical astronomy in 2007. Then in the same year I have started to Ph.D. program at the same institute. I have also worked as a research student in UZAYMER (Space Science and Solar Energy Research and Application Center), Adana, in 2005−2008.

Also, I have been at Technical University of Munich, with ERASMUS exchange program, at the MPE (Max-Planck-Institut fr extraterrestrische Physik, Garching, Germany) as a research student supported by the multinational European research project 'ASTRONS' (Astrophysics of Neutron Stars) during my Ph.D. studies (2008−2011), and at the Institute of Astronomy, University of Zielona Gora, Poland, in 2010 and 2012, supported by Polish Foundation for Science grant number HOM/2009/11B.

I have joined an international project which is called OPTIMA (Optical TIMing Analyzer) in 2007. OPTIMA is one of the active experimental project at MPE. And I also have attended to OPTIMA-Burst Observation Campaigns in September 2007, Jun-July 2009 and Jun-July 2010, in Skinakas Observatory, Crete, Greece.

APPENDIX

1.1. Mathematical Process for Stokes Parameter (I, Q, U)

This part describes the mathematical process of Stokes Parameters (I, Q, U) for the case of n polarizers after Sparks & Axon (1999).

Polarizing element characteristics;

A linearly polarizing element requires three quantities to characterize its behavior or response fully. These are:

1. ε, the efficiency of the polarizer (i.e., the ability to reject and accept polarized light of perpendicular and parallel orientations),
2. t, the overall throughput, in particular to unpolarized light,
3. ϕ, the position angle of the polarizer.

There are a variety of conventions commonly used to present these quantities (Mazzuca et al. 1998). The most common convention is that, the output intensity of a beam with input Stokes parameters (I, Q, U) passing through a polarizing element is adopted as

$$I_k = \frac{1}{2} t_k \left[I + \varepsilon_k (cos2\phi_k Q + sin2\phi_k U) \right] \tag{1.1}$$

where, the subscript k anticipates that the polarizing element is the kth of a series. In this expression three perfect polarizers at the optimal orientation could have $t_k = 1$, $\varepsilon_k = 1$, $(\phi_1, \phi_2, \phi_3) = (0^\circ, 60^\circ, 120^\circ)$. On the other hand, a perfectly bad polarizer would have $t_k = 2$, $\varepsilon_k = 0$, and the (ϕ_k values can be anything since ε is zero). In the case of n polarizers of arbitrary characteristics, a direct observation of the target without any polarizing element in the beam to include as part of the observing sequence could be used. Then the Equation 1.1 will allow this additional observation to form part of the derivation of polarization quantities to maximize the obtainable signal-to-noise ratio (S/N).

In the case of n=4 observations of a source (which can be done with OPTIMA Wollaston polarimeter) simultaneously, the polarizing element and characteristics of

each polarizer are known. To obtain a solution for the three unknowns in the description of the polarization of the incoming light, at least three observations must be made. Through the *k*th polarizer, the measured intensity I_k is related to the Stokes parameters and polarizer characteristics by Equation 1.1. The uncertainty associated with the measurement I_k is denoted as $\sigma_k = \sqrt{I_k}$ which is assumed to follow Poisson distribution.

The case of three polarizers;

The minimum number of polarization observations required to determine the three unknowns represented by the Stokes parameters is obviously three (to be three polarizers at approximately 60° orientation with respect to one another). Using Equation (1.1) with *k* in the range $1-3$, three equations for the three unknowns, (I,Q,U) can be derived:

$$I_1 = \frac{1}{2}t_1\left[I + \varepsilon_1(cos2\phi_1 Q + sin2\phi_1 U)\right]$$

$$I_2 = \frac{1}{2}t_2\left[I + \varepsilon_2(cos2\phi_2 Q + sin2\phi_2 U)\right]$$

$$I_3 = \frac{1}{2}t_3\left[I + \varepsilon_3(cos2\phi_3 Q + sin2\phi_3 U)\right]$$

This complicated linear system may be explicitly solved to yield

$$(I,Q,U) = A\begin{pmatrix} I_1 \\ I_2 \\ I_3 \end{pmatrix} \tag{1.2}$$

or by a minor simplification,

$$(I,Q,U) = B \begin{pmatrix} I_1^* \\ I_2^* \\ I_3^* \end{pmatrix} \tag{1.3}$$

where, $I_k^* = I_k/(0.5t_k)$, i.e., the matrix A is the matrix B with rows divided by $0.5t_k$ and the matrix B is given by

$$B = \begin{pmatrix} \varepsilon_2\varepsilon_3 sin(2\phi_3 - 2\phi_2) & \varepsilon_1\varepsilon_3 sin(2\phi_1 - 2\phi_3) & \varepsilon_1\varepsilon_2 sin(2\phi_2 - 2\phi_1) \\ \varepsilon_2 sin2\phi_2 - \varepsilon_3 sin2\phi_3 & \varepsilon_3 sin2\phi_3 - \varepsilon_1 sin2\phi_1 & \varepsilon_1 sin2\phi_1 - \varepsilon_2 sin2\phi_2 \\ \varepsilon_3 cos2\phi_3 - \varepsilon_2 cos2\phi_2 & \varepsilon_1 cos2\phi_1 - \varepsilon_3 cos2\phi_3 & \varepsilon_2 cos2\phi_2 - \varepsilon_1 cos2\phi_1 \end{pmatrix} /\Omega, \tag{1.4}$$

where,

$$\Omega = \varepsilon_1\varepsilon_2 sin(2\phi_2 - 2\phi_1) + \varepsilon_2\varepsilon_3 sin(2\phi_3 - 2\phi_2) + \varepsilon_1\varepsilon_3 sin(2\phi_1 - 2\phi_3) \tag{1.5}$$

For the calibration measurements and data analysis of OPTIMA observations, a similar solution (Sparks & Axon 1999) can be adapted for *n* (or n=4) polarizers which is described below.

The case of n polarizers;

An analogous solution can be obtained for the case of n polarizers. For this solution Sparks & Axon (1999) started with three unknowns, which are associated with the 3×3 covariance matrix as above, and they adopted a maximum likelihood approach, which is equivalent to a least-squares minimisation.

We assume that the true underlying values of the Stokes parameters of the target are I, Q, U. In that case a mean intensity through the *k*th polarizer of $I_k^{'}$ can be expected to be observed as in Equation (1.1):

$$I_k^{'} = \frac{1}{2} t_k [I + \varepsilon_k (cos2\phi kQ + sin2\phi_k U)] \tag{1.6}$$

Hence the likelihood of observing a particular value I_k, given an underlying mean of $I_k^{'}$ is

$$\rho_k = \frac{1}{\sqrt{2\pi\sigma_k}} e^{-(I_k - I_k^{'})^2/2\sigma_k^2}$$

and hence the likelihood of observing a set of n values (I_k) is

$$\rho_k = \rho_1\rho_2...\rho_n, \qquad \rho = \rho_0 exp[\frac{(I_1-I_1^{'})^2}{2\sigma_1^2} - \frac{(I_2-I_2^{'})^2}{2\sigma_2^2} - \frac{(I_3-I_3^{'})^2}{2\sigma_3^2} - ...]$$

where ρ_0 is a constant. Maximising the likelihood ρ function is equivalent to minimising the absolute value of the exponent, which is a sum of normalised deviations from the mean value. This is the "least-squares" estimation which minimises the differences in the problem.

$$\chi^2 = \frac{1}{2}\sum_k \frac{(I_k - I_k^{'})^2}{\sigma_k^2}, \tag{1.7}$$

The values of $I_k^{'}$ can be substituted into Equation (1.7) from Equation (1.6), and minimisation of χ^2 is obtained by taking partial derivatives with respect to each of I, Q, U in turn and equating to zero. Algebraic manipulation leads to a set of three equations

$$\sum \frac{I_k t_k}{\sigma_k^2} = \frac{1}{2}\sum \frac{t_k^2}{\sigma_k^2} I + \frac{1}{2}\sum \frac{t_k^2 \varepsilon_k cos2\phi_k}{\sigma_k^2} Q + \frac{1}{2}\sum \frac{t_k^2 \varepsilon_k sin2\phi_k}{\sigma_k^2} U,$$

$$\sum \frac{I_k t_k}{\sigma_k^2} = \frac{1}{2}\sum \frac{t_k^2}{\sigma_k^2} I + \frac{1}{2}\sum \frac{t_k^2 \varepsilon_k cos2\phi_k}{\sigma_k^2} Q + \frac{1}{2}\sum \frac{t_k^2 \varepsilon_k sin2\phi_k}{\sigma_k^2} U,$$

$$\sum \frac{I_k t_k \varepsilon_k sin2\phi_k}{\sigma_k^2} = \frac{1}{2}\sum \frac{t_k^2 \varepsilon_k sin2\phi_k}{\sigma_k^2} I + \frac{1}{2}\sum \frac{t_k^2 \varepsilon_k^2 sin2\phi_k cos2\phi_k}{\sigma_k^2} Q + \frac{1}{2}\sum \frac{t_k^2 \varepsilon_k^2 sin^2 2\phi_k}{\sigma_k^2} U, \tag{1.8}$$

where Σ denotes a sum over index k of the n polarizer observations. In other words, there are again a set of three equations and three unknowns. It is very similar in form to the set of three equations for the three-polarizer case solved above and, in fact, is identical if we define a set of "effective three-polarizer characteristics" using these weighted sums.

That is the three terms on the left hand side of equals signs (Equation (1.8) can be used as (I_1, I_2, I_3) in Equation (1.1) above. Label these new parameters as $I_k^{''}$, to get the new three-component vector of effective measurements:

$$I_1^{''} = \Sigma \frac{I_k t_k}{\sigma_k^2}, \qquad I_2^{''} = \Sigma \frac{I_k t_k \varepsilon_k cos2\phi_k}{\sigma_k^2}, \qquad I_3^{''} = \Sigma \frac{I_k t_k \varepsilon_k sin2\phi_k}{\sigma_k^2}, \tag{1.9}$$

with the error estimate for each measured intensity (=counts) denoted as $\sigma_k = \sqrt{I_k}$ and the 4 polarizers are assumed as perfect polarizers ($\varepsilon_1 = \varepsilon_2 = \varepsilon_3 = \varepsilon_4 = 1$). Therefore the corresponding factors reduce to unity. In that case, $I_k^{''}$ the values are expected to be constant. $I_1^{''}$ will be equal to sum over 4 polarizers throughput (Σt_k), $I_2^{''} = \Sigma t_k cos2\phi_k$ and $I_3^{''} = \Sigma t_k sin2\phi_k$, where Σ denotes a sum over index k of the 4 polarizers. The throughput values (t_k) can be used as the relative sensitivity of each polarizer as described above and the position angle of the polarizers (ϕ_k) can be calculated from AROLIS-Polarimeter Test measurements which will be mentioned in the next part. Similarly, a three-component vector of effective transmittances can be define as:

$$t_1^{''} = \sum \frac{t_k^2}{\sigma_k^2}, \qquad t_2^{''} = \sum \frac{t_k^2 \varepsilon_k cos2\phi_k}{\sigma_k^2}, \qquad t_3^{''} = \sum \frac{t_k^2 \varepsilon_k sin2\phi_k}{\sigma_k^2}, \tag{1.10}$$

and a vector of effective efficiencies is defined as:

$$\varepsilon_1^{''} = \frac{1}{\sum t_k^2/\sigma_k^2}\sqrt{\left[\sum \frac{t_k^2}{\sigma_k^2}\varepsilon_k cos2\phi_k\right]^2 + \left[\sum \frac{t_k^2}{\sigma_k^2}\varepsilon_k sin2\phi_k\right]^2}$$

$$\varepsilon_2^{''} = \frac{1}{\sum t_k^2\varepsilon_k cos2\phi_k/\sigma_k^2}\sqrt{\left[\sum \frac{t_k^2}{\sigma_k^2}\varepsilon_k^2 cos^2 2\phi_k\right]^2 + \left[\sum \frac{t_k^2}{\sigma_k^2}\varepsilon_k^2 sin2\phi_k cos2\phi_k\right]^2}$$

$$\varepsilon_2^{''} = \frac{1}{\sum t_k^2\varepsilon_k sin2\phi_k/\sigma_k^2}\sqrt{\left[\sum \frac{t_k^2}{\sigma_k^2}\varepsilon_k^2 sin2\phi_k cos2\phi_k\right]^2 + \left[\sum \frac{t_k^2}{\sigma_k^2}\varepsilon_k^2 sin^2 2\phi_k\right]^2} \quad (1.11)$$

Finally a vector of effective ”position angles” can be defined as:

$$\phi_1^{''} = \frac{1}{2}arctan\left[\sum \frac{t_k^2}{\sigma_k^2}\varepsilon_k sin2\phi_k / \sum \frac{t_k^2}{\sigma_k^2}\varepsilon_k cos2\phi_k\right]$$

$$\phi_2^{''} = \frac{1}{2}arctan\left[\sum \frac{t_k^2}{\sigma_k^2}\varepsilon_k^2 sin2\phi_k cos2\phi_k / \sum \frac{t_k^2}{\sigma_k^2}\varepsilon_k^2 cos^2 2\phi_k\right]$$

$$\phi_3^{''} = \tfrac{1}{2}arctan\left[\sum \tfrac{t_k^2}{\sigma_k^2}\varepsilon_k^2 sin^2 2\phi_k / \sum \tfrac{t_k^2}{\sigma_k^2}\varepsilon_k^2 sin2\phi_k cos2\phi_k\right] \quad (1.12)$$

By making these substitutions, the solution given by Equations (1.3) and (1.4) can be used immediately. Thereby the Stokes parameters (I, Q, U) can be obtained as follows:

$$I = \left[\left(\varepsilon_2^{''}\varepsilon_3^{''} sin(2\phi_3 - 2\phi_2)\right) I_1^* + \left(\varepsilon_1^{''}\varepsilon_3^{''} sin(2\phi_1 - 2\phi_3)\right) I_2^* + \left(\varepsilon_1^{''}\varepsilon_2^{''} sin(2\phi_2 - 2\phi_1)\right) I_3^*\right] / \Omega^*$$

$$Q = \left[\left(\varepsilon_2'' sin2\phi_2 - \varepsilon_3'' sin2\phi_3 \right) I_1^* + \left(\varepsilon_3'' sin2\phi_3 - \varepsilon_1'' sin2\phi_1 \right) I_2^* + \left(\varepsilon_1'' sin2\phi_1 - \varepsilon_2'' sin2\phi_2 \right) I_3^* \right] / \Omega^*$$

$$U = \left[\left(\varepsilon_3'' cos2\phi_3 - \varepsilon_2'' cos2\phi_2 \right) I_1^* + \left(\varepsilon_1'' cos2\phi_1 - \varepsilon_3'' cos2\phi_3 \right) I_2^* + \left(\varepsilon_2'' cos2\phi_2 - \varepsilon_1'' cos2\phi_1 \right) I_3^* \right] / \Omega^* \tag{1.13}$$

where,

$$\Omega^* = \varepsilon_1'' \varepsilon_2'' sin(2\phi_2 - 2\phi_1) + \varepsilon_2'' \varepsilon_3'' sin(2\phi_3 - 2\phi_2) + \varepsilon_1'' \varepsilon_3'' sin(2\phi_1 - 2\phi_3)$$

and,

$$I_1^* = 2\frac{I_1''}{t_1''}, \qquad I_2^* = 2\frac{I_2''}{t_2''}, \qquad I_3^* = 2\frac{I_3''}{t_3''},$$

That is a set of observations with n polarizers can be made equivalent to a set of observations through three polarizers.

In the actual case of n=3, it can also be shown that the maximum likelihood or least-squares solution is identical to the direct matrix inversion used for the three-polarizer case.